POSITRON ANNIHILATION INVESTIGATION OF VACANCIES IN AS-GROWN AND ELECTRON IRRADIATED DIAMONDS

BY

ANLE PU

A thesis
Submitted to the Faculty of Graduate Studies
In Partial Fulfillment of the Requirements
For the Degree of

MASTER OF SCIENCE

Department of Physics
University of Manitoba
Winnipeg, Manitoba

National Library of Canada
Acquisitions and Bibliographic Services
395 Wellington Street
Ottawa ON K1A 0N4
Canada

Bibliothèque nationale du Canada
Acquisitions et services bibliographiques
395, rue Wellington
Ottawa ON K1A 0N4
Canada

Your file Votre reference

Our file Notre référence

0-612-53210-0

Canada

THE UNIVERSITY OF MANITOBA

FACULTY OF GRADUATE STUDIES

*****

COPYRIGHT PERMISSION PAGE

Positron Annihilation Investigation of Vacancies in

As-Grown and Electron Irradiated Diamonds

BY

Anle Pu

A Thesis/Practicum submitted to the Faculty of Graduate Studies of The University

of Manitoba in partial fulfillment of the requirements of the degree

of

Master of Science

ABSTRACT

Vacancy-type defects in the four main types of diamond (Ia, Ib, IIa and IIb) were investigated using positron lifetime, Doppler broadening and optical absorption spectroscopies. In unirradiated samples vacancy clusters were found in all types, synthetic as well as natural. These clusters are situated in highly defected regions, rather than homogeneously distributed, and their concentration varies significantly from sample to sample. For synthetic Ib diamonds vacancy clusters were investigated as a function of nitrogen content. The bulk positron lifetime for diamond is calculated to be 98 ± 2 ps and the bulk Doppler S parameter is estimated to be 25% lower than that for silicon. Electron irradiation (2.3 MeV) produced neutral monovacancies in IIa diamond and the positron data correlated well, as a function of dose, with the GR1 optical zero-phonon line (the optical absorption at 740nm arise from neutral monovacancies in diamond); the introduction rate was estimated to be $0.5 \pm 0.2\ cm^{-1}$. In Ib diamond monovacancies were found to be negatively charged whereas they were neutral in IIa diamonds. The positron lifetime for monovacancies was $(40 \pm 6)\%$ larger than the bulk lifetime and the Doppler S parameter increased by $(8 \pm 1)\%$. At-temperature Doppler measurements between 30 and 770 K indicated that irradiation-produced neutral monovacancies can convert to the negatively charged state above 400 K but this was dependent on diamond type. Isochronal annealing of irradiated Ib diamonds showed that the complex of a substitutional nitrogen and a vacancy, formed upon annealing close to $600\,^{\circ}C$, undergoes two detectable modifications between 600 and $870\,^{\circ}C$ reaching a configuration stable to $1170\,^{\circ}C$. Key conclusions based on positron and optical data are in mutual accord.

We have developed a simplified model for the trapping of positrons by *negatively* charged vacancies. By solving the differential equations pertaining to the population of positron states, expressions for the experimentally observable positron parameters (lifetimes, their intensities and the Doppler broadening parameter S) were obtained. We show that the temperature dependencies of the positron parameters are markedly influenced by the ratio between the trapping rate from the delocalized state to the vacancy and that from the Rydberg-like state to the vacancy, and illustrate the usefulness of the model in the case of Doppler broadening data for diamond.

Based on results obtained from photon-modulated positron annihilation experiments (lifetime and Doppler broadening) it is found that the 0/- electronic level for isolated monovacancies in diamond is situated at 2.85 ± 0.15 eV above the valence band edge, i.e. essentially in the middle of the band gap. The dependency on photon flux of the conversion of neutral vacancies to negative vacancies can be explained by a model, which takes into account charging and decharging, by photons as well as that occurring due to the positrons.

ACKNOWLEDGEMENTS

The work presented in this report was carried out in partial fulfilment of the requirements for obtaining the MASTER IN SCIENCE degree from the University of Manitoba, Canada. This work was carried out at the Positron Laboratory of the Physics Department of the University of Winnipeg, Canada under the supervision of professor Steen Dannefaer.

I would like to express my most sincere gratitude and thanks to Prof. S. Dannefaer for his valuable advice, patient guidance and constant encouragement throughout this research project and carefully reading my thesis. Prof. S.Dannefaer leaves upon me a strong impression of a very kind and understanding person and a dedicated professor and researcher. I have greatly benefited in many ways by working with him.

I also wish to extend my thanks to Dr. D. Kerr, Mr. V. Avalos for their spending time and assistance for my project. Thanks are also due to the Winnipeg-based National Research Council of Canada laboratory for facilitating optical measurements as well as to the Chemistry Department at the University of Winnipeg.

I am especially most grateful to my parents: Mr. Chengming Pu and Mrs. Peiying Ge, my wife: Mrs. Yulan Yang, my son: Sirui Pu, and my daughter: Sarah Siyu Pu, for all their understanding, encouragement and continuous support over the years. To Yulan Yang, I cannot thank you enough for your love and much needed support at crucial times.

TABLE OF CONTENTS

Page

ABSTRACT.....i

ACKNOWLEDGEMENTS.....iii

LIST OF FIGURES.....vii

LIST OF TABLES.....xii

Chapter 1 INTRODUCTION.....1

1.1 Introduction.....2

1.2 Positron Annihilation.....4

Chapter 2 INTRODUCTION TO EXPERIMENTAL TECHNIQUES.....7

2.1 Introduction to experimental techniques.....8

2.2 Positron source and source correction.....9

2.3 Doppler broadening.....11

2.3.1 Spectrum analysis.....13

2.4 Positron lifetime spectroscopy.....16

2.4.1 Scintillator and photomultiplier.....19

2.4.2 The constant fraction discriminator.....20

2.4.3 Time to amplitude converter and multichannel analyzer.....22

2.4.4 Resolution function.....23

2.4.5 Calibration.....25

2.5 Fourier transform infrared spectroscopy.....25

2.6 Absorption measurements in the UV/VIS range.....26

Chapter 3 ANALYSIS OF THE MEASURED SPECTRA.....27

3.1 Introduction.....28

3.2 Positron implantation and thermalization.....28

3.3 Annihilation characteristics.....29

3.4 Positron Trapping.....30

3.5 Trapping model.....31

3.6 Important remarks.....37

3.7 Positronfit.....38

Chapter 4 BASIC CONCEPTS OF DEFECTS AND DIAMONDS.....43

4.1 Defects in materials.....44

4.2 Point defects.....45

4.3 Geometrical configuration of point defects.....46

4.3.1 The vacancy.....46

4.3.2 The divacancy.....47

4.3.3 The interstitial.....48

4.3.4 Complex defects.....50

4.3.5 Aggregates.....51

4.4 Diamond.....51

4.4.1 Structure of diamond.....51

4.4.2 The 'type' terminology for diamond.....53

Chapter 5 EXPERIMENTAL RESULTS AND DISCUSSIONS.....57

5.1 Positron annihilation investigation of vacancies in as-grown and electron irradiated diamonds.....58

5.1.1 Introduction.....58

5.1.2 Experimental.....61

5.1.3 Results.....63

5.1.4 Discussion.....79

5.1.5 Conclusion.....91

5.2 On the trapping of positrons by negatively charged vacancies.....93

5.2.1 Introduction.....93

5.2.2 Model.....93

5.2.3 Results and discussion.....97

5.2.4 Conclusion.....106

5.3 Determination of the 0/- electronic level of the monovacancy in diamond by means of positron annihilation.....108

5.3.1 Introduction.....108

5.3.2 Experimental.....109

5.3.3 Results and discussion.....110

5.3.4 Conclusion.....119

REFERENCES.....**120**

LIST OF FIGURES

FIGURE		PAGE
2.1	Schematic representation of three methods of positron annihilation measurements, Doppler broadening, lifetime, and angular correlation.....	8
2.2	Decay scheme for ^{22}Na	9
2.3	The vector diagram of the momentum conservation in the 2γ-annihilation process. P is the total momentum, subscripts L and T refer to longitudinal and transverse components,respectively.....	11
2.4	Typical Doppler-broading schematic setup.....	13
2.5	Doppler broadened spectrum. The S parameter is defined as the ratio between the counts in the S region (511 ± 0.7 keV) and that in whole spectrum (511 ± 5.0 keV). The W parameter is defined similarly but using the two regions marked by the W's (506.0-507.7 keV and 514.3-516.0 keV). Background has been subtracted from the spectrum.....	14
2.6	Schematic diagram of a typical equipment for measuring positron lifetimes..	18
2.7	Gamma energy spectrum. In the start window counts originate from 1.28 MeV (start) γ-rays while in the stop window they originate from the (stop) 511 KeV annihilation γ-rays.....	19
2.8	Uncertainty in time determination due to different pulse heights by: a) leading edge and b) constant fraction.....	21
2.9	Experimentally obtained lifetime spectrum (8×10^{16} counts) for a Ib diamond sample set	23

2.10 Shape of a typical prompt curve for ^{60}Co..... 24

4.1 Schematic representation of simple point defects: a) Vacancy; b) Self interstitial; c) Interstitial impurity; d) Divacancy; e) Subtitutional impurity; f) Vacancy substitutional impurity complex..... 45

4.2 Schottky and Frenkel defects in an ionic crystal. The arrows indicate the displacement of the ions..... 46

4.3 The monovacancy in diamond lattice. a) Four bonds are broken; b) V^0; c) V^- 47

4.4 The divacancy configuration and its schematic two dimension-representation..... 48

4.5 The split-divacancy configuration and its schematic representation..... 48

4.6 Different interstitial configurations in Diamond lattice. a) The hexagonal; b) The tetrahedral; c) The bond-centered; d) some split interstitial configurations..... 49

4.7 Vacancy-oxygen complex, the oxygen atom is slightly displaced off the substitutional position..... 50

4.8 One of the possible configurations for a penta-vacancy..... 51

4.9 a) Tetrahedral bonds of the carbon atoms; b) Structure of diamond. Two of the three cleavage directions are shown..... 52

4.10 Crystal structure of diamond, showing the tetrahedral bond arrangement..... 53

5.1 Lifetime parameters at room temperature for the Ib(syn) samples as a function of nitrogen content..... 66

5.2 S and W parameters at room temperature for the Ib(syn) samples investigated by lifetime spectroscopy (Fig.5.1)..... 67

5.3 Lifetime results for the IIa(1) samples at room temperature as a function of the dose from 2.3 MeV electrons..... 69

5.4 Relative changes in S at room temperature for the IIa(1) samples for which lifetime data are shown in Fig.5.3. S_{Ref}=0.3800..... 70

5.5 Relative changes in S for irradiated diamonds as a function of sample temperature. ■: Ib(syn, Ns = 130 ppm), dose $14\times10^{17}e^{-}/cm^{2}$. ▲: Ib(nat), dose $3\times10^{17}e^{-}/cm^{2}$. •: IIa(1), dose $14\times10^{17}e^{-}/cm^{2}$. ▼: Ia(1), dose $25\times10^{17}e^{-}/cm^{2}$. For sample identifications see Table 1..... 75

5.6 Relative S parameter as a function of annealing temperature for Ib (syn, N_S = 130 ppm) irradiated to a dose of $14\times10^{17}e^{-}/cm^{2}$. The entry at $20^{0}C$ is for the as-irradiated case and the one at $480^{0}C$ corresponds to the highest temperature in the at-temperature measurements shown in Fig. 5.5..... 76

5.7 Lifetime data for the samples whose relative S parameters are shown in Fig.5.6. No τ_1 component could be resolved. In addition to τ_2 there was a τ_3 component ($\cong$ 300 ps) with an intensity of $(100-I_2)$..... 77

5.8 Optical absorption coefficient of Ib (syn, N_S = 130 ppm) irradiated to a dose of $14\times10^{17}e^{-}/cm^{2}$ and then annealed to $720^{0}C$: (a) for the visible range and (b) for the infrared range, the latter showing the presence of N_S... 78

5.9 Integrated absorption of the N_SV^{-} zero-phonon line (see Fig.5.8(a)) as a function of annealing temperature..... 79

5.10 (a) Model for the trapping of positrons originally in the (delocalized) bulk state, into either several Rydberg-like states, thermal detrapping there from and transfer to the vacancy, or by direct trapping into the vacancy. (b) Simplified model replacing the manifold of Rydberg-like states with a single state resulting in the occupation probability equations (5.3~5.5), see text..... 94

5.11 S/S_B as a function of temperature for different ratios of κ_{BD}/η_{RD} using the following parameter values at 300 K: Bulk lifetime 220 ps, defect lifetime 270 ps, defect specific S parameter S_D/S_B = 1.07, $\mu_{BR}=5\times10^6(\frac{300}{T})^{1/2} ns^{-1}$, $\mu_{BD}=1\times10^6(\frac{300}{T})^{1/2} ns^{-1}$, η_{RD}= 20 ns^{-1} (4 times the bulk annihilation rate), and E_B= 50 meV. For the lowest ratio of κ_{BD}/η_{RD}, the relative concentration of the negatively charged vacancies is 2 ppm, and for increasing ratios, they are, 4, 8, 20, 40, 400 ppm..... 98

5.12 Individual lifetimes τ_1(panel (a)) and τ_2(panel (b)) for different ratios of κ_{BD}/η_{RD} (T = 300 K); τ_3= 270 ps is not affected by these ratios. In panel (c) is shown the composite τ_{avg} parameter. Parameter values correspond to those used in Fig.5.11..... 100

5.13 Intensities I_1, I_2 and I_3 of the τ_1, τ_2 and τ_3 (=270 ps) lifetime components for different ratios of κ_{BD}/η_{RD} (T = 300 K)..... 101

5.14 Experimental Doppler data as a function of sample temperature for two sets of diamonds, Ib (down-triangles) and illuminated IIa (up-triangles). The solid curves are fits to the data using parameter values as listed in Table 9

(first and third row) while the dashed curve is an attempt to fit the data for Ib using trapping parameters from IIa (second row in Table 9)..... 103

5.15 Doppler data obtained at 25 K with the samples in the dark and when illuminated with a photon flux of $9\times10^{15}cm^{-2}s^{-1}$ for photon energies between 2.35 and 3.3 eV..... 110

5.16 Fraction of positrons trapped as calculated from the data in Fig.5.15 using Eq.(5.3.1)..... 112

5.17 Doppler data as a function of temperature for samples in the dark and when illuminated at a photon energy of 2.83 ± 0.07 eV at a flux of $9\times10^{15}cm^{-2}s^{-1}$. The curve shows a fit using the model described in the text. 113

5.18 Fraction of neutral vacancies converted negative as a function of photon energy. The sample temperature was 25 K..... 115

5.19 Doppler data as a function photon flux for two sample temperatures. The photon energy was 2.83 ± 0.07 eV..... 117

5.20 Fraction of neutral vacancies converted negative as calculated from the data in Fig.5.19 sample temperatures..... 117

LIST OF TABLES

TABLE **PAGE**

1. Concentrations of substitutional nitrogen (N_S), N_S-N_S (A centers) and $4N_S \cdot V$ (B centers). In the Ia(2) diamonds there were also $3N_S \cdot V$ (N3) centers and platelets but their nitrogen concentration cannot be determined. The purely Ib type is synthetic, while the rest are natural diamonds. Entries of zero mean below detection limit (≈ 1 ppm). 1 ppm corresponds to an absolute concentration of $1.76\times10^{17}/cm^3$ 61
2. Lifetime results for unirradiated diamonds measured at room temperature. Lifetimes and their associated intensities are listed together with the auxillary parameters τ_{avg} and τ_B^{TM} as defined by Eqs. (5.1) and (5.2)..... 65
3. S and W parameters for unirradiated diamonds at room temperature. For easy reference, S and W parameters for undoped float-zone Si are 0.5095 and 0.0082, respectively, using the same energy regions as for diamond (see Fig.2.5)..... 65
4. Lifetime and Doppler data for Ib(syn, Ns = 130 ppm) for accumulated electron doses. Results are for measurements at room temperature. S_{Ref} = 0.3800..... 71
5. Lifetime data for Ib(nat) at room temperature for accumulated electron doses. 72
6. Results obtained for Ia(1). First row, before irradiation; second row, after irradiation with 3.5 MeV electrons to a dose of $21\times10^{17}e^-/cm^2$ at $1\times10^{17}e^-/cm^2/h$; third row, after annealing to 1020^0C; fourth row, for re-

irradiation to nearly the same dose as before but with a 7 times higher dose rate..... 73

7. Lifetime and Doppler data as a function of temperature for Ib(syn, Ns=130 ppm) irradiated to a dose of $14\times10^{17} e^{-}/cm^{2}$. S_{Ref}=0.380..... 74

8. Dose dependencies for IIa(1) for the neutral vacancy lifetime, τ_{V^0}, trapping rate, κ, the defect specific Doppler parameter S_{V^0}/S_{Ref}, and the peak absorption coefficient of the GR1 zero phonon line at 741 nm (1.673 eV)..... 84

9. Parameter values used to obtain the fits to the experimental data in Fig.5.14. The bulk annihilation rate is 10.2 ns^{-1}, the defect specific S/S_{Ref} is 1.079 for both neutral and negative monovacancies, and the vacancy concentration is 4 ppm ($7\times10^{17}/cm^{3}$) [see section 5.1]. μ_{BR} and μ_{BD} are specific trapping rates at 300 K. For neutral monovacancies the specific trapping rate is $1.5\times10^{6} ns^{-1}$ and is used only in the case of IIa diamond..... 104

10. Lifetime results for different illumination conditions. The photon flux was the same as for the Doppler data shown in Fig.5.15 ($9\times10^{15} cm^{-2}s^{-1}$) and the sample temperature was 30 K..... 111

CHAPTER ONE

INTRODUCTION

1.1 Introduction:

Diamond is famous for its beauty as a gem. It is composed of one of the commonest substances on earth, ordinary carbon, and is the hardest material man has ever discovered and the purest that occurs in Nature. The unique hardness today plays a formidable part in modern industrial technology. From a physical point of view diamond has the strongest bonds and highest atomic density leading to unique physical properties.

Diamonds have attracted man's attention for thousands of years. As early as about 800 B.C. diamonds were known in India. In fact, cut diamonds were produced only in India until the beginning of the eighteenth century. All diamonds were found in the alluvial gravels or conglomerates of active or dried-up rivers until about a century ago when they were discovered in great rock pipes that penetrated deeply into the earth. This rock is called Kimberlite as named after its discoverer. Diamonds are closely associated with the kimberlite rock, but are actually not attached to it. Today it is believed that kimberlite is a source rock for diamonds. It brings diamonds from the earth's upper mantle (at least 150 km thick) to its surface. The relationship of diamond to these volcanic rocks (kimberlites) and, in particular, to the samples of upper mantle rocks and minerals that kimberlite contains, are now major and continuing research projects aimed at understanding the geological processes operating in the earth's upper mantle. For detailed information about diamond genesis and growth and occurrences in environments, refer to [1,2].

It is still not certain how diamonds originated [3]; however, one of the current theories is that diamonds were formed in the earth's mantle at depths of not less than 15

kilometers. The material of the mantle is called peridotite and eclogite. Diamond genesis and growth occurs principally in the molten peridotite and eclogite at a wide range of pressures and temperatures between about 3×10^8 kilogram-forces per square meter at 700^0C, and 9×10^8 kilogram-forces per square meter at 2,500 ^{0}C. These conditions must have been remained stable for long enough to allow for the crystallization of diamonds and for the migration of nitrogen atoms in the crystals, because the majority of all natural diamonds contain nitrogen in various forms. Meanwhile a pressure of carbon dioxide in the Earth's mantle gradually built up, eventually driving the diamond and molten magma (peridotite) to the surface. In this process the molten peridotite became altered by chemical change and also picked up many other rocks and minerals, to become kimberlite. After reaching the earth's surface, erosion releases diamonds into adjacent river systems, which is the reason why diamond depositions are found within these rivers or along shorelines where rivers meet the sea.

Since the turn of the 19th century it was known that diamond could be converted into graphite and many attempts have been made to synthesize diamond from various forms of carbon with other structures. A Swedish company under the direction of B.von Platen achieved the first success in 1953. It is now known that diamond may be synthesized both at high pressure in the diamond stable region of the carbon phase diagram or at low pressure in the graphite stable field of the phase diagram, using a host of chemical and physical vapour deposition techniques [3,4]. The trick is here to remove graphite by etching it away by means of hydrogen so leaving behind only the diamonds.

A great number of studies of diamond have been carried out because of its excellent optical and electrical properties, such as high thermal conductivity, wide

range of optical transparency, high tensile strength and absence of plastic flow at high temperatures, etc. The feasibility of using these properties for electronic device applications is in many cases limited by defects and impurities, which in the last decade or two has sparked renewed interest in the fundamentals of defects in diamond. The main problem for using diamonds as electronic devices is that *n*-type diamonds to date have not been made, only *p*-type, and that curtails the possibility for making *p-n* junctions. The positron annihilation technique is regarded as a powerful means of studying defects in metals and semiconductors. The work presented in this thesis will concentrate on using positron lifetime, Doppler broadening and optical absorption spectroscopies.

1.2 Positron Annihilation:

Positrons are the anti-particles of the ubiquitous electrons in this world. Their existence was first predicted by Dirac in 1926 when he tried to explain the negative energy solutions of the Klein-Gordon relativistic quantum mechanical equations [5,6]. Six years later Anderson verified experimentally Dirac's postulation using the Wilson cloud chamber [7]. In the presence of strong magnetic fields, the tracks of positively charged particles with a mass equal to the electron mass was found. Soon after Blackett and Occhialini [8] confirmed the observations of Anderson. Positron and electron has the same rest mass ($9.01095\times10^{-31} kg$) and spin ($\frac{1}{2}$), but opposite charge (1.6×10^{-19} coulomb) and magnetic moment.

In 1934 Thibaud [9] showed that when a positron annihilates with an electron γ–rays are emitted (one, two, three). In condensed matter, almost all positrons annihilate with electrons by emission of two gamma-quanta, each with a nominal energy of 0.511

MeV corresponding to the rest-mass energy of a positron. Obviously this is a relativistic process where the masses are converted into energy. Later, Klemperer [10] demonstrated that the two gamma-rays emerging from the annihilation site are in coincidence and in essentially opposite directions. The γ-rays are modified, however, by the momentum and energy distributions of the electrons in the materials, in the sense that small deviations from 0.511 MeV occur due to Doppler shift as well as small deviations from colinearity.

In 1951, Deutsch demonstrated the existence of positronium, the bound state between a positron and an electron [11,12]. During the 1950's scientists studied the structure and properties of positrons and positronium atoms. In the early 1960's they started to *apply* positrons for the study of condensed matter and discovered positron trapping at vacancies. The experimental and theoretical basis of the positron spectroscopy of defects in metals was developed in the 1970's, parallel with chemical applications. From the 1980's interest in semiconductor applications started gradually to arise, and especially the development of low-energy positron beams opened the avenue for defect studies in surface layers and interfaces which have growing importance in semiconductor applications.

The positron technique has many advantages in the study of materials. It provides a nondestructive method and there is no need for special sample preparation. It may apply to in-situ studies, e.g., on dynamic phenomena at elevated temperatures [25]. Positron annihilation allows us to study vacancy-type defects in crystal, provided the positrons are trapped by the vacancies, a craveat of particular importance in semiconductors. Variations of the vacancy concentrations are accessible in a "concentration window" that extends roughly between 10^{-7} and 10^{-4} in atomic units. Apart from muon spin

relaxation under very special conditions [14] no other technique has a similar sensitivity to low vacancy concentrations. Today positron annihilation has become an indispensible tool for defect studies.

CHAPTER TWO

INTRODUCTION TO EXPERIMENTAL TECHNIQUES

2.1 Introduction to experimental techniques:

The positron annihilation method is successfully used to study vacancy-like defects such as vacancies, vacancy clusters, voids, and possibly dislocations. Relatively small defect concentrations of only a few parts per million can cause a significant fraction of positrons to annihilate from defect states, and therefore cause measurable changes in the annihilation characteristics as shown in Fig 2.1.

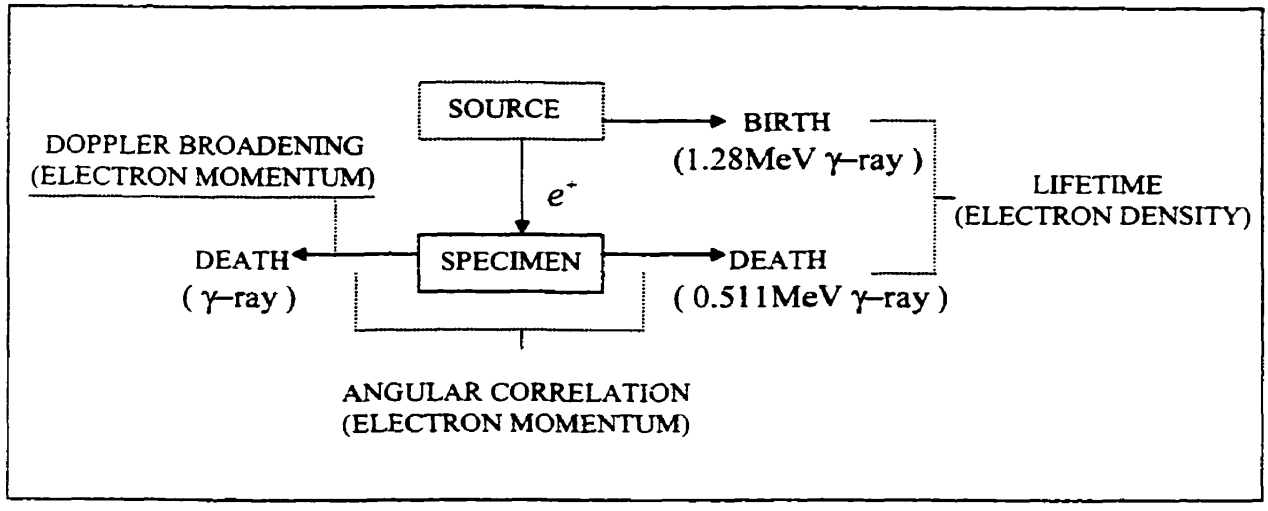

Figure 2.1. Schematic representation of three methods of positron annihilation measurement, Doppler broadening, lifetime, and angular correlation.

Annihilation measurements are based mainly on the following three methods of positron spectroscopy: the positron lifetime, angular correlation of annihilation radiation and Doppler broadening profiles. The work presented in this thesis deals only with the use of positron lifetime and Doppler broadening. Positron lifetime gives information about the electron density by measuring the time elapsed from the emission of the birth γ–ray to the death γ–ray. Doppler broadening gives information about electron momenta by measuring the energy shift relative to the nominal value of 0.511 MeV. The angular

correlation technique determines the deviation from the nominal colinearity between the two death γ–rays, but is essentially only a high-resolution form of Doppler broadening measurements.

Fourier transform infrared spectroscopy and optical absorption measurements in the ultraviolet-visible-near-infrared range are used for the characterization of the diamonds. This chapter gives a general overview of these methods and some of the background knowledge.

2.2. Positron Source and Source Correction:

The positron source used in all of our experiments is the ^{22}Na isotope (in the form of ^{22}NaCl). It has a half-life of 2.6 years. Its decay scheme is shown in Figure 2.2.

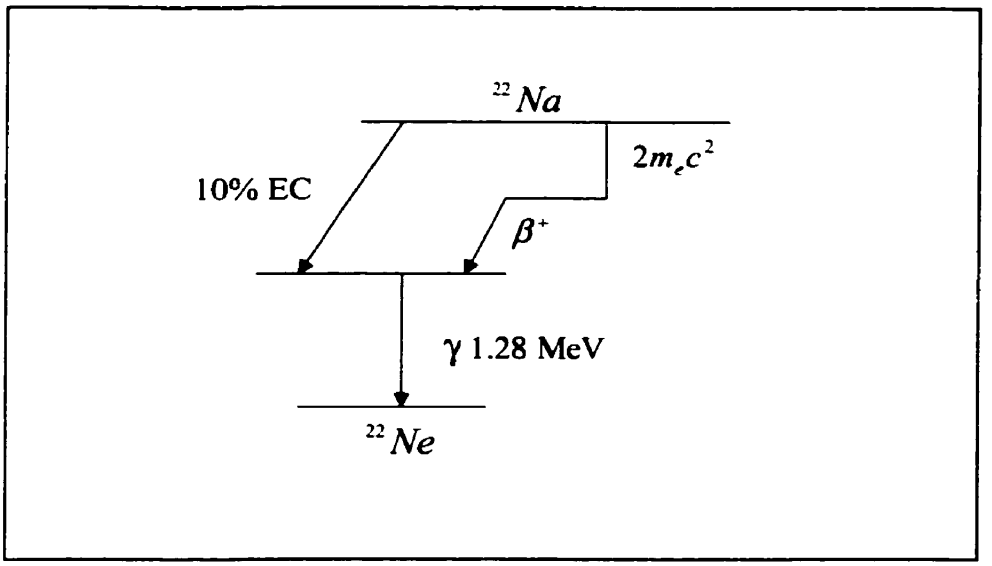

Figure 2.2. Decay scheme for ^{22}Na.

A small fraction ($\cong 2\%$) of positrons will annihilate in the foil encapsulating the ^{22}NaCl source material (to prevent contamination of the samples) and also in the source material itself, contributing additional lifetimes to the measured spectrum. These

additional lifetimes are very difficult to determine so to minimize these contributions, the choice of the encapsulating material as well as the technique of depositing the source material is very important. The positron source preparation is done by evaporating a few micro curies of aqueous solution ^{22}NaCl deposited on a very thin aluminum foil (around 0.8 μm thick) wrapped as a square envelope of approximately 5×5 mm^2 around the source. For the purpose of our experiments, the strength of the sources was between 10 to 19 μCi. To minimize source contributions we have developed a new technique in which the original aqueous ^{22}NaCl solution is first dried out completely in the supplied vial having a conically shaped bottom. Then, using a micro-pipet, 4-5 microliters of water is added to form a highly concentrated solution. Finally a micro syringe takes the solution depositing it on the source envelope material. Usually one drop produces a 5 μCi source. If two or more drops are needed to form a stronger source, it is necessary that each drop need to dry separately. The dried drops form an evenly distributed layer of ^{22}NaCl with a diameter of less than 1 mm. This source preparation technique removes the usual ringlike build-up of source material and also removes a long-lived positron lifetime from the spectrum which is known to affect numerical analyses. Minimizing the thickness of the Al foil is in order to minimize the fraction of positrons annihilation in the encapsulating envelope. With the improvements in source preparation technique the extraneous source contribution is only 2% and, importantly, the cumbersome long lived source contribution has been removed.

Since the contributions of the foil to the S parameter are within the uncertainty of the measurement, source correction is superfluous for Doppler broadening spectra. However, it is important to quantify the source contribution to the lifetime spectrum,

because the analysis of lifetime spectra involves numerical fitting of exponentials. In theory one can estimate the fraction of positrons annihilating in the foil by considering the exponential implantation profile of positrons emitted from a β^+ source and multiple backscatter from the sample back into the foil. In the experiment, one can determine it by measuring the lifetime spectrum of a stack of foils thick enough to stop all positrons. The aluminum foils used in our experiment result in a lifetime of 250 ps, with a relative intensity of 1.5 %. Such a low source contribution has light, if any, effect on the positron lifetime analyses as checked by analyzing a experimental spectra using different assumptions for the source contribution (0% ~ 5%).

2.3. Doppler Broadening:

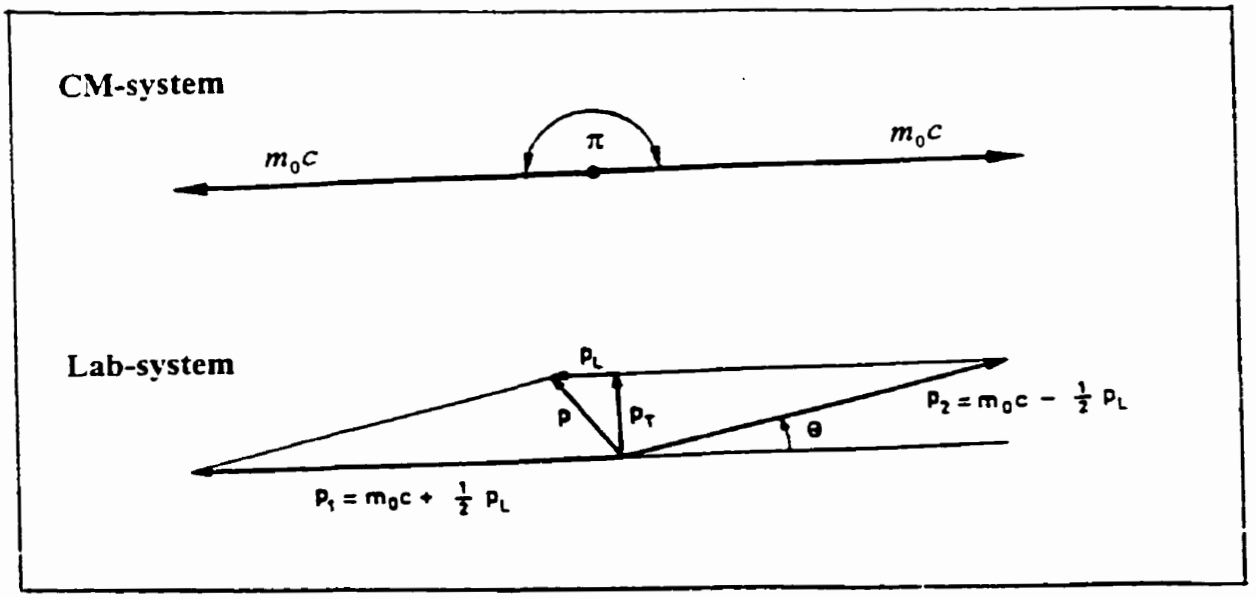

Figure 2.3. The vector diagram of the momentum conservation in the 2γ-annihilation process. P is the total momentum, subscripts L and T refer to longitudinal and transverse components,respectively.

The positron-electron annihilation emits 2 γ–quanta. In their center-of-mass frame the two photons are moving strictly into opposite directions, with the energy being exactly $m_0c^2 = 511$ KeV. Because of the non-zero momentum of the electron-positron pair (due largely to the momentum of the electron) the photons deviate from colinearity in the laboratory frame. As illustrated in Figure 2.3 the deviation of the gamma-rays from colinearity is

$$\theta \approx \frac{P_T}{m_o c} , \qquad (2.1)$$

where P_T is the momentum component of the annihilation pair normal to the photon emission direction.

The motion of the electron-positron pair also causes a Doppler shift in the energy of the emitted photons measured in the laboratory system. The frequency shift is

$$\frac{\Delta\nu}{\nu} = \frac{V_L}{c} , \qquad (2.2)$$

where V_L is the longitudinal velocity component of the pair in the direction of the annihilation gamma emission and c is the speed of light. Obviously we have

$$V_L = \frac{P_L}{2m_o} \qquad (2.3)$$

Since the energy of a photon is proportional to its frequency ν, we have

$$\frac{\Delta E}{E} = \frac{\Delta\nu}{\nu} = \frac{V_L}{c} \qquad (2.4)$$

Then we get the Doppler energy shift:

$$\Delta E = \frac{V_L}{c} E = \frac{V_L}{c} m_o c^2 = \frac{P_L}{2m_o} m_o c = \frac{P_L c}{2} . \qquad (2.5)$$

Since the momentum of the thermalized positrons is almost zero, P_L almost equals the momentum of electrons. Thus the line shape of the annihilation radiation reflects the momentum distribution of electrons in the sample.

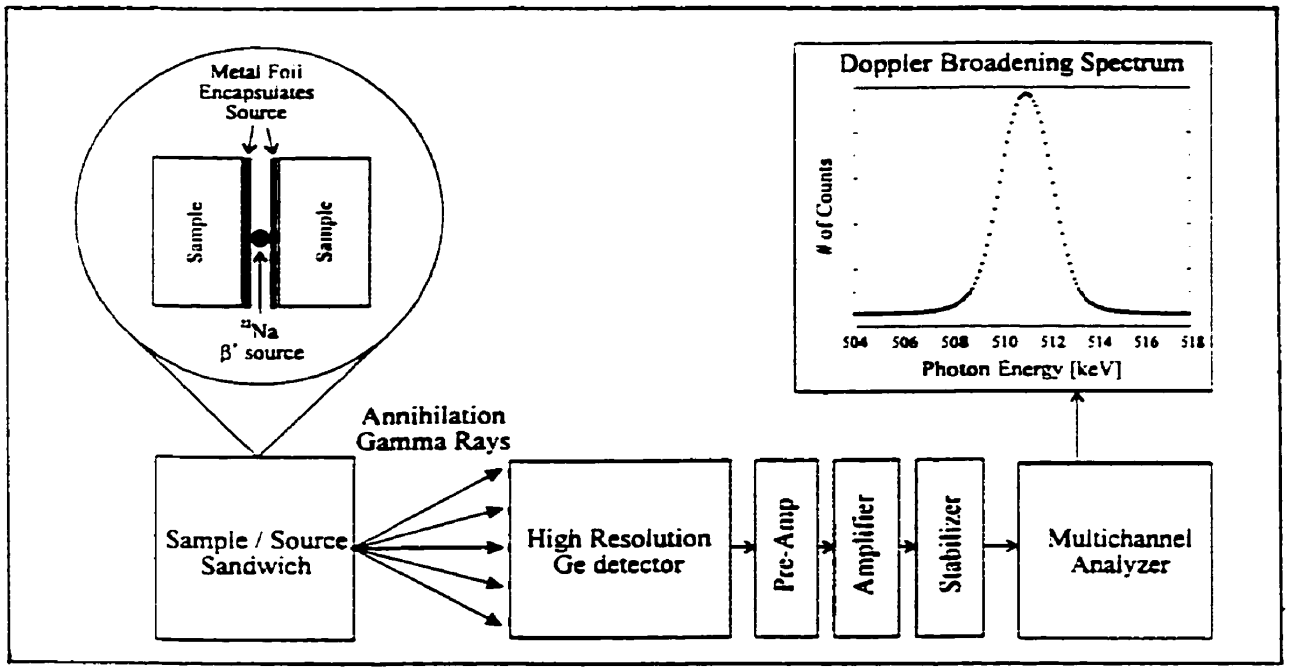

Figure 2.4. Typical Doppler-broading schematic setup.

Those small energy changes ΔE (in the order of a few KeV) can be measured by a high-purity Ge detector. Figure 2.4 shows a typical Doppler-broading schematic setup. The full width at half maximum (FWHM) of the resolution function of a Ge-detector at 511 KeV is typically 1.2 KeV, which is considerable compared to the typical electron momenta of the order of 10 KeV, so Doppler broadening experiments can not yield detailed information.

2.3.1. Spectrum analysis:

A Doppler broadened spectrum consists of two basic contributions, one arising from valence electrons and one from core electrons. The latter contribution is relatively weak since the positron wavefunction penetrates little into the core region, but these high-momentum core electrons give rise to a much wider distribution than the valence electrons. Analysis of the Doppler broadening data in the energy spectrum is normally quantified by the so-called " S parameter " as introduced by Mackenzie et al [15]. This parameter is defined by the ratio of the counts between the central area of the annihilation 511 keV peak, usually within the energy range 511 ± 0.7 keV (see figure 2.5), to the total area in the peak within the range 511 ± 5.0 keV. In the same way, the wing parameter, W, is defined as the ratio of counts in the two wing regions of the peak to the total counts in the peak (see figure 2.5).

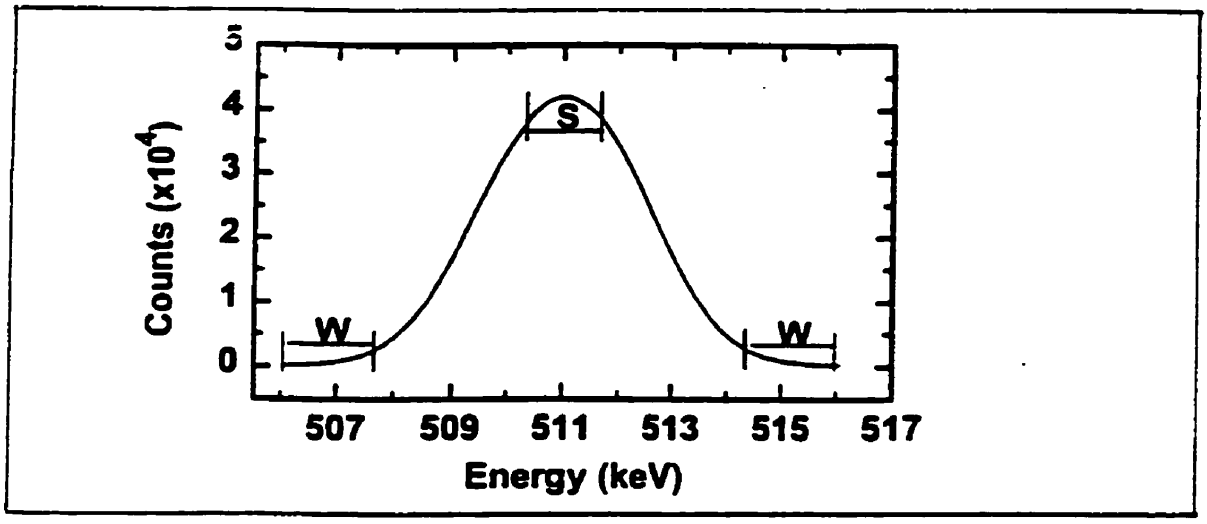

Figure 2.5. Corresponding Doppler broadened spectrum. The S parameter is defined as the ratio between the counts in the S region (511 ± 0.7 keV) and that in whole spectrum (511 ± 5.0 keV). The W parameter is defined similarly but using the two regions marked by the W's (506.0-507.7 keV and 514.3-516.0 keV). Background has been subtracted from the spectrum.

It can be seen that the very definition of S and W they concentrate on the valence (low momentum) and core electron momenta, respectively. Since the S, W parameter energy windows are arbitrary, these parameters are not directly comparable between different measuring systems. The " window " of energy for S is usually chosen so that S $\approx$ 0.5 [16] in order to minimize the uncertainty in the measurement. The ensuing small uncertainty in the S parameter makes it sensitive to minute changes. To facilitate comparisons between experimental results, it is usual to quote relative values, such as S_D/S_B and W_D/W_B, where S_B, W_B refers to the bulk and S_D, W_D to the defects. These relative values are surprisingly independent the chosen energy windows.

The line shape parameters S, W have values characteristic for each material depending on the electron-momentum distribution. When positrons annihilate in the bulk state, the amount of broadening depends on the average electron momentum in the bulk of the sample. When positrons are trapped, the lineshape is altered by the trapping defect. In a trapped state such as an open volume defect, the positron wavefunction is localised and has more overlap with the valence electrons of the atoms surrounding the defect than with the core electrons. Since valence electrons have lower momentum than core electrons, this leads to a narrower annihilation peak; Thus we may observe a larger S parameter than in a sample without defects. On the other hand, core electrons have momentum values that are mainly reflected by the W parameter. Therefore, the S and W parameters represent predominantly the contribution for annihilation with the valence and core electrons. The W and S parameters roughly show opposite behavior, i.e. an increase in W is accompanied by a decrease in S.

In the case of only one defect state the S and W parameters can be expressed as

$$S = (1-f)S_B + fS_D, \qquad (2.6)$$

and

$$W = (1-f)W_B + fW_D, \qquad (2.7)$$

where B denotes the bulk state and D the defect state and f is the fraction of positron annihilating in the defect. This fraction is given by the expression

$$f = \frac{\kappa}{\lambda_B + \kappa} . \qquad (2.8)$$

Here κ is the trapping rate (see section 3.5) and λ_B is the annihilation rate in the bulk state. Equations (2.6 and 2.7) can be rearranged to give

$$\frac{S_D}{S_B} = \{(\frac{S}{S_B}) + f - 1\}/f \qquad (2.9)$$

and

$$\frac{W_D}{W_B} = \{(\frac{W}{W_B}) + f - 1\}/f \qquad (2.10)$$

As stated above, it is pertinent to report only on relative values, so equations (2.9 and 2.10) are useful forms for calculating the defect specific values of S_D/S_B (W_D/W_B) provided f is known. It is important to note that Doppler data do not provide for the determination of "f", which requires the independent information from lifetime measurements.

2.4. Positron Lifetime Spectroscopy:

Positron lifetime spectroscopy is a more powerful analytical technique than Doppler broadening. Several experimental parameters can be extracted from a lifetime spectrum, and in many cases we can calculate directly all relevant physical parameters using the trapping model (see 3.5). Therefore, lifetime measurement can identify defects

and their concentrations, but this comes with a price, namely complexity of analysis, which is a definite drawback.

The lifetime of an individual positron is defined as the difference in time between the zero-time (start) of an lifetime measurement and the annihilation event (stop); it is to a very good approximation equal to the time that the positron spent in the sample. The entirety of the positron lifetimes registered during a run constitutes the lifetime spectrum. In the lifetime measurements the positron "death" signals (i.e. stop signal) are provided by the 511 KeV γ–quanta generated by the electron-positron annihilation, but the "birth" signals (i.e. start signal) may be obtained by two methods. The first method is the so-called $\beta^+\gamma$–technique, where the passage of the positron through a scintillation counter located between the positron source and the sample is registered. The second method is the so-called $\gamma\gamma$–technique. It uses a "prompt" γ–quanta (the 1.28 MeV photons from ^{22}Na in our case) emitted from the positron source simultaneously with the positron (refer to figure 2.2 for the decay scheme of ^{22}Na). The $\beta^+\gamma$–technique was introduced by Bell and Graham [17] and has the potential of giving higher counting rates than $\gamma\gamma$–technique, but has lower time resolution. The $\gamma\gamma$–technique was first used by Shearer and Deutsch [18,11] in their study of positrons in gases, and is the technique used today in most laboratories.

In our laboratory we use the so-called fast-fast time coincidence system which belongs to the $\gamma\gamma$–technique. A schematic diagram of the equipment is shown in figure 2.6 where the lifetime measuring system is divided into two branches, the start branch and the stop branch which is connected to the detector #1 and the detector #2, respectively.

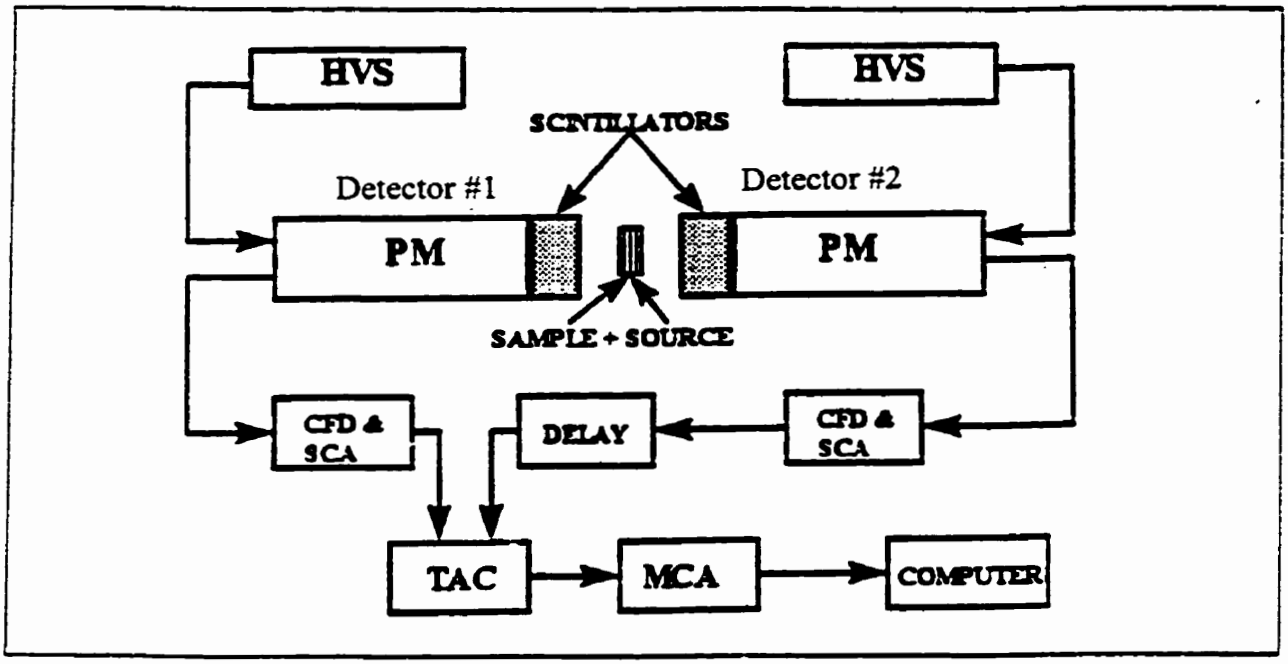

Figure 2.6. Schematic diagram of a typical equipment for measuring positron lifetimes.
HVS- High voltage supply. PM- Photomultipliers. CFD- Constant fraction discriminators. SCA- Single channel analyzer. TAC- Time to amplitude converter. MCA- Multichannel analyzer.

The detector #1, as the start detector, places the energy window (as shown in figure 2.7) to detect one photon of energy 1.28 MeV. The task of the detector #2 is to detect one photon of energy 0.511 MeV by placing the energy window as shown in figure 2.7. The signal from detector #1 is fed into a discriminator circuit (Constant Fraction Discriminator, CFD), which gives an output pulse provided the signal falls within a selected pulse height window corresponding to 1.28 MeV γ–rays. The output from the CFD is then fed into a time –to-amplitude converter (TAC). The detector #2 as the stop branch is quite similar to the start branch except that the output from the CFD only occurs if the signal from the detector falls within the 511 KeV γ–rays. To makes the TAC operate properly a time delay is usually necessary. The delayed signal is then fed into the

TAC for conversion. The output of the TAC is a pulse signal whose amplitude is proportional to the time difference between the two input signals and thus proportional to the time lapse between the start and stop signals from the detectors. These output pulse amplitudes are then stored according to height by the multichannel analyzer (MCA). In this way the channel number in the MCA is proportional to the time difference between the 1.28 MeV photon and 0.511 MeV photons, and the number of events recorded with a certain time difference is stored in the MCA.

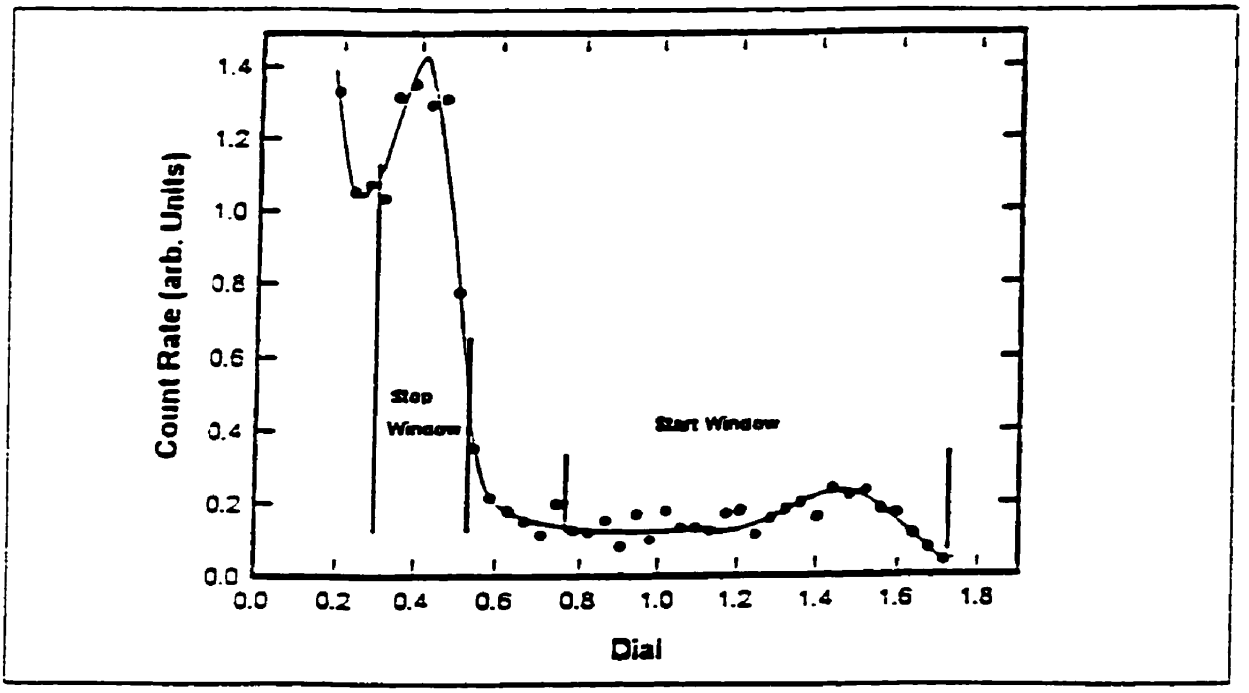

Figure 2.7. Gamma energy spectrum.

2.4.1. Scintillator and Photomultiplier:

The detector consists of a plastic scintillator coupled to a photomultiplier tube [20]. The scintillator is the device that converts the γ–quanta into an optical signal by generating luminecent decay of excited molecules. The photomultiplier tube is a

photosensitive device consisting of a photoemissive cathode followed by focusing electrodes, an electron multiplier and an electron collector.

The incident photons (γ–quanta) enter the scintillator and interact with the molecules of the scintillator. These molecules will be excited, and some of the excitation energy will be liberated as photons in the visible (or near visible) light. This light is guided into the photomultiplier (PMT) and a suitable optical coupling between the scintillator and the PMT is very important to reduce scattering effects. When the light strikes the photocathode of the photomultiplier tube, the photocathode emits photoelectrons, normally releasing several photoelectrons per photon. These photoelectrons are then directed by the focusing electrode voltages towards the electron multiplier where electrons are multiplied (by a factor of $10^5 \sim 10^6$). These electrons are finally collected at the anode constituting the (current) output signal of photomultiplier tube.

In our laboratory, we used Hamamatsu photonic tubes (PMT) and a Pilot-U plastic scintillators manufactured by Nuclear Enterprises (decay rate ~ 0.7 ns). The Pilot-U scintillators are shaped like a truncated cone and polished to mirror-like surfaces. Although this configuration causes a small decrease in the count rate compared to a cylindrically shaped scintillator, it cuts down on the scattering of photons from the walls of the scintillator, and that improves significantly on the time resolution.

2.4.2. The Constant Fraction Discriminator (CFD):

This electronic component is the most important one in the equipment. Essentially it determines the time of arrival of the pulse of charge that came from the photomultiplier

tube as caused by the γ-ray entering into the scintillator. However, time of arrival is ill-defined since the pulse heights from the PMT varies even though they originate from the same γ-ray energy.

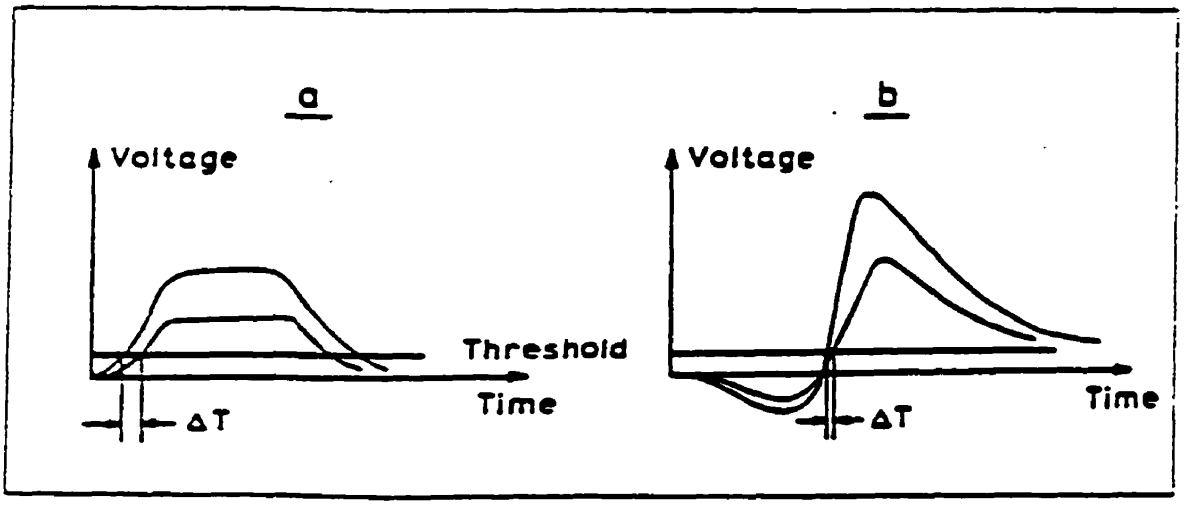

Figure 2.8. Uncertainty in time determination due to different pulse heights by: a) leading edge and b) constant fraction.

The signal from the PMT is fed into the constant fraction discriminator, where the time of pulse arrival as well as the pulse height selection takes place [21]. For the latter purpose energy windows are set in the relevant range for the start 1.28 MeV and the stop 511 KeV in the two discriminators. The CFD generates a pulse height independent "time mark" using the constant fraction method. When the input signal of the discriminator exceeds a preset level, the discriminator circuit gives an output pulse. Because of the poor energy resolution of the scintillator crystals (cf Fig.2.7), this will result in a timing jitter for the pulse crossover of the discriminator level (see figure 2.8a) [22], leading to jitter of the TAC output, and hence to poor time resolution. In technical terms this is referred to as leading edge timing and to improve on this disadvantage of the leading edge system a

circuit was designed, known as the constant fraction discrimination. In this method the input signal is split into two signals, inverting one, delaying it, subtracting a fraction of the delayed pulse from the original pulse, and detecting when the pulses cross the base line as shown as in figure 2.8b. The amplitude of the negative part is a constant fraction of the positive part, and the fit of the two parts can be adjusted by the walk-adjustment. Walk is the time movement of the output signal from the CFD, relative to its input signal. As shown in figure 2.8b smaller time scatter is achieved than the leading edge system.

After amplification, the signal is fed into a single channel analyzer build into the CFD unit. If the two detected events fall within the selected energy ranges set by lower level and upper level controls in the CFD unit, an output is generated. The proper setting values are extracted from the gamma energy spectrum (see figure 2.7) in the start and stop branch. Only those detected pulses that satisfy these energy requirements and separated within 50ns of each other will be processed by the TAC.

2.4.3. Time To Amplitude Converter (TAC) and Multichannel Analyzer (MCA):

The Ortec 566 Time-to-amplitude converter is an analog to digital converter and is used to measure the time interval between start and stop inputs and generate an output pulse whose height is proportional to the measured time [23]. The outputs from the two CFD's are fed into the TAC unit. The TAC converts the two input signals to an output pulse amplitude that is proportional to the time difference between its input signals. The output of the TAC is fed into the multichannel analyzer (MCA). The channel number (1~ 2048) in the MCA is proportional to the time difference between the start and

stopsignal recorded by the detectors. MCA collects the lifetime distribution of the observed events and produces the so-called lifetime spectrum as shown in figure 2.9.

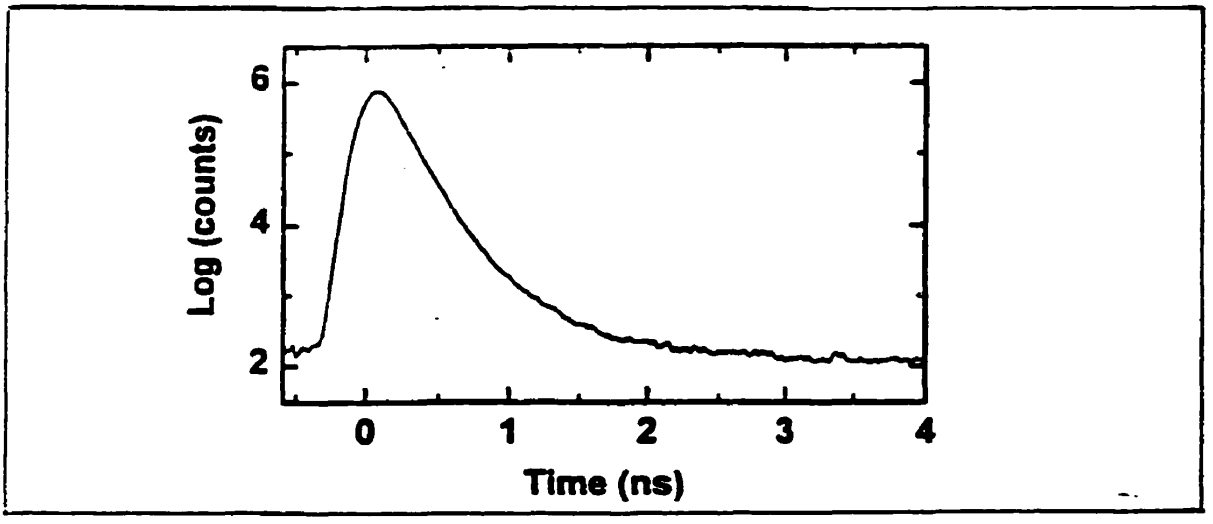

Figure 2.9. Experimentally obtained lifetime spectrum (8×10^{16} counts) for a Ib(syn) diamond sample set.

2.4.4. Resolution function:

The resolution function of a lifetime equipment system is defined as the full-width-at-half-maximum (FWHM) of the so-called prompt curve, which can be determined by using a ^{60}Co source emitting two γ-quanta simultaneously (hence prompt) with energy of 1.17 MeV and 1.33 MeV. Such a spectrum is shown in figure 2.10. In our laboratory the FWHM of the equipments are 170 ~ 220 ps. In the data analysis the resolution function are best determined by using two qaussians as an approximate prompt curve. The second gaussian was displaced typically 30ps to the left of the main gaussian. In order to be able to separate positron lifetimes that are sometimes about 50~70ps a good time resolution of the system is important. The resolution function of the given

system mainly depends on several factors: the geometrical size of the scintillators, energy windows for energy selection and the performance of the timing discriminators. The energy influence is due to the statistical effects (approximately proportional to $(E)^{-1.2}$): the higher the energy, the smaller the statistical variation.

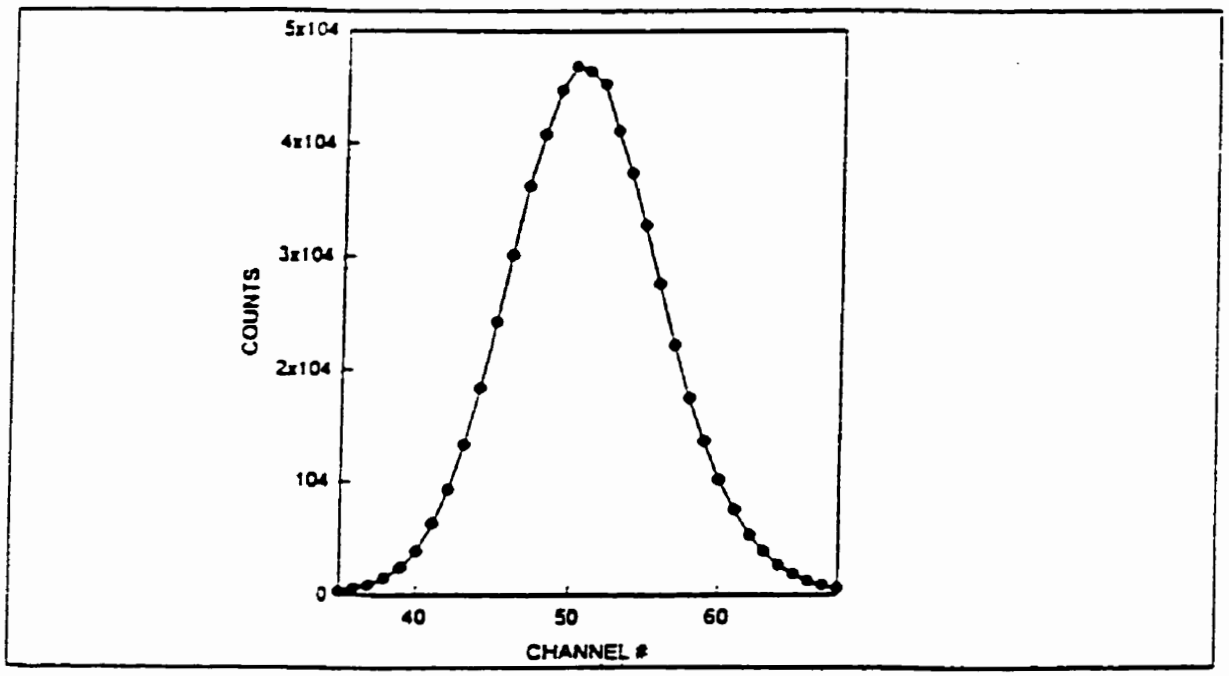

Figure 2.10. Shape of a typical prompt curve for ^{60}Co.

The most important factor is the geometrical size and surface treatment of the scintillator that has the strongest influence on the FWHM of the resolution function, since the collection of the light from the scintillator onto the photocathode of the photomultiplier occurs after numerous reflections from the scintillator walls; for this reason the surface treatment of the scintillator can be expected to influence the resolution. Once the scintillators and the PMT are chosen, the next important factors influence on the time resolution of the system are the triggering of the fast discriminators and the setting of the energy windows for the start and stop quanta. The setting of the windows strongly affects

the FWHM because of the possibility of backscattering effects of γ-quanta into the detectors. By decreasing the width of the windows, one can somewhat reduce the value of the FWHM and thus improve on the time resolution. With care it is possible a to obtain a FWHM of 170ps, a value only 30ps larger than the theoretically minimum resolution value. One of our lifetime spectrometers operates at this value while the other two spectrometers operate at 210 ~ 220 ps due to larger scintillator sizes.

2.4.5. Calibration:

The time calibration consists of the determination of the time difference between two successive channels in the Multi-Channel Analyzer (MCA). This is done by using one of the CFDs. One output is directly connected to the start input of the TAC, the other is connected to a calibrated delay unit, the output of this unit is then connected to the stop input of the TAC. The stop output signal is delayed with respect to the start signal by changing the amount of delay in the delay unit. The relation between delay time and channel number is linear from 25 to 26 ps/channel in our laboratory and accurate to within ± 0.08 ps, depending on the TAC and MCA used for the system.

2.5. Fourier Transform Infrared (FTIR) Spectroscopy:

Fourier transform infrared spectroscopy works basically like a Michelson interferometer. The recording of the detected signal versus optical path difference is the interferogram, which for a polychromatic light source, becomes a superposition for each of the wavelengths. Fourier analysis enables one to convert the interferogram into an absorption spectrum, i.e., absorption versus frequency. The measurements were carried

out at room temperature using a FTIR spectrometer in the spectral range of 600 ~ 4000 cm^{-1} with a spectrometer resolution of 4 cm^{-1}.

2.6. Absorption Measurements in the UV/VIS range:

UV/VIS (Ultra-violet/Visible) absorption was measured at 85 K using a single beam spectrometer. The low temperature of 85 K is necessary in order to resolve the sharp zero-phonon lines used to identify defects by optical measurements. Spectra were obtained within the spectral range of 200nm to 1200nm. The spectra were described in terms of the Beer-Lambert law:

$$\log\frac{I_o}{I} = \alpha d \qquad (2.12)$$

Where I_o and I are the intensities of the incident and transmitted monochromatic light, respectively, and d is the thickness of the sample. The absorption coefficient α is directly proportional to the concentration of the absorbing species.

CHAPTER THREE

ANALYSIS OF THE MEASURED SPECTRA

3.1. Introduction:

When energetic positrons from a radioactive source are injected into the samples (one on each side of the positron source), their kinetic energy distribution is according to a β^- spectrum. This energy is lost by collisions with the atoms of the sample material in a very short time, ($\leq$ 2-5 ps). This slow-down process is called thermalization, during which only a very small portion of positrons annihilates. Since the lifetime of positrons varies from 100 to 500 ps based on the characteristic of each material, the thermalization time is much shorter than the total positron lifetime and can be neglected in positron lifetime measurements. When positrons have reached close to thermal energy, they are normally assumed to occupy only the Bloch state from which they annihilate with a rate λ_B (corresponding to the bulk lifetime, $\tau_B = 1/\lambda_B$) as dictated by the electron density in the bulk of the diamond. However, if vacancies (monovacancies or vacancy clusters) are present, some of the positrons become trapped at these open volume defects before annihilating in the bulk and then annihilate from the trapped state. Since the electron density in the vacancy is less than in the bulk, the positron lifetime becomes longer than the bulk value by an amount which depends mainly on the open volume. Thus, by measuring the time each of the injected positrons lasts for, one can distinguish between those annihilating in the bulk and those annihilating in various vacancy configurations. This requires a collection of several millions of individual annihilation events to produce a lifetime spectrum from which individual lifetimes and intensities of the lifetime components can be extracted (see Fig.2.9).

3.2. Positron Implantation and thermalization:

When an high-energy positron enters a solid material, it is rapidly slowed down until it reaches (near) thermal equilibrium with the surrounding crystal. The depth distribution of thermalized positrons follows an approximately exponential implantation profile:

$$P(z) = \mu \exp[-\mu z] \qquad (3.1)$$

where z is the distance from the surface of the sample, the attenuation constant μ determined mostly by the endpoint E_{max} of the β^+-spectrum and the density ρ of the material, is given by:

$$\mu \approx \frac{16\rho}{E_{max}^{1.4}} \qquad [\mathrm{cm}^{-1}] \qquad (3.2)$$

where ρ is in the unit of gr/cm^3 and E_{max} in MeV.

The most common isotope for positron lifetime and Doppler-broadening experiments is ^{22}Na with $E_{max} = 0.54$ MeV. For this isotope the average penetration depth $1/\mu$ is 110 μm in Si, 50 μm in Ge, 14 μm in W and 80μm in diamond. Thus the ^{22}Na positron source is only suitable for bulk studies and can not practically be used for investigations of thin films (≤10 μm) or surfaces, although positron beams with controlled low energy (keV range) can be used in such cases.

3.3. Annihilation Characteristics:

If positrons annihilate from a state localized at a vacancy-type defect, the positron lifetime changes from the bulk value due to the change in the electronic environment. In the absence of electrons the positron is a stable particle, but in an environment of

electrons the positron has a finite lifetime τ. The positron lifetime is the inverse of the annihilation rate:

$$\tau = \frac{1}{\lambda} \qquad (3.3)$$

The positron annihilation rate λ is determined by the overlap of the positron wave function with the electron wave functions and depends therefore on the electron density at the annihilation sites, and is given by:

$$\lambda = \pi r_e^2 c \int d\bar{r} |\Psi_+(\bar{r})|^2 n(\bar{r}) \gamma[n(\bar{r})], \qquad (3.4)$$

where r_e is the classical electron radius, c the speed of light, $n(\bar{r})$ the electron density and $\gamma[n(\bar{r})]$ the short-range enhancement factor of the electron density at the site of the positron. There are various interpolation formulas for $\gamma[n(\bar{r})]$ based on many-body calculations, and $\gamma[n(\bar{r})]$ has numerical values that make very significant contributions to λ. In each positron state i, the posiron probes different electron densities leading to different lifetimes $\tau_i = 1/\lambda_i$. Due to the decrease of the overlap between the localized positron and electron densities at the vacancy, the trapped-positron lifetime is increased compared to free positrons.

3.4. Positron Trapping:

If point defects of vacancy type are present in a material, the positron will tend to occupy these defects (positron trapping) and localization takes place as described for the first time by Goldanskii in 1966 [24] for point defects in alkali halides.

Positron trapping can be divided into two categories: Deep trapping and shallow trapping. Deep traps are characterized by a binding energy that is much larger than the

thermal energy at 300K (~ 1/40 eV) while shallow traps constitute traps with comparable energies. For deep traps, such as vacancy-type defects, the binding energy is normally about 1 eV. Such traps are so deep that thermal escape is not possible to occur. Shallow traps can be dislocations which have little open volume or negatively charged impurities that provide Rydberg-like states for the positively charged positron, much like shallow acceptors in semiconductors.

3.5. Trapping Model:

The changes of the annihilation characteristics as a function of the trap concentration are described by the so-called trapping model [25,26]. The trapping in a homogeneous solid is described by kinetic equations (called rate equations). In an inhomogeneous medium, the time-dependent diffusion equation is needed. The kinetic equations were first introduced by Brandt [27] in 1967. Later they were used by Bergersen and Stott [28], and Connors and West [29] to analyze positron trapping at thermal vacancies. The current theories of trapping model are mainly based on the treatment given by them.

The trapping model is based on the following some assumptions:

i) At time t = 0 all positrons are in the delocalized (Bloch) states.

ii) When defects are present the positrons are transferred from the Bloch state (commonly referred to as the Bulk state) to the defect with a certain rate κ_i. κ_i is called the trapping rate, which is proportional to the defect concentration c_i:

$$\kappa_i = \mu_i c_i \qquad (3.5)$$

where i refers to the type of defects, c_i is the number of defects of type " i " per unit volume and μ_i is called the specific trapping rate.

iii) The positron may escape from a trap. The detrapping rate is denoted by δ.

If there are N different defects, we get a set of linear differential equations:

$$\frac{dn_B}{dt} = -\left(\lambda_B + \sum_{i=1}^{N} \kappa_i\right) n_B + \sum_{i=1}^{N} \delta_i n_{Di} \qquad (3.6)$$

$$\frac{dn_{Di}}{dt} = \kappa_i n_B - (\lambda_{Di} + \delta_i) n_{Di} \qquad (i = 1, 2, \ldots, N), \qquad (3.7)$$

where n_B is the probability of the positron to be in the free state (Bulk state) and n_{Di} is the probability of the positron to be in the " i-th " defect. λ_B is the annihilation rate in the Bulk state and λ_{Di} is in the " i-th " defect state. $\sum_{i=1}^{N} \kappa_i$ is the total trapping rate due to the different type of defects.

The first term in equation (3.6) is the disappearance of positrons from the Bulk state by annihilations. The second term takes into account the disappearance from the Bulk state by the transfer to trapped states. The third term is the detrapping from trapped states back into the Bulk state. The equation (3.7) represents the occupation probability for the defect.

The boundary condition from assumption i) is

$$n_B(0) = 1\,, \qquad n_{Di}(0) = 0 \qquad (i = 1, 2, \ldots, N) \qquad (3.8)$$

In the case of no detrapping ($\delta_i = 0$, i = 1, 2, ..., N) the solution of equations (3.6) and (3.7) can be analytically written in the form:

$$n_B(t) = \exp\left[-\left(\lambda_B + \sum_{i=1}^{N} \kappa_i\right)t\right] \qquad (3.9)$$

$$n_{Di}(t) = \frac{\kappa_i}{\lambda_B - \lambda_{Di} + \sum_{i=1}^{N} \kappa_i}\left\{\exp(-\lambda_{Di}t) - \exp\left[-\left(\lambda_B + \sum_{i=1}^{N} \kappa_i\right)t\right]\right\} \qquad (3.10)$$

The total occupation probability, or the probability for a positron to be alive (i.e. has not annihilated) at time t is given by

$$n(t) = n_B(t) + \sum_{i=1}^{N} n_{Di}(t)$$

$$= \left(1 - \sum_{i=1}^{N} \frac{\kappa_i}{\lambda_B - \lambda_{Di} + \sum_{i=1}^{N} \kappa_i}\right)\exp\left[-\left(\lambda_B + \sum_{i=1}^{N} \kappa_i\right)t\right] +$$

$$+ \sum_{i=1}^{N} \frac{\kappa_i}{\lambda_B - \lambda_{Di} + \sum_{i=1}^{N} \kappa_i}\exp(-\lambda_{Di}t) \qquad (3.11)$$

The form of equation (3.11) is particularly useful in relating the trapping rates and annihilation rates, which are the physical parameters that contain information about the sample, to the experimentally measured lifetimes and intensities. In equation (3.11) terms in front of the exponential are called the intensities of the lifetime components.

The lifetime spectrum is the probability for annihilation at time t and has the general form:

$$-\frac{dn(t)}{dt} = \sum_{i=1}^{N+1} I_i \lambda_i \exp(-\lambda_i t) \qquad (3.12)$$

Thus,

$$n(t) = \sum_{i=1}^{N+1} I_i \exp(-\lambda_i t) \qquad (3.13)$$

where λ_i is the annihilation rate and I_i the relative intensity. From the equations (3.11) and (3.13) by comparing terms we can obtain:

$$\lambda_1 = \lambda_B + \sum_{i=1}^{N} \kappa_i \qquad (3.14)$$

$$\lambda_{i+1} = \lambda_{Di} \qquad (3.15)$$

The following sum rules can be deduced:

$$n(0) = \sum_{i=1}^{N+1} I_i = 1 \qquad (3.16)$$

$$-\left.\frac{dn(t)}{dt}\right|_{t=0} = \lambda_B = \sum_{i=1}^{N+1} I_i \lambda_i \qquad (3.17)$$

$$\tau_{avg} = \int_0^\infty dt\left(-\frac{dn}{dt}\right)t = \int_0^\infty dt\, n(t) = \sum_{i=1}^{N+1} I_i \tau_i$$

$$= \frac{1 + \sum_{i=1}^{N} \kappa_i \lambda_{Di}}{1 + \sum_{i=1}^{N} \kappa_i \tau_B} \tau_B \qquad (3.18)$$

According to the basic assumption in the trapping model, all positrons occupy the Bulk state at time t = 0. The positrons can be transferred at a rate κ (the trapping rate) from the Bulk state to a vacancy. Thus, positrons will disappear from the Bulk by both annihilations as well as transfer to vacancies.

Following we will consider some simple cases:

1) One type of defects, no detrapping. – This is the model most frequently applied.

We have the kinetic equations:

$$\frac{dn_B}{dt} = -\lambda_B n_B - \kappa n_B \qquad (3.19)$$

$$\frac{dn_D}{dt} = \kappa n_B - \lambda_D n_D \qquad (3.20)$$

The solution with the boundary condition $n_B(0)=1, n_D(0)=0$ is

$$n_B(t)=\exp[-(\lambda_B+\kappa)t] \qquad (3.21)$$

$$n_D(t)=\frac{\kappa}{\lambda_V+\kappa-\lambda_D}\{\exp(-\lambda_D t)-\exp[-(\lambda_B+\kappa)t]\} \qquad (3.22)$$

$$n(t)=n_B(t)+n_D(t)$$

$$=\frac{\lambda_B-\lambda_D}{\lambda_B-\lambda_D+\kappa}\exp[-(\lambda_B+\kappa)t]+\frac{\kappa}{\lambda_B-\lambda_D+\kappa}\exp(-\lambda_D t). \qquad (3.23)$$

The decomposition of the lifetime spectrum gives λ_1, λ_2, I_1, I_2 as experimental parameters;

$$n(t)=I_1\exp(-\lambda_1 t)+I_2\exp(-\lambda_2 t) \qquad (3.24)$$

Thus we find by comparing terms relations:

$$I_1=1-\frac{\kappa}{\lambda_B-\lambda_D+\kappa}=\frac{\lambda_B-\lambda_D}{\lambda_B-\lambda_D+\kappa} \qquad (3.25)$$

$$I_2=\frac{\kappa}{\lambda_B-\lambda_D+\kappa}=1-I_1 \qquad (3.26)$$

$$\lambda_1=\frac{1}{\tau_1}=\lambda_B+\kappa, \quad \lambda_2=\frac{1}{\tau_2}=\lambda_D, \qquad (3.27)$$

$$\lambda_B=I_1\lambda_1+I_2\lambda_2 \qquad (3.28)$$

$$\tau_{avg}=I_1\tau_1+I_2\tau_2=\frac{1+\kappa\tau_D}{1+\kappa\tau_B}\tau_B \qquad (3.29)$$

$$\tau_1=\frac{\tau_D-\tau_{avg}}{\tau_D-\tau_B}\tau_B, \qquad \lambda_1=\frac{1}{I_1}(\lambda_B-I_2\lambda_D), \qquad (3.30)$$

$$I_2 = \frac{\tau_{avg} - \tau_1}{\tau_2 - \tau_1} \qquad (3.31)$$

$$\kappa = \frac{I_2}{I_1}(\lambda_B - \lambda_D) = I_2(\lambda_1 - \lambda_D) = \frac{\tau_{avg} - \tau_B}{\tau_D - \tau_{avg}} \frac{1}{\tau_B} \qquad (3.32)$$

2) Two types of defects, no detrapping.

We can obtain relations:

$$\lambda_1 = \lambda_B + \kappa_1 + \kappa_2, \quad I_1 = 1 - I_2 - I_3, \qquad (3.33)$$

$$\lambda_2 = \lambda_{D1}, \qquad I_2 = \frac{\kappa_1}{\lambda_B - \lambda_{D1} + \kappa_1 + \kappa_2}, \qquad (3.34)$$

$$\lambda_3 = \lambda_{D2}, \qquad I_3 = \frac{\kappa_2}{\lambda_B - \lambda_{D2} + \kappa_1 + \kappa_2}, \qquad (3.35)$$

where κ_1 and κ_2 are the trapping rates for defects 1 and 2.

3) One type of defects with detrapping.

$$n(t) = \frac{\lambda_B - \lambda_2}{\lambda_1 - \lambda_2}\exp(-\lambda_1 t) + \frac{\lambda_1 - \lambda_B}{\lambda_1 - \lambda_2}\exp(-\lambda_2 t) \qquad (3.36)$$

$$\lambda_{1,2} = \frac{1}{2}\left\{\lambda_B + \lambda_D + \kappa + \delta \pm \left[(\lambda_B + \kappa - \lambda_D - \delta)^2 + 4\kappa\delta\right]^{1/2}\right\} \qquad (3.37)$$

The above decay models lead to fairly simple solutions, although the last model, which includes detrapping, hints at significant complications. Later in this thesis will be considered a model pertinent to trapping by negatively charged vacancies and such a model results in a very much more complicated set of solutions for the observable lifetimes and intensities.

3.6. Important Remarks:

In this section we will focus on some important points for positron annihilation relevant to our this work.

The rate at which positrons are trapped by vacancies, κ, is normally assumed proportional to the vacancy concentration $[C_V]$ according to $\kappa = \mu \cdot [C_V]$. The constant of proportionality is strongly influenced by the charge state of the vacancy. If neutral, $\mu = \mu^0$ is temperature independent, but if negatively charged, $\mu = \mu^-$ is larger than μ^0 due to the Coulomb attraction between the vacancy and the positron, and is also temperature dependent [68]. On the other hand, positively charged vacancies are much less efficient traps for positrons due to the Coulomb barrier.

In addition to lifetime measurements, the electron momentum distribution can be investigated by means of the Doppler broadening of the 511 keV annihilation line (see chapter two, 2.3). What is measured is the Doppler broadening caused by the 3-dimensional electron momentum distribution projected onto the viewing direction between the samples and the detector, and since the momentum distribution normally is anisotropic, this broadening depends on the crystallographic direction pointing toward the detector.

An issue which is of importance in this work is the difference in sensitivity to the vacancy concentration between lifetime and Doppler broadening measurements. When positrons are trapped by vacancies, the experimentally determined rate of disappearance of positrons from the bulk is $(\lambda_B + \kappa)$, according to equation (3.21), where, again, λ_B is the bulk annihilation rate and κ is the vacancy-concentration-dependent rate by which positrons are transferred from the bulk to the vacancy. Thus, the fraction of positrons

trapped in vacancies is $\kappa/(\lambda_B+\kappa)$. As the trapped fraction increases, so does the intensity of the lifetime component associated with the trap.

For experimental reasons a combined rate larger than $\cong 25ns^{-1}$ is impossible to resolve in a lifetime spectrum. Therefore, with $\lambda_B \cong 10ns^{-1}$ (for diamond), the maximum measurable κ value would be about 15 ns^{-1}. In Doppler measurements the situation is quite different. The measured value for S is composed of the contributions from the fractions of positrons annihilating in the bulk and in the vacancies with parameters S_B and S_V respectively so that $S=(1-\frac{\kappa}{\lambda_B+\kappa})S_B+\frac{\kappa}{\lambda_B+\kappa}S_V$. For increasing κ values S therefore approaches S_V and, assuming that one can experimentally determine S/S_B to within an uncertainty of $\cong 5\%$, the upper limit for detecting changes in S occurs for a κ value of $\cong 200$ ns^{-1}, i.e., at least one order of magnitude higher than for lifetime measurements.

3.7. Positronfit:

The positron lifetime spectra are analyzed by a computer program in terms of a number of exponential terms and a constant background all convoluted with the instrumental resolution function. At our laboratory we used the computer program developed by Kirkegard and Eldrup [30], named Resolution. This program extracts lifetimes and intensities from lifetime spectra by making use of least-squares techniques. It fits a parameterized model function to a distribution of experimental data points y_i (y_i denotes the counts recorded in each channel " i "), and seeks values of the model parameters $b_1, \ldots, b_k$ to minimize;

$$\chi^2 = \sum_{i=1}^{n} w_i [y_i - f_i(b_1,...,b_k)]^2, \qquad (3.38)$$

where n is the number of data points, $f_i(b_1,...,b_k)$ the model prediction for point numbers i, and w_i the " statistical weight " at this point i.

$$w_i = \frac{1}{\sigma_i^2} \qquad (3.39)$$

where σ_i is the standard variance of the count number at the data point i. In the case of the Poisson distribution, a perfect fit χ^2 will equal one and should therefore serve as an indicator of the validity of the assumed model, in which the most important assumption made is the number of lifetime components present in the lifetime spectrum. Newer programs are aiming at removing this assumption, i.e. directly identifying the number of lifetimes, their values and intensities; They are, however, still in the developing stages.

In the Resolution program, the model function consists of a sum of decaying exponentials convoluted with the resolution function of the lifetime spectrometer plus a constant background. Let k_0 be the number of lifetime components, a_j the decay function for component j, R the time-resolution function and B the background. Then the model spectrum is given by:

$$f(t) = \sum_{j=1}^{k_0} (a_j * R)(t) + B, \qquad (3.40)$$

$$a_j(t) = A_j \exp\left(-\frac{t}{\tau_j}\right), \qquad \text{for} \quad t > 0 \quad \text{and} \qquad (3.41)$$

$$a_j(t) = 0, \qquad \text{for} \quad t < 0 \qquad (3.42)$$

where τ_j is the lifetime of the j-th component, and $A_j\tau_j$ is the intensity of the j-th component. R(t) is assumed to be a sum of k_g Gaussians which may be displaced with respect to each other:

$$R(t)=\sum_{p=1}^{k_g} w_p G_p(t), \qquad (3.43)$$

$$G_p(t)=\frac{1}{\sqrt{2\pi}\sigma_p}\exp\left[-\frac{(t-T_0-\Delta t_p)^2}{2\sigma_p^{\,2}}\right] \qquad (3.44)$$

$$\sum_{p=1}^{k_g} w_p = 1 \qquad (3.45)$$

The Gaussian $G_p(t)$ is centered around channel number $T_0+\Delta t_p$, where T_0 is the time-zero channel number, i.e. the channel number at which two simultaneously emitted γ rays would be detected by the equipment, and Δt_p a displacement. The standard deviation σ_p of the Gaussian is related to its FWHM by;

$$FWHM_p = 2(2\ln 2)^{1/2}\sigma_p \qquad (3.46)$$

The model spectrum $f(t)$ is a continuous curve, while the spectra is recorded in channels of a multi-channel analyser. For proper comparation the curve $f(t)$ shall therefore be transformed into a histogram by integration over the width of each channel. The model count distribution fitted to the measured spectrum is given by:

$$f_i = \int_{t_i}^{t_i+1} f(t)dt \qquad (3.47)$$

where t_i is the value of t at the common limit of channel number i-1 and i. Here we assume equidistant channel widths and $t_{i+1}-t_i=1$; in this way the integrated count

becomes the channel average. Thus, we obtain a model for the least-squares analysis of the form:

$$f_i = \sum_{j=1}^{k_0} F_{ij} + B \qquad (3.48)$$

where F_{ij} is the value from lifetime component j in spectral channel i.

The fitting parameters in Positronfit are the lifetimes τ_j, the relative intensities $I_j = \frac{A_j \tau_j}{\sum_{k=1}^{k_0} A_k \tau_k}$, time-zero T_0, and the resolution function. The programme allows for fixing some of these parameters, but that would require a physical insight; The background, B, is determined directly by experiment and is, therefore, not an adjustable parameter.

In our work, the resolution function $R(t)$ is well approximated to be a superposition of two Gaussians, one as a main (~80%) Gaussian centered at T_0, and the second (~20%) Guassian was slightly offset (by typically 30 ps) from the main Gaussian. B is chosen in the fitting procedure to the average value of at least 500 channels in the background region of each spectrum.

The number of lifetime components is usually determined by the minimum number of components that yield a good χ^2 value in the fitting procedure. Generally, fits are performed with between two and four lifetimes. A value of $\chi^2 = 1.00 \pm 0.06$ indicates that the chosen model is in perfect statistical agreement with the experimental data, and fits are accepted when they are within 1 ± 0.12 to allow for experimental effects

such as instrumental time-zero drift and small (but unknown) deviations from the mathematical model employed.

The final results of the fits are values of lifetimes, relative intensities, background, time-zero-channel and resolution function parameters and all of these parameters are evaluated with their standard deviations.

CHAPTER FOUR

BASIC CONCEPTS OF DEFECTS AND DIAMONDS

4.1. Defects in Materials:

Defects play an important role in determining the physical properties of most crystalline substances. Defects can affect the crystal's intrinsic electronic and optical properties, especially the carrier concentration. Characterization of defects is extremely important in regards to the performance of semiconductor devices because the quantity of defects, which are necessary to significantly change the properties of a semiconductor, are less than one defect per million regular lattice atoms.

Defects in crystals are the imperfections in the crystal lattice arrangements, and arise from deviations of the atoms from their ideal lattice sites. They can be classified as point defects, linear defects, planar defects, and volume defects.

i) Point defects:

There are the smallest defects of atomic size, i.e. chemical impurities, vacant lattice sites (lattice vacancies), and extra atoms not in regular lattice positions.

ii) Linear defects:

Linear imperfections are known as a dislocation. There are two basic types: edge dislocations and screw dislocations. One important aspect of linear defects is that they are potential traps for point defects.

iii) Planar defects:

Planar imperfections are the result of errors in the stacking sequence of crystal atomic planes.

iv) Volume defects:

These defects are usually agglomerates of point defects, so creating voids or clusters of interstitials.

4.2. Point Defects:

The point defects are the smallest defects. Their size is typically in the order of atomic sizes. They can exist in many different forms: vacancy, interstitial, impurity, etc. They occur mainly during the following circumstances.

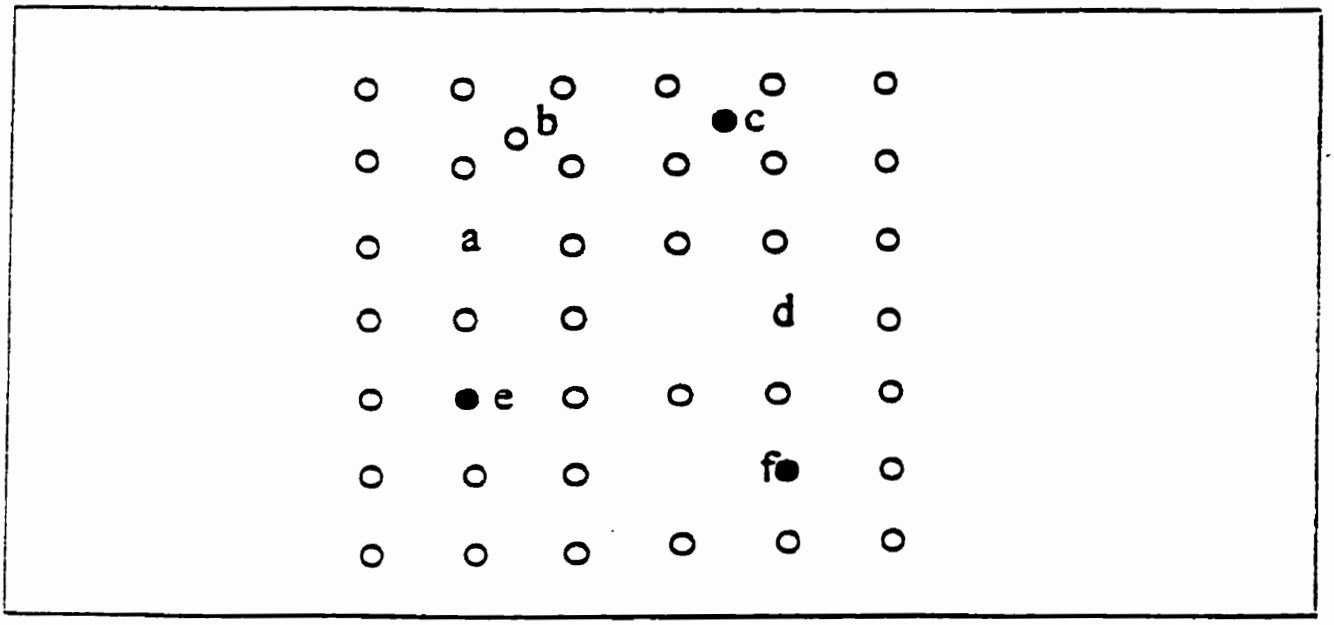

Figure 4.1. Schematic representation of simple point defects: a) Vacancy; b) Self interstitial; c) Interstitial impurity; d) Divacancy; e) Subtitutional impurity; f) Vacancy substitutional impurity complex.

i) An atom is removed from its regular lattice site (vacancy).

ii) An atom is not at its regular lattice site, but has moved into the region between lattice sites, so the defect is an interstitial. It can involve either one of the host atoms (an self-interstitial) or an impurity atom (an extrinsic defect).

iii) An impurity occupies a substitutional site.

Various kinds of defects are also formed by the association of intrinsic or extrinsic, substitutional or interstitial defects. As a special case, an interstitial defect occurs when a vacancy is formed by transferring a host atom from a lattice site to an interstitial position. This type of disorder is called a Frenkel pair. All these various types of defects are schematized in figure 4.1 [31].

4.3. Geometrical Configuration of Point Defects:

4.3.1. The Vacancy:

When an atom is removed from its regular lattice site, the formed defect is called a vacancy also known as Schottky defect (figure 4.2).

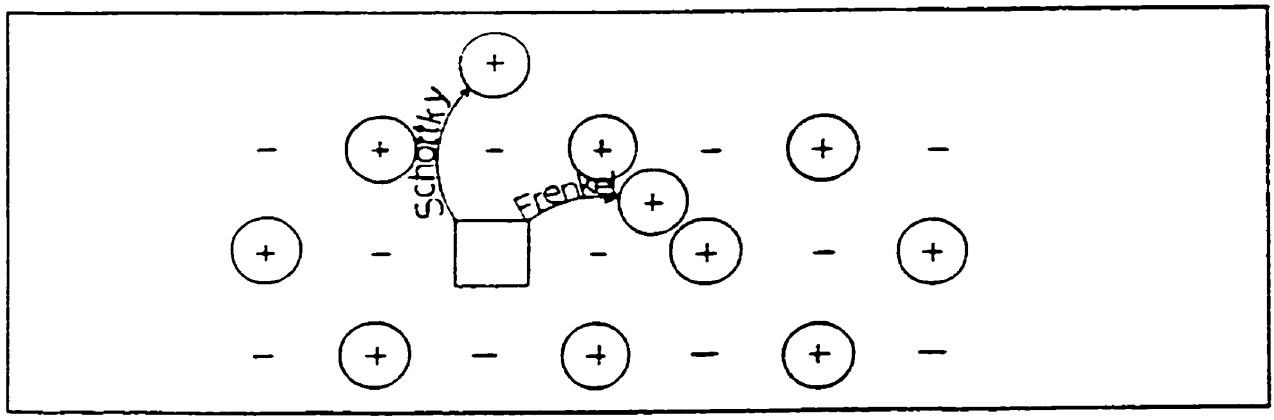

Figure 4.2. Schottky and Frenkel defects in an ionic crystal. The arrows indicate the displacement of the ions.

In a group IV semiconductor four bonds are broken when a vacancy is created. The broken (dangling) bonds will be rearranged and form new bonds which may lead to atomic displacements. These new bonds depend on the charge state of the vacancy, i.e., on the number of electrons that occupy these dangling bonds. Figure 4.3 [31] shows a vacancy in diamond lattice structure.

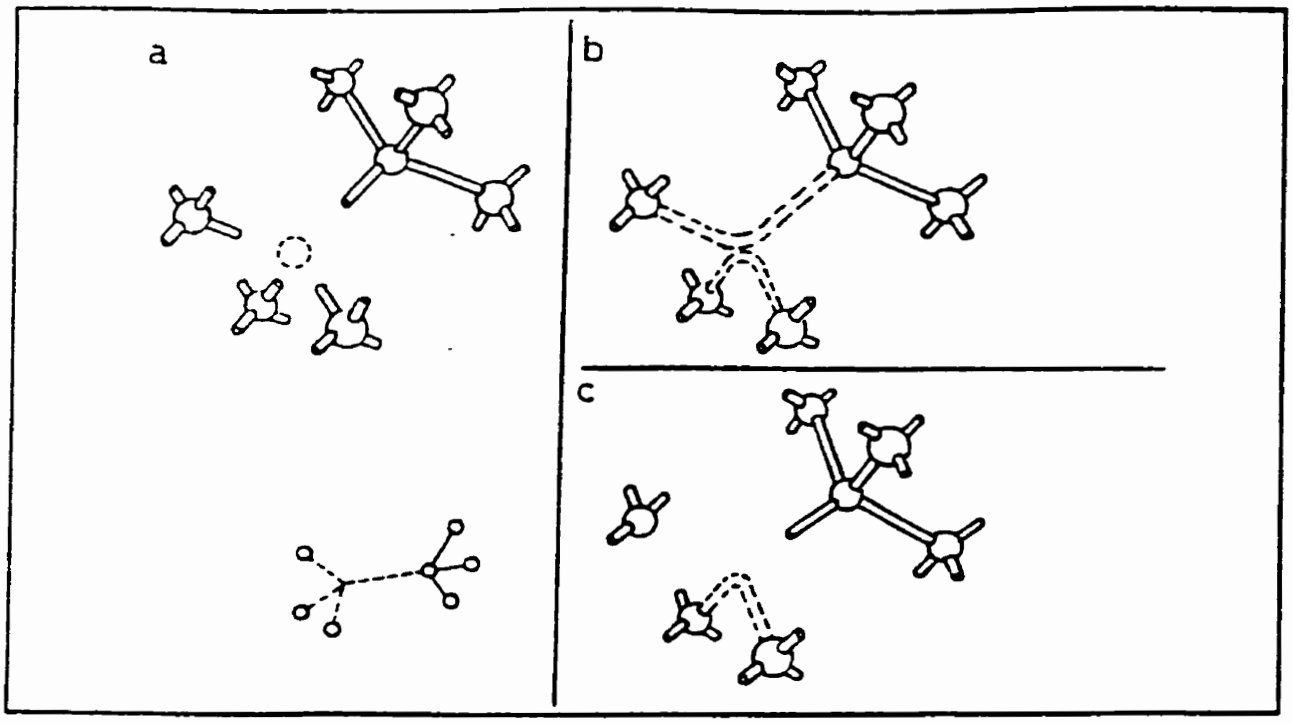

Figure 4.3. The monovacancy in diamond lattice. a) Four bonds are broken; b) V^0; c) V^+.

In (a) four bonds are broken in order to create the vacancy. (b) for the neutral vacancy V^0 there is one electron per dangling bond, they form two new bonds. (c) when an electron is missing (a positively charged vacancy V^+), one of these two bonds is weakened since it contains only one electron. The distortion in the case of V^+ is thus different from that in the case of V^0. The monovacancy has five charged states: $V^=$, V^-, V^0, V^-, and V^{++}.

4.3.2. The Divacancy:

Removing two adjacent atoms as shown in figure 4.4[31] forms the divacancy.

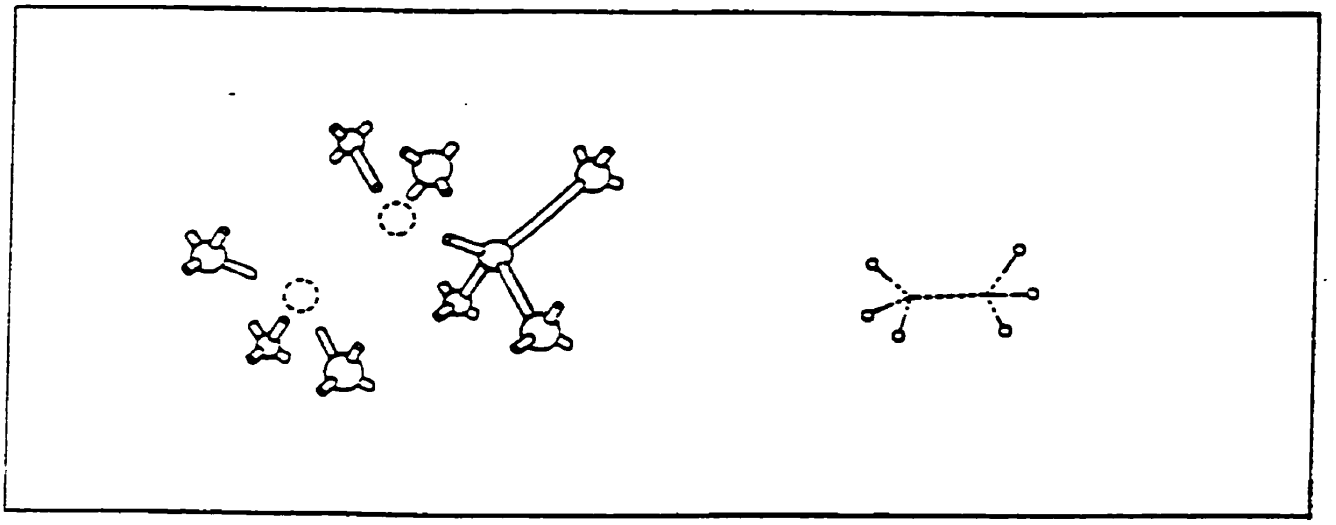

Figure 4.4 The divacancy configuration and its schematic two dimension-representation.

Actually, a divacancy may be seen as two nearest neighbor vacancies. It is possible to be produced directly by irradiation and heat treatment. In this case new localized electron states is V_2^+, V_2^0, V_2^-, and $V_2^=$.

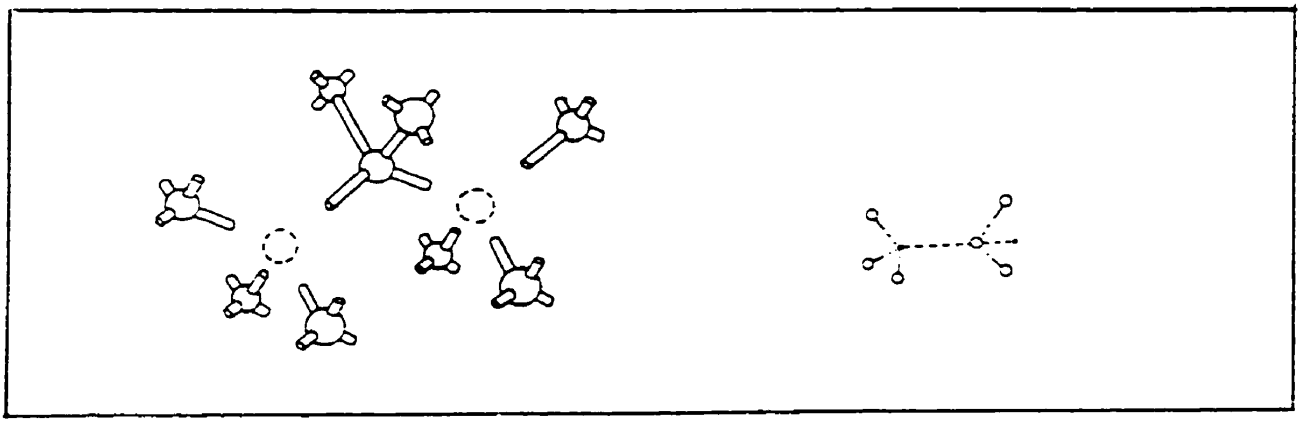

Figure 4.5. The split-divacancy configuration and its schematic representation.

In order to understanding, figure 4.5[31] shows the split-divacancy configuration, corresponding to the configuration of the divacancy in the saddle point for the migration.

4.3.3. The Interstitial:

A lattice atom is removed from its regular lattice site and transferred into a position that is not a regular lattice site. Such a position is referred to an interstitial position and the atom is called the interstitial atom.

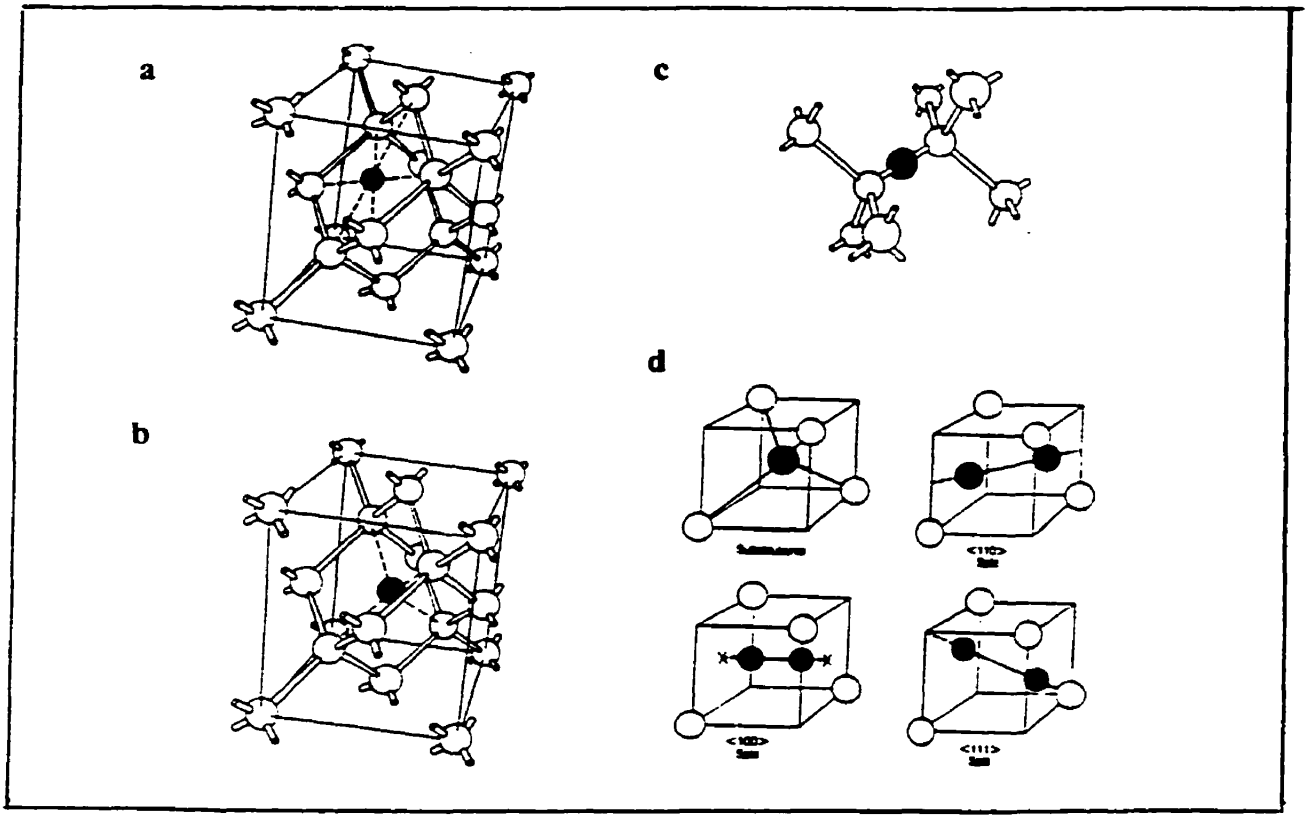

Figure 4.6. Different interstitial configurations in Diamond lattice. a) The hexagonal; b) The tetrahedral; c) The bond-centered; d) some split interstitial configurations.

These defects can involve either one of the host atom (self-interstitial) or an impurity atom or dopant. These defects are easily formed in semiconductors as a consequence of irradiation damage, but in many cases interstitials are mobile even at very low temperatures. It is still not possible to decide what are the stable sites for an interstitial atom, and also understand what is the mechanism of interstitial migration. But if

considering total electronic energy and symmetry, it is reasonable to say that some of the high-symmetry sites are the most stable interstitial positions.

In the diamond lattice, the high-symmetry sites correspond to the hexagonal and tetrahedral sites and the " bond-centered " configuration (the interstitial sits at the center of the bond) as can be seen in figure 4.6[31].

4.3.4. Complex Defects:

When a simple defect moves, for example, due to the heat treatment, it can interact with other intrinsic as well as extrinsic point defects giving rise to a more stable complex defects. When the vacancy becomes mobile in silicon, it can be trapped by an oxygen interstitial impurity (present in Cz-silicon due to its grown process) and form a V-O pairs (which are, essentially, substitutional oxygen).

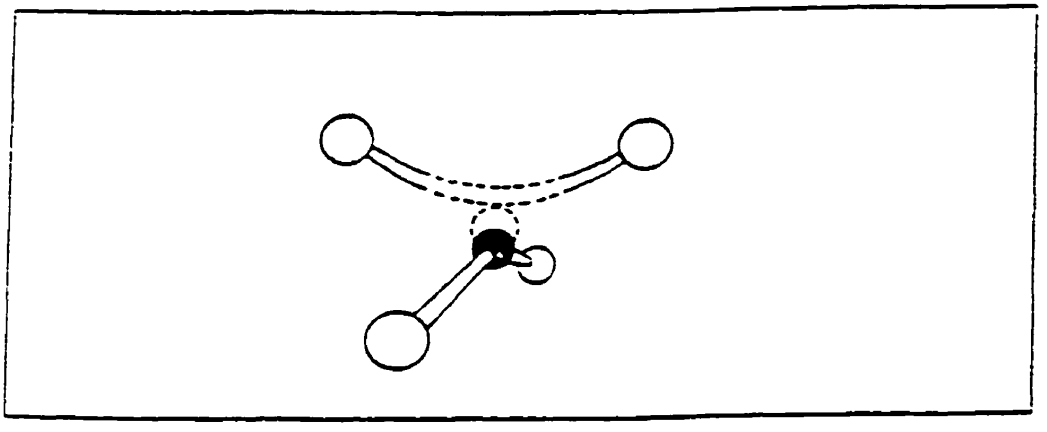

Figure 4.7. Vacancy-oxygen complex. the oxygen atom is slightly displaced off the substitutional position.

In diamond, vacancies, produced by the irradiation, are trapped by the single N atoms, and form nitrogen-vacancy complex pairs. In another case the vacancy can capture another vacancy to form divacancies. Figure 4.7[31] gives the configuration of vacancy-

oxygen pair in Cz-silicon in which the oxygen atom is slightly displaced off the substitutional vacancy position.

4.3.5. Aggregates:

The defects, with high concentration in a material, tend to aggregate as the temperature is increased as facilitated by long-range migration process. In many cases, it is possible to produce vacancy aggregates by prolonged radiation and heat treatment. Vacancies form divacancies that upon further heating start to move, forming larger vacancy aggregates, such as trivacancies, quadrivacances, etc. The agglomerated defect can have several possible configurations. Figure 4.8[31] gives one of the possible configurations for a penta-vacancy.

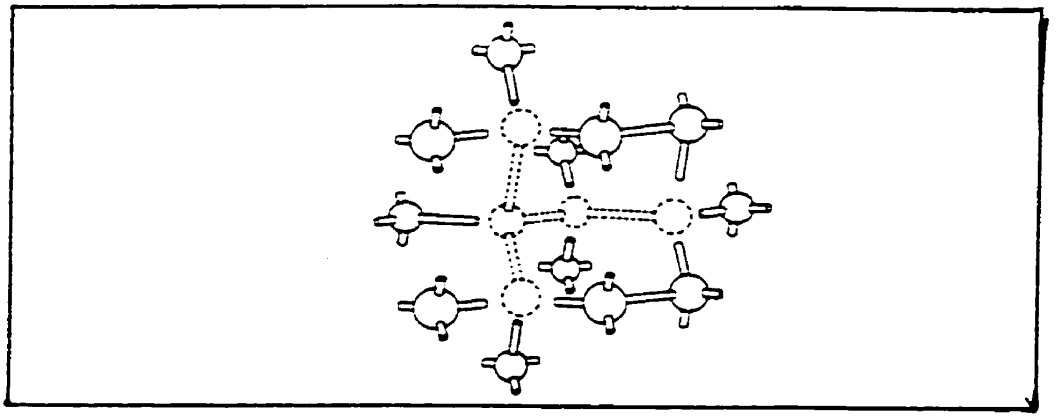

Figure 4.8. One of the possible configurations for a penta-vacancy.

4.4. Diamond:

4.4.1. Structure of Diamond:

Carbon atoms can form two solid states graphite and diamond. Graphite is thermodynamically the most stable form, but under appropriate conditions diamond crystals can be formed. The carbon atom has four electrons in the n=2 shell, which can hold up to eight. Two carbon atoms can link together by sharing an electron from one. Each carbon atom can link with four others and form four bonds; i.e. it has a valence of four. Such bonds are called covalent and can hold atoms together so that they form geometrical lattice structures. The four bonds to each atom are not flat, but are at 109.5^0 to each other as shown in figure 4.9a. Each atom is at the geometric center of four others, which are at the corners of an imaginary tetrahedron. Every bond is 1.544-Angstrom long. The linking of a number of carbon atoms in this way into a three-dimensional diamond lattice can be seen in figure 4.9b[33]. One layer is shown shaded to draw attention to the puckered hexagonal rings of atoms that result from the structure.

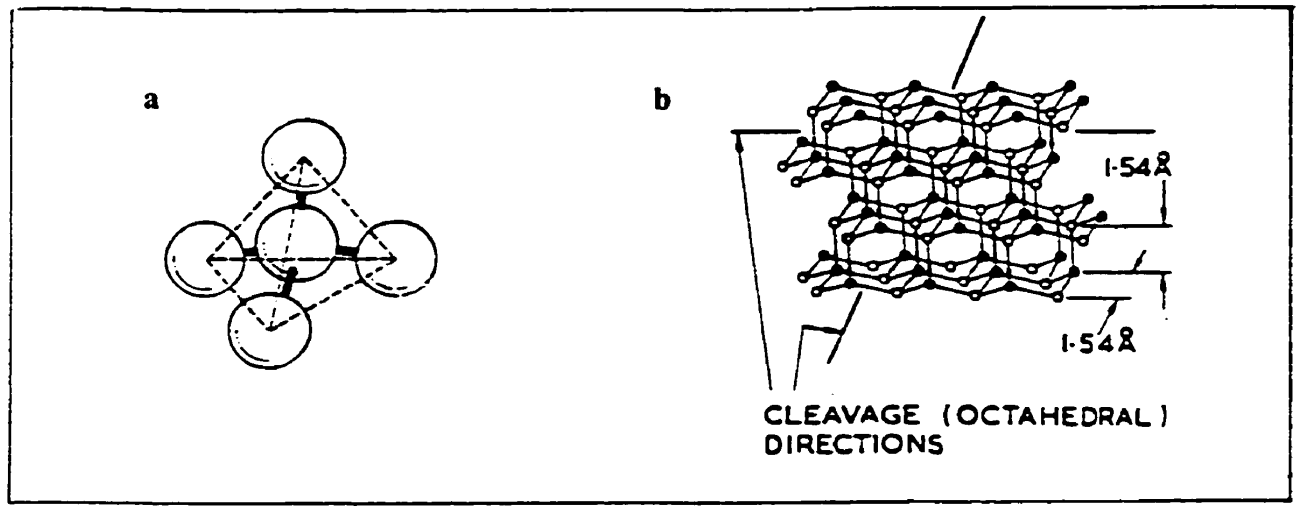

Figure 4.9. a) Tetrahedral bonds of the carbon atoms: b) Structure of diamond. Two of the three cleavage directions are shown.

It is conventional in crystallography to represent a crystal by a space lattice that is a model of the unit cells of the same shape that make up the crystal. The space lattice of

diamond is face-centered cube (FCC). The primitive basis has two identical atoms at 000; $\frac{1}{4}\frac{1}{4}\frac{1}{4}$ associated with each point of the Fcc lattice. Thus, the conventional unit cube contains eight atoms. The tetrahedral bonding characteristic of the diamond structure is shown in figure 4.10. It may be viewed as two FCC structures displaced from each other by one-quarter of a body diagonal. Each atom has 4 nearest neighbors and 12 next nearest neighbors. Many of physical properties can be related to the atomic lattice of diamond. As there are no free electrons or holes in a perfect diamond crystal lattice, diamond has high resistance to the passage of electricity. The lattice of diamond is exceptionally strong, which results in its extreme hardness and resistance to deformation, as well as to a large band gap (5.5 eV).

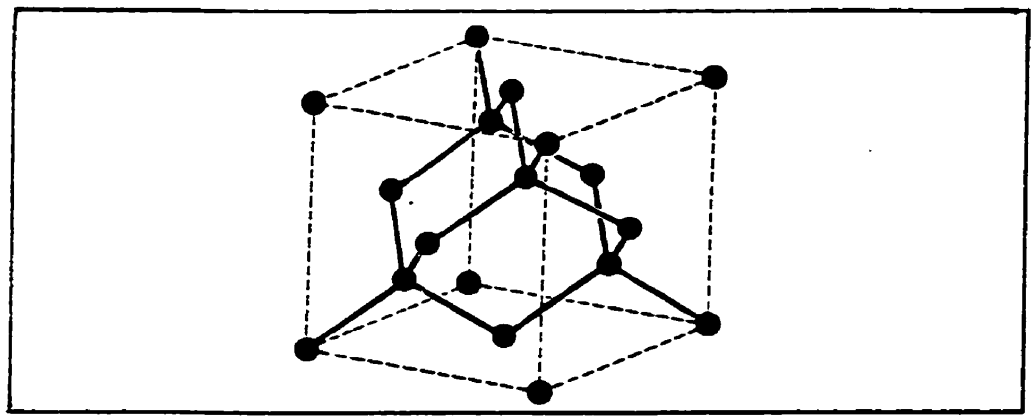

Figure 4.10. Crystal structure of diamond, showing the tetrahedral bond arrangement.

4.4.2. The ' type ' terminology for diamond:

At the beginning of the twentieth century it was discovered that diamonds fell broadly into two categories, which were called type I and type II. On the account of showing distinct differences in their transparency to ultra-violet light and infrared light. Type I diamonds absorbed ultra-violet strongly from about 330 nm and showed absorption bands in the infrared. Type II diamonds transmitted ultra-violet light down to about 220 nm and showed no absorption bands in the infrared [32,33]. Later it became clear that impurity nitrogen atoms were the cause for these differences [34]. Type I diamonds can be broadly defined as those with nitrogen in their structure and type II diamonds as those without. More refined spectroscopic measurements led to a subdivision of the types, such as Ia, Ib, IIa and IIb. These shorthand notations are still widely used today, and are detailed below.

1) Type I:

All type I diamonds contain relatively substantial amounts of nitrogen (> 100 ppm). Type I diamonds are subdivided into type Ia and Ib on the basis of the different agglomerated forms of nitrogen.

Type Ia is characterized by aggregated nitrogen, and comprises the majority of natural diamonds. The nitrogen aggregates in diamonds are, most commonly, pairs of neighboring substitutional N-atoms, the A-aggregate and are therefore called type IaA. Another type of nitrogen aggregate in diamonds are groups of four nitrogens around a vacancy, the B-aggregate, so diamonds are referred to as type IaB. Each of these aggregate types is recognized by their infrared (IR) absorption spectra.

In Type Ib the nitrogen is present as single substitutional nitrogen atoms that has an infrared local mode of vibration at 1344 cm^{-1}, and show electron paramagnetic resonance because of the unpaired electron of the N-atom. Almost all synthetic diamond belongs to this category, because such diamonds are made at conditions (temperature and time) that do not give the opportunity for nitrogen atoms to migrate into clusters as in the natural type Ia diamonds. Nitrogen can, however, be suppressed during in growth, which case the synthetic diamonds become type II, to be discussed below.

2) Type II:

Type II diamonds contain nitrogen to less than 1 ppm and only ~1% of all naturally occurring diamonds belong to this class. Such diamonds are exceptionally "clear" because the absorption of light in the visible range due to nitrogen is absent; For that reason type II diamonds cost much more than do the common type I.

Custers [35] proposed in 1952 and 1959 that type II diamonds should be subdivided into type IIa and IIb due to the differences in luminescence and photoconductivity. Non-semiconducting is classified as type IIa, while semiconducting diamond is classified as type IIb.

The semiconducting type IIb diamonds constitute a very small proportion of type II, possibly about one in a thousand and thus very rare. Unlike other diamonds, they are semiconducting due to the presence of the acceptor boron and the absence of the donor nitrogen. Boron containing diamonds are bluish and have great commercial value due to their rarity and beauty.

Type IIa diamonds are the purest form of diamonds and contain no appreciable nitrogen, nor boron. They have no indication of colour so considered by some gemologists to be the "best" diamonds, a view that will be altered by the commercial interest in coloured diamonds.

CHAPTER FIVE
EXPERIMENTAL RESULTS AND DISCUSSIONS

In this chapter are presented the results of the experiments performed at the Positron laboratory of the Physics Department of the University of Winnipeg. In part 1 the basic positron experiments on diamond are presented and discussed. In part 2 a theoretical model for positron trapping by negatively charged vacancies is presented, and then used in connection with the illumination-induced effects on positron annihilation (part 3). The works presented in each of these sections form the basis for 3 papers submitted to journals.

5.1. Positron Annihilation Investigation of Vacancies in As-grown and Electron Irradiated Diamonds.

5.1.1. Introduction:

Characterization of defects in diamond has mainly been done by optical and hyperfine interaction methods (such as electron paramagnetic resonance (EPR)). These techniques have each identified many defects [36-38] but only in a few cases have correlation been possible: Examples thereof are substitutional nitrogen (N_S), the irradiation-produced negatively charged isolated monovacancy (V^-) and the negatively charged nitrogen vacancy complex ($N_S \cdot V^-$). It is noteworthy that optical measurements, and not EPR, have provided the main basis for models of many of the defect structures in diamond, opposite to the case of silicon.

In this work we have employed positron annihilation, together with optical measurements, to investigate vacancies, but since positron annihilation is " new " in the context of diamond research there is in this work a strong element of comparison with optical data.

In diamond the omnipresent nitrogen impurity enjoys a central role. It is the basis for the rough classification of diamonds, as Ia, Ib, IIa and IIb (see chapter 4.4.2). In Ia nitrogen is agglomerated as $N_S \cdot N_S$ (denoted the A center in optical measurements and in the following we include parenthetically the nomenclature adopted from these) or as $3N_S \cdot V$ (N3 center) or as $4N_S \cdot V$ (B center), and in any given Ia diamond a mixture is usually present. Type Ib contains only N_S-commonly found in synthetic diamonds, but very rarely in natural ones. In IIa the nitrogen content is below detection limit ($\cong$ 1 ppm) and in IIb this is also the case but there is a significant boron content which makes the diamond p-type " semi-conducting ". The nitrogen content varies greatly, from less than 1 ppm (IIa, IIb) to several hundred ppm (Ia, Ib) and the distribution is far from being homogeneous. In addition to these point-like defects there are twins, dislocations, inclusions and, as we shall see, vacancy clusters. Diamonds are highly " individual ", which frustrates systematic investigations.

Nitrogen introduces allowed electronic states in the band gap (5.5 eV). Substitutional N, N_S, has a donor level ~1.9 eV below the conduction band [39], $N_S \cdot N_S$ (A center) has a much deeper donor level at $\cong$ 4.0 eV [40], while $4N_S \cdot V$ (B center) has no known level; clearly, nitrogen plays an important role in establishing the Fermi level and is, additionally, a trap for vacancies. Zero-phonon lines have identified several such vacancy-associated complexes ($N_S \cdot V, N_S \cdot N_S \cdot V$ (H_2 or H_3), $3N_S \cdot V$ (N3), and $4N_S \cdot V$-V (H4)).

The isolated monovacancy is produced by irradiation and is immobile to fairly high temperature (~550 ^0C). In its neutral state it gives rise to the GR absorption system

(prominent zero-phonon line at 741 nm, GR1) and in its negative state (EPR active) to the ND1 system (zero-phonon line at 394 nm). The 0/- level is inferred to be close to the mid-gap position [41]. Divacancies have tentatively been associated with the series of zero-phonon lines (TH5) in the 440-540nm range (in IIa) [42] and while larger agglomerates have not been identified by optical means, they have been indicated by means of EPR.

As mentioned above, positron annihilation is relatively new in the context of diamond research, with most of the papers dating from 1990. Several investigations have been done on diamond films [43-49], all of which showed substantial vacancy concentrations and formation of positronium. Studies on single crystalline diamonds [50-55] have been somewhat frustrated by difficulties in establishing the bulk lifetime for positrons, an issue that will be addressed in this work. On the theoretical front [56-59] bulk positron lifetimes and momentum distributions have been calculated, as have been the positron lifetimes for mono- and di-vacancies [56]. Vacancy production arising from irradiation has been reported in [60-64].

In this work we report on positron lifetime and Doppler broadening experiments on a variety of diamond types, unirradiated as well as electron irradiated. We also report on measurements at elevated temperatures (up to 770 K), where optical measurements are not possible, and on isochronal annealing. The positron-based results, while confirming several key interpretations based on optical measurements, reveal new effects in particular at elevated temperatures, and details pertaining to the formation of $N_S \cdot V^-$ complexes in Ib diamond.

5.1.2. Experimental:

a: Samples and Irradiations.

Twenty-four diamond samples were investigated making up 12 sets for positron measurements. The samples were characterized by optical absorption in the infrared at room temperature and in the " visible " (250 to 1200 nm) at 85 K so to detect zero-phonon lines. The infrared absorption arising from substitutional nitrogen N_S, $N_S \cdot N_S$ (A center) and $4N_S$ -V (B center) together with their concentration calibrations [65,66] form the basis for concentration estimates with results as listed in Table I.

Table 1. Concentrations of substitutional nitrogen (N_S), $N_S \cdot N_S$ (A centers) and $4N_S \cdot V$ (B centers). In the Ia(2) diamonds there were also $3N_S$ -V (N3) centers and platelets but their nitrogen concentration cannot be determined. The purely Ib type is synthetic, while the rest are natural diamonds. Entries of zero mean below detection limit ($\approx$1 ppm). 1 ppm corresponds to an absolute concentration of $1.76\times10^{17}/cm^3$.

Type	[N_S] (ppm)	[A] (ppm)	[B] (ppm)
Ia(1)	0	37	13
Ia(2)	0	175	350
Ib(syn)	45~210*	0	0
Ib(nat)	67	11	0
IIa(1)	0	0	0
IIb(2)	0	0	0
IIb	0	0	0

*) range for different samples.

Not included in these is nitrogen in " platelets " and in $3N_S \cdot V$ (N3) which both occur particularly in Ia and possibly also in the natural form of Ib, listed as Ib(nat) in Table I; these omissions are due to the lack of calibration. Synthetic Ib diamonds (from Sumitomo Co., Japan) are listed as Ib(syn). In all of the Ib(syn) diamonds there were macroscopic variations in the nitrogen concentration as evidenced by different shades of yellow colour, so both optical and positron measurements were done on an area of uniform colour to the eye, but in view of these macroscopic variations, microscopic variations are also very likely within the volume sampled by the positrons ($\approx 0.1\ mm^3$).

IIa(1) was cleaved to expose the [111] surface while the Ib(syn) and Ia(1) diamonds were cut to expose the [100] surface. This difference does not matter to positron lifetime measurements but does, potentially, to Doppler broadening (see chapter three, section 3.6).

Electron irradiations were done on Ia(1) at 3.5 MeV while for IIa(1), Ib (syn, N_S=130ppm) and Ib(nat) the energy was 2.3 MeV. The beam was pulsed (duty cycle of 240 pulses/s each of duration 3 ms). The dose rate for 2.3 MeV was $10^{17}\ cm^{-2}h^{-1}$ while for 3.5 MeV it was 7 times higher; the samples were cooled directly by water at $8\ ^0C$. The Ia(1) sample had been previously irradiated at 3.5 MeV to a dose of $2.1\times10^{18} e^- / cm^2$ at a dose rate of $10^{17}\ cm^{-2}h^{-1}$, and then annealed up to 1020 ^0C . We mention that for the high dose rate the colour of the diamonds turned green, whereas for the original lower dose rate they were blue; this may have gemological interest [67] but the physical reason for the difference is not clear.

Annealing of the irradiated samples took place under a flow of Ar in a quartz tube. Above $700\,^{0}C$ Ti flakes were added close to the samples to get oxygen to prevent graphitization of the diamond surfaces [49].

b: Measurements

Infrared absorption was measured on samples at 300 K using a Fourier-transform spectrometer (4 cm^{-1} resolution), while a single beam spectrometer was used in the 200-1200 nm range with samples at 85 K.

Positron lifetime measurements were made with two lifetime spectrometers, one for room temperature, the other for low temperatures. The former had a prompt width of 170-175 ps, the latter 205-210 ps, but the latter was more efficient so to compensate for the larger detector distance necessitated by the cryostat. Each measurement lasted 11 h (and was repeated twice) during which time $(8-10)\times10^{6}$ counts were accumulated. The positron source had a strength of 14-18 μCi, and gave rise to a source correction of 250 ps with an intensity of 1.5% which arises from the Al source-backing foil. The high number of counts was found necessary in order to resolve the rather short lifetimes using the RESOLUTION program [30].

Doppler broadening experiments were done with an intrinsic Ge detector having an energy resolution of 1.2 keV at the 511 keV annihilation γ quanta. Each spectrum contained 2×10^{6} counts in the 511 keV peak and was repeated 4-5 times during a time span of 20 h; the analyses of these spectra are described in the chapter two.

5.1.3. Results

a: Unirradiated Diamonds.

Lifetime and Doppler results are listed in Tables 2 and 3, and in Figs.5.1 and 5.2. As seen in Table 2, up to three lifetimes, τ_i, with intensities, I_i, could be resolved. If the shortest lifetime component has been properly resolved and trapping is occurring from the bulk into defects, then this lifetime is the modified bulk lifetime, $\tau_1 = 1/(\lambda_B + \kappa)$. The longer lifetimes τ_2 and τ_3 are associated with open volume defects of different sizes. Two auxiliary parameters can be calculated from the experimental data, namely the composite (average) lifetime

$$\tau_{avg} = \sum_{i=1}^{N} \tau_i I_i , \qquad (5.1)$$

and the parameter

$$\tau_B^{TM} = \left\{ \sum_{i=1}^{N} I_i / \tau_i \right\}^{-1} , \qquad (5.2)$$

where N is the number of components that can be resolved (2 or 3). The latter parameter is of particular importance because if the annihilation scheme follows the trapping model (TM), which assumes that all positrons are initially in the bulk state, then τ_B^{TM} will equal the bulk lifetime $\tau_B (= 1/\lambda_B)$. In trap-free diamond this value has been determined experimentally to be 97 ± 1 ps [51]. The values of τ_B^{TM} calculated here are generally larger than 97 ps, and significantly so for the Ia samples. All of the samples yield a weak component, τ_3, whose values of 170-420 ps indicate vacancy clusters of varying size; such have also been observed in other works [52,54,63]. It is clear from the results listed in Table 2 that the vacancy content varies greatly even within the same type of diamonds.

Table 2. Lifetime results for unirradiated diamonds measured at room temperature. Lifetimes and their associated intensities are listed together with the auxillary parameters τ_{avg} and τ_B^{TM} as defined by Eqs. (5.1) and (5.2).

	τ_1 (ps)	τ_2 (ps)	τ_3 (ps)	I_1 (%)	I_2 (%)	I_3 (%)	τ_{ave} (ps)	τ_B^{TM} (ps)
Ia(1)	112±5	180±2	400±2	88±1	8±1	4±1	130±1	119±5
Ia(2)	106±6	162±7	424±3	46±8	51±8	3±1	144±0.5	130±6
Ib(syn)*	97~101	--	170-	92~81	--	7~19	107~114	104~1
Ib(nat)	58±4	148±1	326±9	37±2	56±2	8±1	130±1	96±6
IIa(1)	100±1	--	374±4	93±1	--	7±1	119±0.5	105±3
IIa(2)	71±3	139±4	393±9	43±4	48±4	9±1	134±1	103±6
IIb	97±1	--	200±5	91±1	--	9±1	116±0.5	102±1

*) See Fig.5.1 for details of the dependencies of lifetime parameters on N_S concentration.

Table 3. S and W parameters for unirradiated diamonds at room temperature. For easy reference, S and W parameters for undoped float-zone Si are 0.5095 and 0.0082, respectively, using the same energy regions as for diamond (see Fig.2.5).

	S (±0.0005)	W (±0.0005)	τ_{ave} * (ps)
Ia(2)	0.3913	0.0215	144±0.5
Ib(syn)**	0.3847~0.3876	0.190~0.215	107~114
Ib(nat)	0.4010	0.0194	130±1
IIa(1)	0.3850	0.0170	119±0.5
IIa(2)	0.3971	0.0163	134±1
IIb	0.3884	0.0184	116±0.5

*) From Table 2.

**) See Fig.5.2 for dependencies of S, W on N_S concentration.

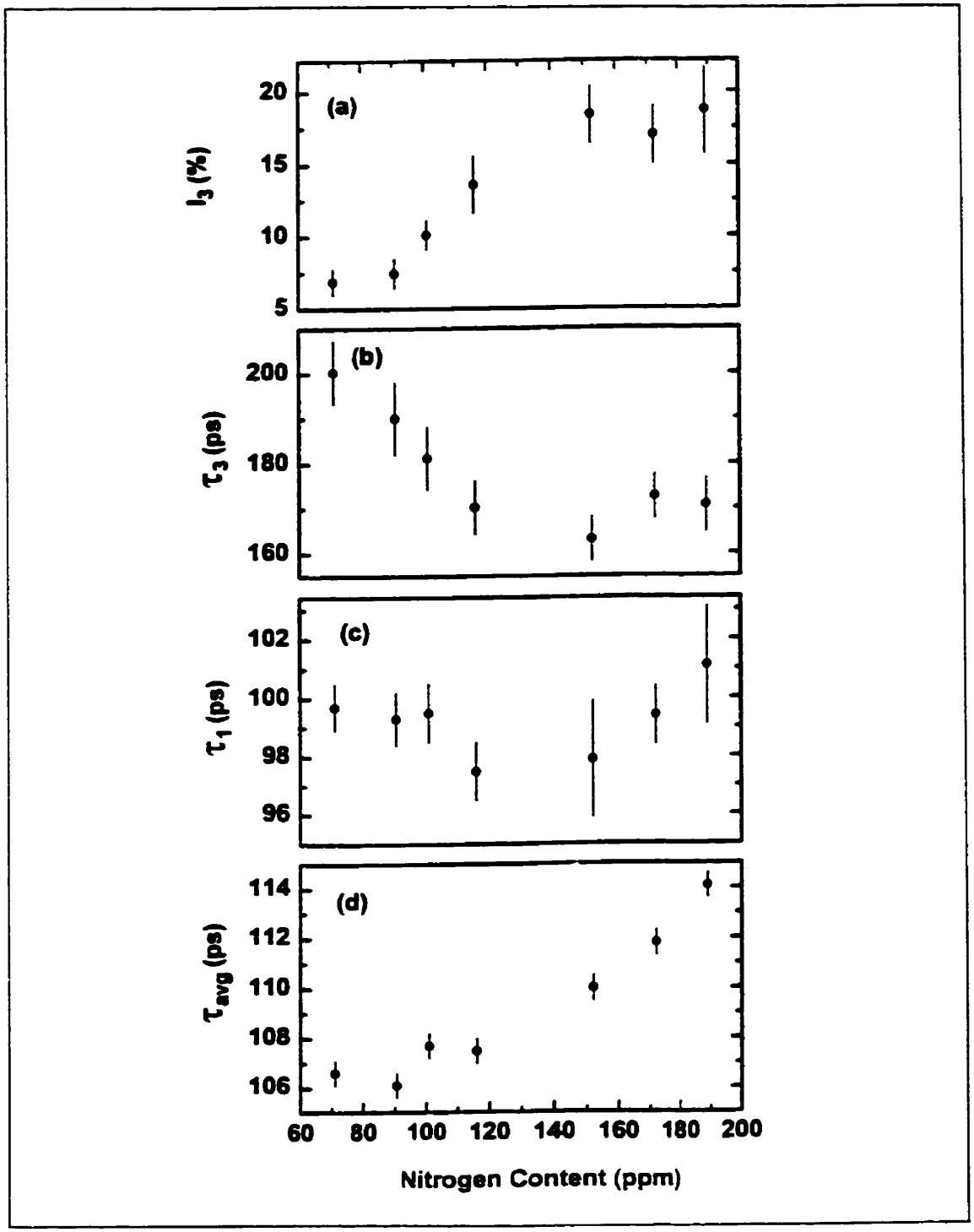

Figure 5.1. Lifetime parameters at room temperature for the Ib(syn) samples as a function of nitrogen content.

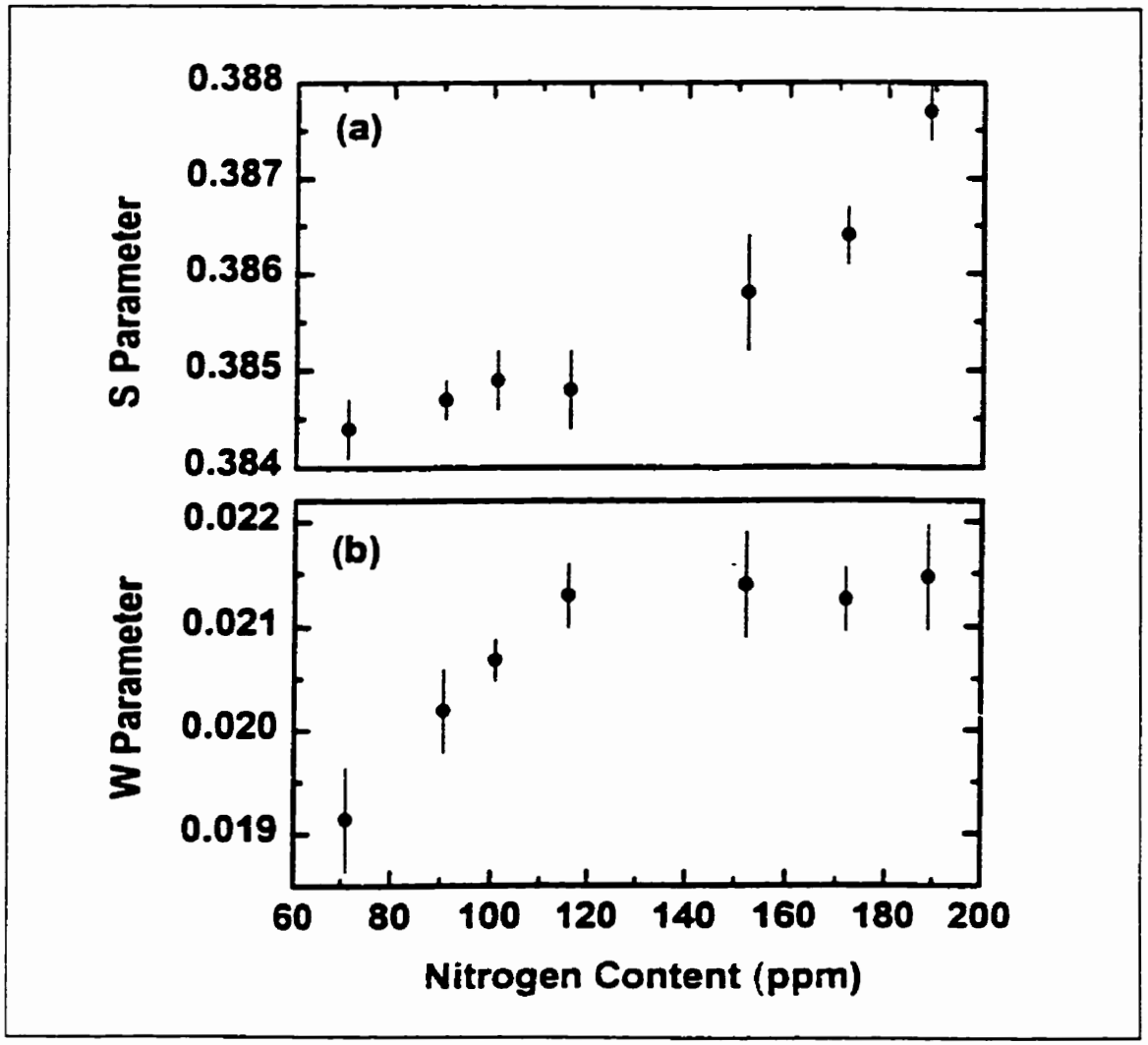

Figure 5.2. S and W parameters at room temperature for the Ib(syn) samples investigated by lifetime spectroscopy (Fig.5.1).

The Ib(syn) diamonds contained various concentrations of N_S so a study could be done as a function of concentration as averaged over the two samples used to make up the source-samples assembly (see Fig.5.1). There seems to be a systematic trend towards higher vacancy concentration with N_S concentration as indicated by the increasing value

of I_3, but we do mention that a sample set with N_S=130 ppm gave a result (290 ps with 5% intensity) which does not follow the trend. This particular sample set was obtained from the same supplier, but much earlier than the others shown in Fig. 5.1, and may therefore have been manufactured somewhat differently. A larger ensemble of similarly manufactured samples is necessary to firmly establish if a systematic trend with N_S concentration indeed exists. Figure 5.2, displaying Doppler data, indicates systematic trends with N_S concentration where S has the same trend as τ_{avg} in Fig.5.1(d). W does not exhibit the expected opposite behavior to S.

At-temperature measurements were also done between 30 K and 770 K on Ia(1), Ib(nat), Ib(syn, Ns=130 ppm) and IIa(1) but no significant temperature effects were found.

The anisotropy of S was investigated to determine if the numerical difference in the values between the [100] direction (cut diamonds) and the [111] direction (cleaved) had any importance when comparing data. The difference amounts to $0.5 \pm 0.2\%$ agreeing within experimental uncertainty with Nilen et al.'s [53] more detailed investigations, so the effect from anisotropy is small enough not to matter here.

b: Irradiated Diamonds.

IIa(1) and Ib(syn, Ns=130 ppm) were investigated as a function of dose administered simultaneously to the samples. These two types were chosen because in IIa neutral monovacancies are formed according to the interpretation of optical results, while in Ib(syn) they are negatively charged [37]. To positrons this charge difference matters very much as explained in the section 3.6, thus providing a method of establishing

charge completely independently of optical measurements. For IIa(1), Fig.5.3 shows lifetime data and Fig.5.4 Doppler data. Irradiation produces a new lifetime, denoted τ_2, with a value (145 ± 5 ps), which is larger than τ_B ($\cong 100$ ps), so this lifetime must arise from vacancies. The intensity, I_2, of this lifetime component increases with dose but does not depend on temperature in the 30 to 300 K range for any of the doses employed.

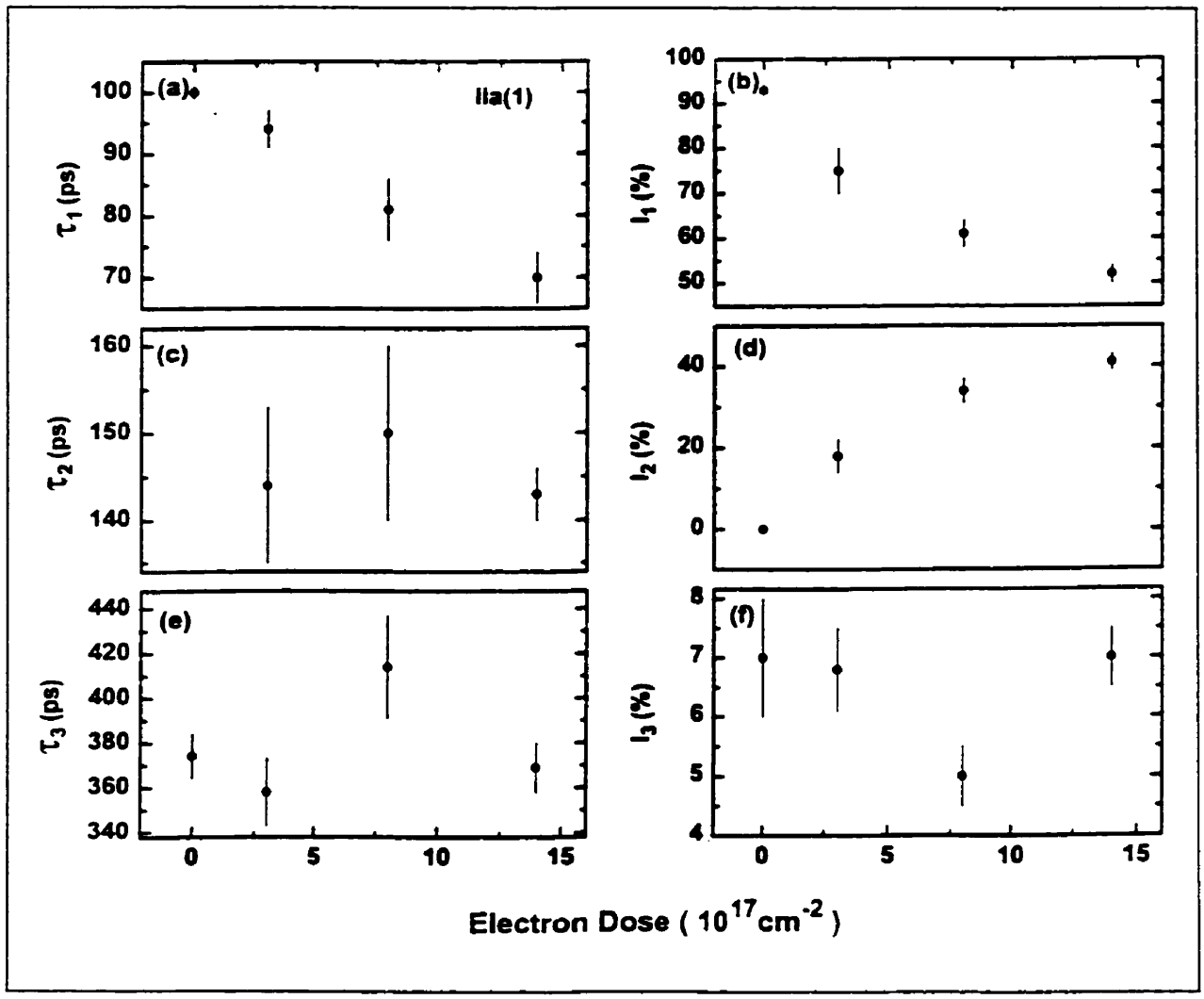

Figure 5.3. Lifetime results for the IIa(1) samples at room temperature as a function of the dose from 2.3 MeV electrons.

so the vacancies are neutral. Optical measurements showed GR1 absorption interpreted to arise from neutral monovacancies and we will later demonstrate a very good correlation with the positron response, allowing for the conclusion that the 145 ps lifetime in IIa diamonds arises from neutral monovacancies.

Doppler results are customarily presented as the ratios S/S_B and W/W_B, i.e., relative to the shape parameters for the defect-free bulk material. This is done since S and W are strongly dependent on the choice of energy range while these ratios are much less so, thus facilitating comparisons with other works. As will be described in the discussion section we have no basis for obtaining W_B, but can estimate S_B. This estimated value is labeled S_{Ref} to avoid giving the impression that an accurate bulk value has been determined. The Doppler data, S/S_{Ref}, in Fig.5.4 show an increase with dose, which is expected in view of the lifetime data.

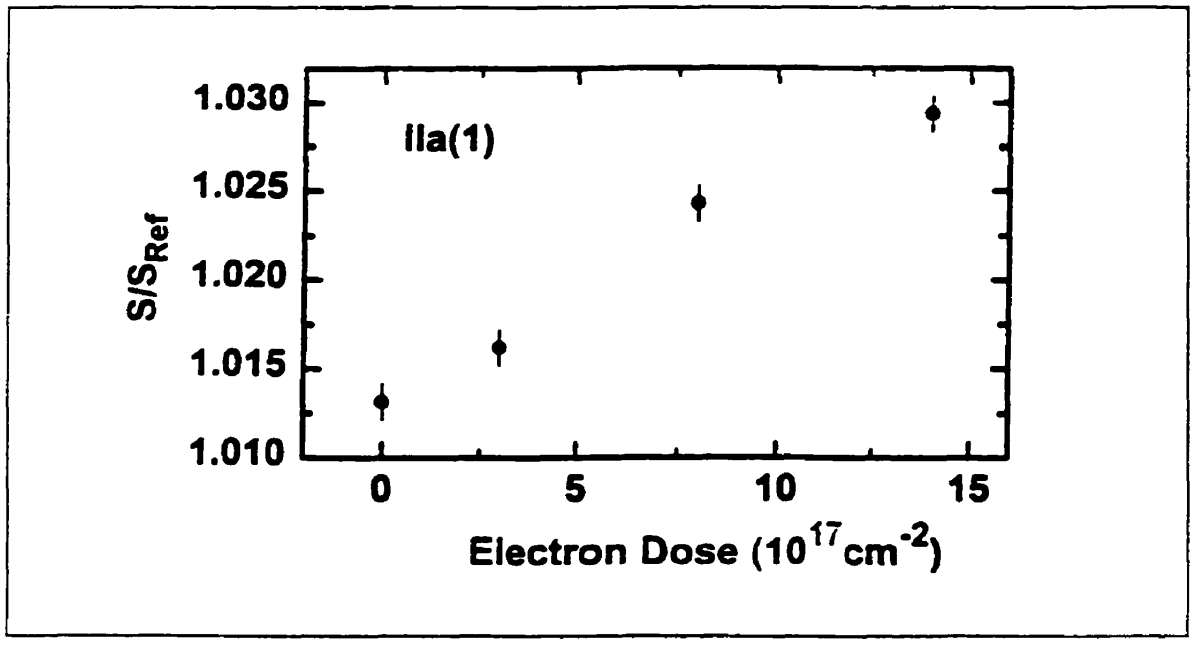

Figure 5.4. Relative changes in S at room temperature for the IIa(1) samples for which lifetime data are shown in Fig.5.3. S_{Ref}=0.3800.

Table 4. Lifetime and Doppler data for Ib(syn, Ns = 130 ppm) for accumulated electron doses. Results are for measurements at room temperature. $S_{Ref} = 0.3800$.

Dose ($10^{17} e^- / cm^2$)	τ_1 (ps)	τ_2 (ps)	τ_3 (ps)	I_1 (%)	I_2 (%)	I_3 (%)	S / S_{Ref} (± 0.002)
0	105 ± 2	--	290 ± 10	95 ± 1	--	5.0 ± 0.5	1.013
3	--	140 ± 1	315 ± 20	--	92.2 ± 0.7	7.8 ± 0.7	1.073
8	--	145 ± 1	347 ± 15	--	93.0 ± 0.6	7.0 ± 0.6	1.080
14	--	144 ± 1	320 ± 11	--	92.5 ± 0.6	7.5 ± 0.6	1.079

Results for Ib(syn) are listed in Table 4. Already at the dose of $3\times10^{17} e^- / cm^2$ the results differ significantly from those of IIa(1); no τ_1 could be resolved, indicating a trapping rate of at least 15 ns^{-1}, and S / S_{Ref} is much larger, but the irradiation-produced lifetime, τ_2, is the same (140-145 ps) as for IIa(1). This indicates that monovacancies in Ib(syn) are much more efficient in trapping positrons than in IIa(1). Our optical measurements showed no absorption due to neutral vacancies (GR1) but based on the lifetime value the vacancies would be monovacancies, and according to independent optical measurements they should be negatively charged, i.e. give rise to the ND1 absorption system at 394 nm (zero phonon line). In our case that absorption could not be detected due to the strong absorption by N_S, thus defying direct correlation. However, in view of positron and optical data, there is very little doubt that in Ib(syn) the monovacancy is negatively charged.

In the case of Ib(nat) only two fairly low doses were administered. Already after the lowest dose (see Table 5) it was not possible to resolve τ_1 indicating that in this natural Ib-type diamond the monovacancies are also negatively charged. The τ_2 lifetime is about 133 ps after irradiation, 10 ps smaller than for Ib(syn), but this can very well be a computational artifact due to the significant contribution from vacancies in the pre-irradiated samples. Optical measurements showed no response from neutral monovacancies, but, as was the case for Ib(syn), the strong absorption due to N_S prevented observation of absorption bands below $\cong 400$ nm.

Table 5. Lifetime data for Ib(nat) at room temperature for accumulated electron doses.

Dose ($10^{17} e^- / cm^2$)	τ_1 (ps)	τ_2 (ps)	τ_3 (ps)	I_1 (%)	I_2 (%)	I_3 (%)
0	58 ± 4	148 ± 1	326 ± 9	37 ± 2	56 ± 2	8.2 ± 0.5
1	--	133 ± 2	321 ± 14	--	87 ± 1	13 ± 1
3	--	134 ± 3	291 ± 10	--	90 ± 1	10 ± 1

The Ia(1) samples were previously investigated [60], and where irradiated using 3.5 MeV electrons to a dose of $25\times10^{17} / cm^2$. They were then annealed to 1020 ^0C which removed most of the irradiation damage [49]. These samples were then re-irradiated to the same dose but with a dose rate 7 times higher than previously used. The lifetime data in Table 6 for the originally irradiated and the re-irradiated samples indicate a slightly larger contribution (I_2) from monovacancies in the latter case and the value for

τ_2 is smaller. This lower value is more in line with the values found in the other diamond samples.

Table 6. Results obtained for Ia(1). First row, before irradiation; second row, after irradiation with 3.5 MeV electrons to a dose of $21\times10^{17}e^-/cm^2$ at $1\times10^{17}e^-/cm^2/h$; third row, after annealing to 1020^0C; fourth row, for re-irradiation to nearly the same dose as before but with a 7 times higher dose rate.

Dose ($10^{17}e^-/cm^2$)	τ_1 (ps)	τ_2 (ps)	τ_3 (ps)	I_1 (%)	I_2 (%)	I_3 (%)
0	112±5	180±20	400±20	88±1	8±1	4±1
21	88±4	155±5	390±30	43±2	55±5	2±2
+annealing At 1020 ^0C	110±5	180±15	380±20	67±3	20±4	3±1
25 (re-irradiated)	85±7	135±5	315±17	25±5	70±5	5±2

c: Temperature Effects for Irradiated Diamonds.

Low temperature lifetime measurements (30-300 K) were done on Ia(1), Ib(nat), Ib(syn, Ns=130 ppm), and IIa(1). In none of these samples did the lifetime measurements reveal any clear changes with temperature, as exemplified by the data shown in Table 7 for Ib(syn). Doppler measurements were done over a wider temperature range (30-770 K) with results as shown in Fig.5.5. The ability to conduct positron measurements at elvated temperatures sets the positron annihilation technique apart from optical techniques which require low temperatures for resolving absorption bands. The Doppler data shown in Fig.5.5 are reversible except for the case of Ib(syn). Up to 730 K they were reversible,

but at 770 K a non-reversible decrease took place during the 24 hours of measurement time; the irreversible decrease in S/S_{Ref} was from 1.079 to 1.072, and suggests some removal of V^-.

Table 7. Lifetime and Doppler data as a function of temperature for Ib(syn, Ns=130 ppm) irradiated to a dose of $14\times10^{17} e^-/cm^2$. S_{Ref}=0.380.

T (K)	τ_2 (ps)	τ_3 (ps)	I_2 (%)	I_3 (%)	S/S_{Ref} * (±0.002)
50	140±2	343±17	93.0±0.6	7.0±0.6	1.066
100	141±2	355±16	93.4	6.6	1.067
150	142±1	359±15	93.6	6.4	1.068
200	142±2	336±20	92.6	7.4	1.071
250	144±1	356±17	93.3	6.7	1.074
293	144±1	320±11	92.5	7.5	1.078

*) These data are also shown in Fig.5.5.

The most important features of the data in Fig.5.5 are the following: i) S/S_{Ref} for Ib(syn) increases with temperature between 30 and 300 K; ii) S/S_{Ref} for Ib(nat) and Ia(1) increases at elevated temperatures (above 400 K and 500 K respectively) and iii) for IIa(1) there is little temperature dependency. We will explain the behaviors noted in ii) in terms of Fermi level effects shifting the balance from neutral to negatively charged monovacancies.

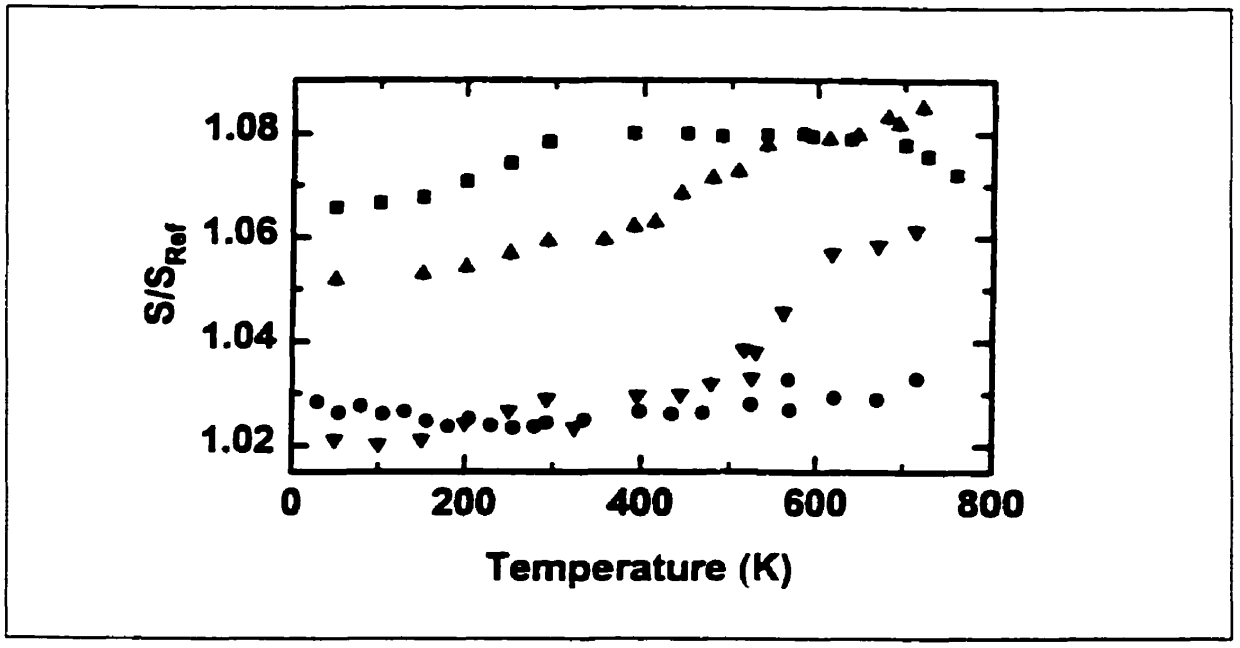

Figure 5.5. Relative changes in S for irradiated diamonds as a function of sample temperature. ■: Ib(syn, Ns = 130 ppm), dose $14\times10^{17}e^{-}/cm^{2}$. ▲: Ib(nat), dose $3\times10^{17}e^{-}/cm^{2}$. ●: IIa(1), dose $14\times10^{17}e^{-}/cm^{2}$. ▼: Ia(1), dose $25\times10^{17}e^{-}/cm^{2}$. For sample identifications see Table 1.

d: Annealing Studies of Irradiated Diamonds.

One of the sample-sets investigated at elevated temperatures was subsequently subjected to isochronal annealing up to 1170 ^{0}C; Ib(syn, N_S=130 ppm) was chosen because of its low content of vacancy cluster, allowing investigation of V^{-} and its complexing with N_S. Doppler data for Ib(syn) are shown in Fig.5.6 and lifetime data in Fig. 5.7. For all of the lifetime spectra it was impossible to resolve the short-lived τ_1 component arising from positrons annihilating in the bulk state indicating that the trapping rate was large ($\geq 15ns^{-1}$). The decrease in S/S_{Ref} between $20^{0}C$ and the first annealing temperature in Fig.5.6 is due to the removal suffered during the preceding at-temperature experiments up to $480^{0}C$.

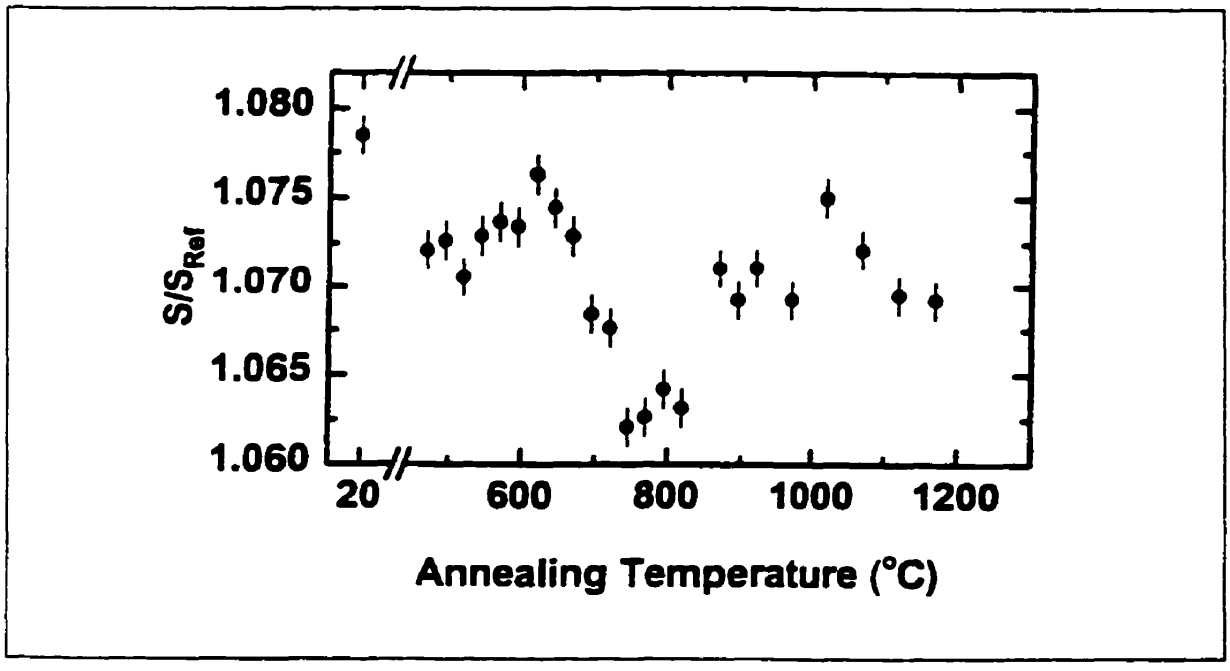

Figure 5.6. Relative S parameter as a function of annealing temperature for Ib (syn, Ns = 130 ppm) irradiated to a dose of $14\times10^{17}e^{-}/cm^{2}$. The entry at $20^{0}C$ is for the as-irradiated case and the one at $480^{0}C$ corresponds to the highest temperature in the at-temperature measurements shown in Fig. 5.5.

The most important features of the data in Fig.5.6 are the "dip" of S/S_{Ref} centered close to $800^{0}C$, and the strong correlation between S/S_{Ref} and τ_2 in Fig.5.7.

Optical measurements were also done on the Ib(syn) sample, but unfortunately only for annealing temperatures $\geq 720^{0}C$. Fig.5.8(a) shows absorption in the visible range where the zero-phonon line at 637 nm – plus replica – is due to the negatively charged $N_S \cdot V$ complex [36]. Apart from the absorption peak at ~ 470 nm, not present in the as-irradiated state of the samples, and which disappeared slowly until ~ $900^{0}C$, there were no other absorption peaks generated up to $1170^{0}C$; the 470 nm absorption

line has variously been interpreted as arising from divacancies [69] or from interstitial clusters [70].

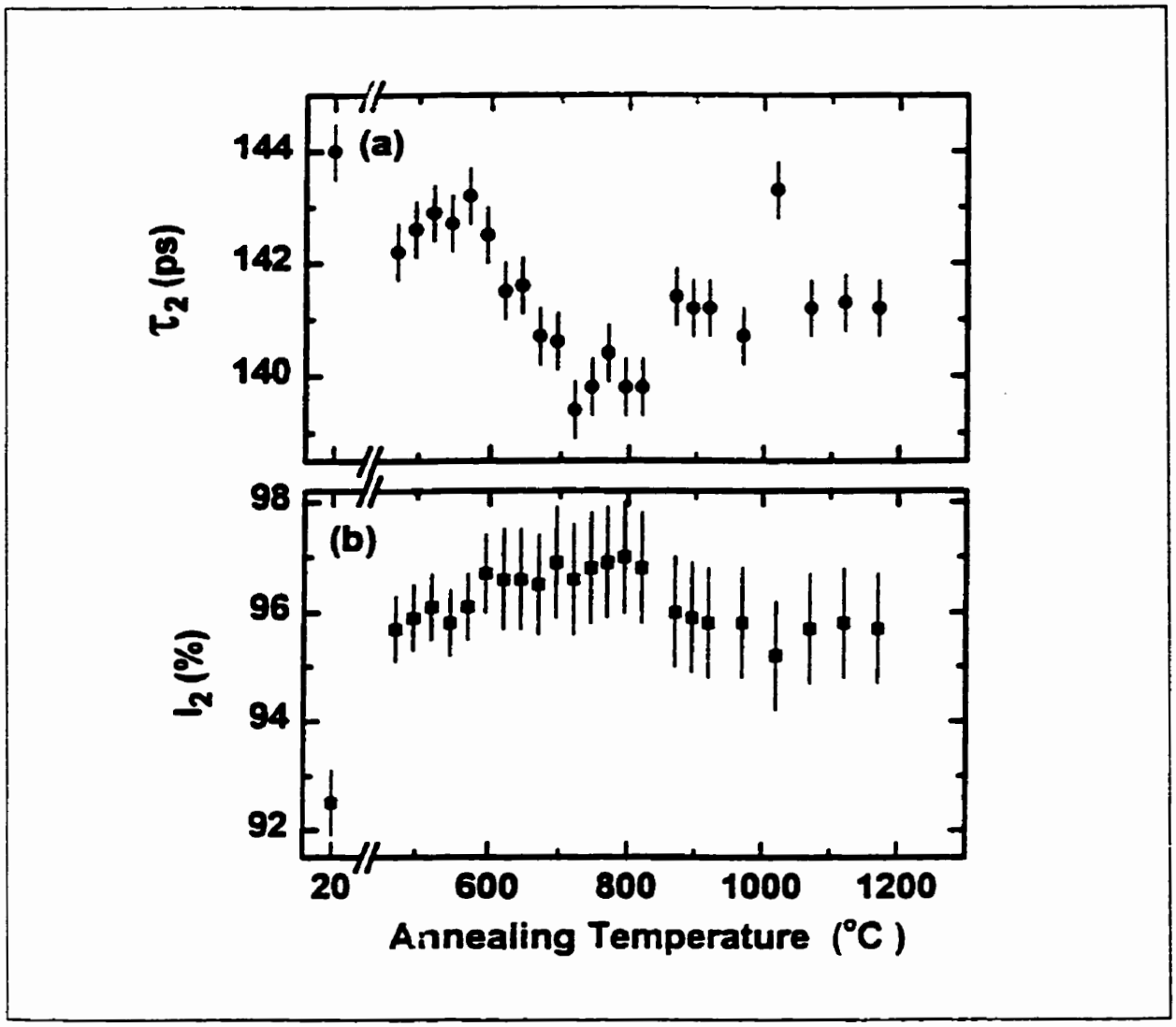

Figure 5.7. Lifetime data for the samples whose relative S parameters are shown in Fig.5.6. No τ_1 component could be resolved. In addition to τ_2 there was a τ_3 component ($\equiv 300$ ps) with an intensity of $(100 - I_2)$.

To obtain a quantitative measure for $N_S \cdot V^-$ absorption, we have plotted in Fig.5.9 the integrated absorption coefficient of the zero-phonon line at 637 nm as a function of

annealing temperature. The decrease in $N_S \cdot V^-$ absorption between 820 and $870\,^0C$ amounts to a decrease in concentration of ≅ 15%.

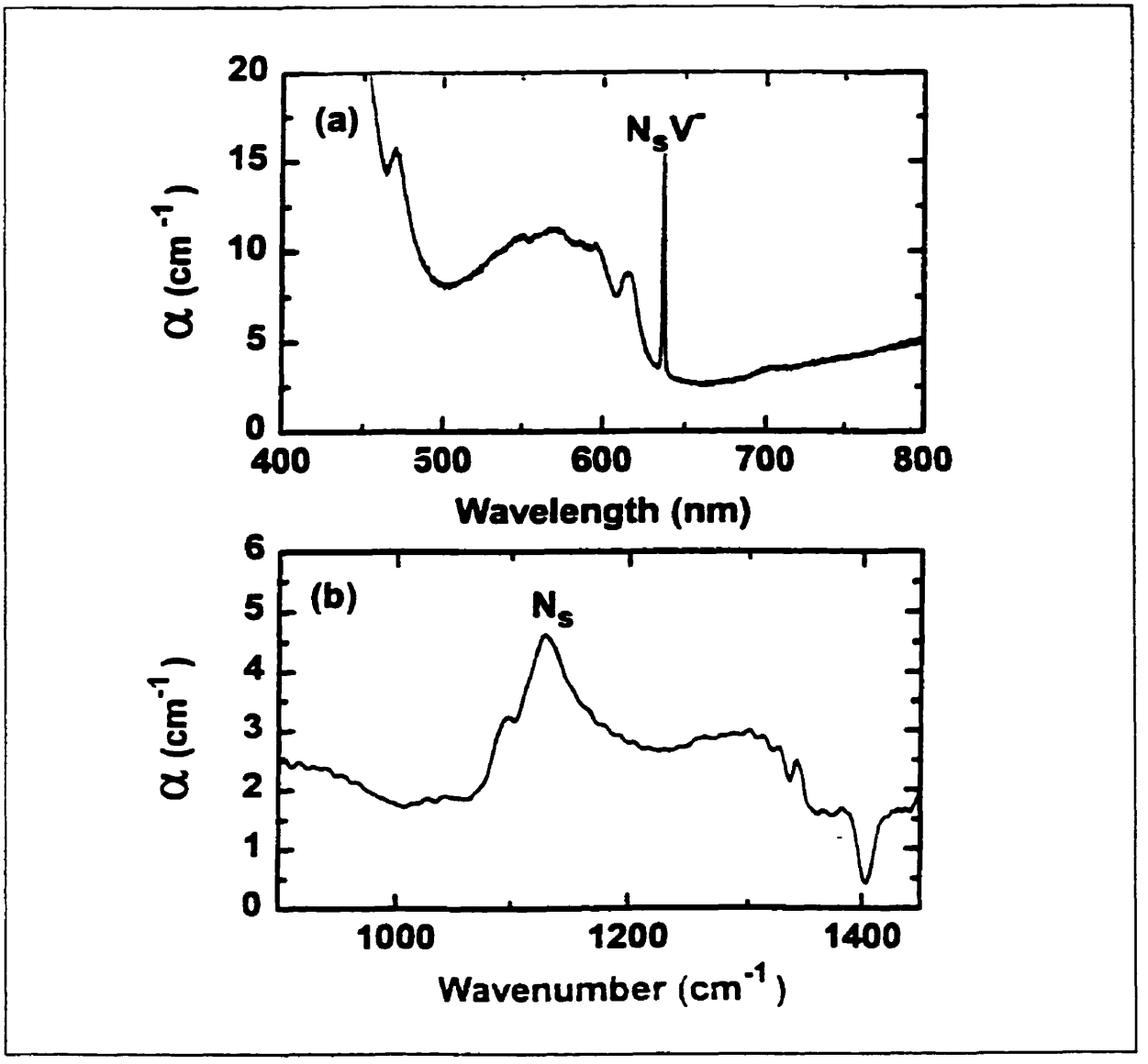

Figure 5.8. Optical absorption coefficient of Ib (syn, Ns = 130 ppm) irradiated to a dose of $14\times10^{17} e^- / cm^2$ and then annealed to $720\,^0C$: (a) for the visible range and (b) for the infrared range, the latter showing the presence of N_S.

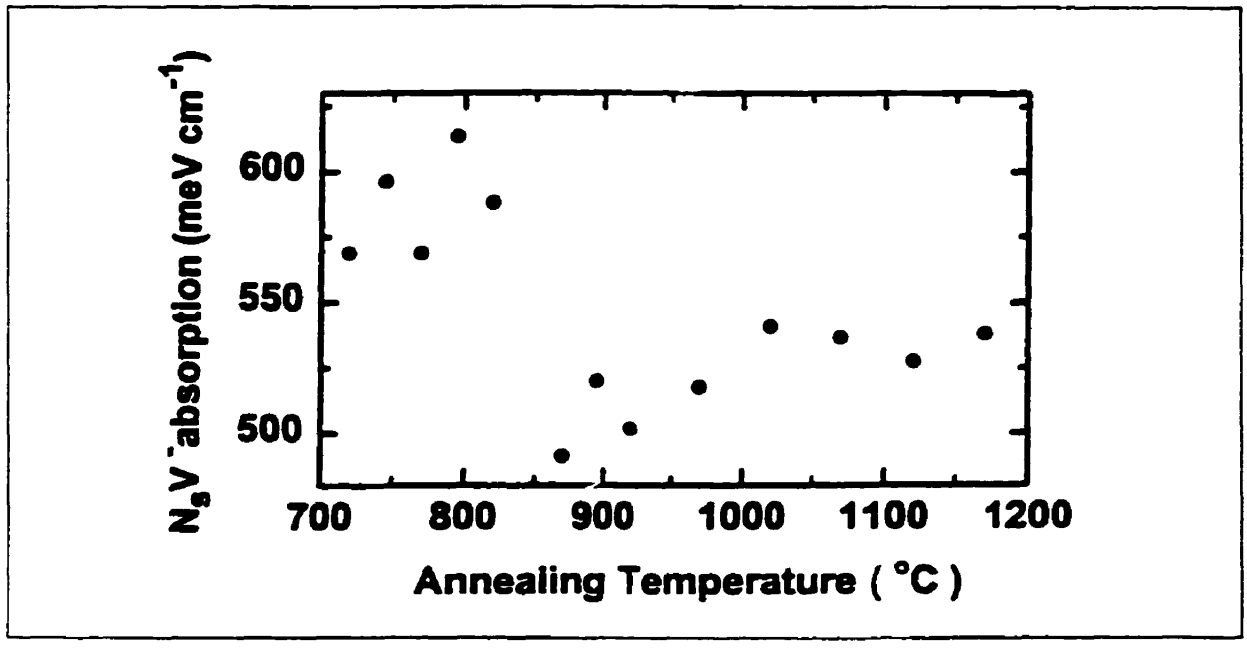

Figure 5.9. Integrated absorption of the N_SV^- zero-phonon line (see Fig.5.8(a)) as a function of annealing temperature.

This concludes the presentation of the results. We can summarize them as follows: i) Natural as well as synthetic diamonds contain vacancy clusters as signaled by the τ_3 component. ii) Electron-irradiation-induced monovacancies affect the positrons very differently according to the type of diamonds, being much stronger in type Ib than in type IIa. iii) Strong temperature effects at elevated temperatures are observed in irradiated Ia(1) and the Ib(nat) whereas none are observed in IIa(1).

5.1.4. Discussion

a: Unirradiated Diamonds.

One of the most important positron parameters is the bulk lifetime since all other lifetimes are gauged relative to it. In the case of diamond, experiments have yielded

values between 97 ps [51] and 120 ps [50] and theory, values between 93 ps [71] and 114 ps [56]. The 97 ps lifetime was determined using a synthetic IIa diamond for which the lifetime spectrum contained only one resolvable component in which case the 97 ps lifetime reasonably can be interpreted to be the bulk lifetime, but there is the concern that catalysts used to produce the synthetic diamond could influence the observed lifetime. Uedono et al. [63] found a dominant lifetime of 99 ps in synthetic IIa diamond but larger values)up to 106 ps) were found in other types of diamonds. The significantly higher value of 120 ps [50] for the bulk lifetime was based on natural Ia diamonds and this turns out, in retrospect, to be a poor choice as will be discussed below.

None of the diamonds investigated in this work were free of vacancy contributions (τ_2, τ_3, see Table 2, p65). To calculate the bulk lifetime, the simple trapping model (Eq.5.2) can be used to obtain τ_B^{TM} as listed in the last column of Table 2. Except for Ia diamonds this procedure yields values close to, but slightly larger than, 97 ps. The problem with Ia diamonds seems to be that there are unresolved lifetime components modifying in particular the short lived τ_1 component and possibly arising from $4N_S \cdot V$ (B) centers. Dismissing the Ia diamonds as unsuitable for determining the bulk lifetime gives an estimate of 104 ± 2 ps for the rest of the diamonds which is quite close to the value of 97 ± 1 ps, and we argue that the agreement is even closer based on the following observations. The data for I_3 for the electron irradiated Ib(syn) (Table 4, p71), Ib(nat)(Table 5, p72), Ia(1) (Table 6, p73) and IIa(1) (Fig.5.3, p69) all show that this intensity is independent of dose. However, according to the trapping model, I_3 should decrease due to the increasing competition from monovacancies in trapping

positrons. We suggest, therefore, that the τ_3 component originates from positrons that are captured in local regions of high vacancy concentration during slow-down. I_3 is thus the fraction of positrons which never occupy the bulk state and should therefore be excluded when calculating the bulk lifetime from the trapping model: Doing this we obtain the value of 98 ± 2 ps for the bulk lifetime based on 11 different sets of natural and synthetic diamonds.

The fraction of positrons captured during slow-down by regions of high vacancy concentration is typically 7% but up to 20% is found in Ib(syn) containing a large N_S concentration (Fig.5.1(a)). These percentages seem high if one were to take them to represent the fractional crystal volume of the regions, but two factors may accentuate the positron response: i) The energy loss of positrons entering into the region at positron energies below the band gap (5.5 eV) would be more efficient than in the bulk due to defect-induced electronic levels within the band gap, i.e. positrons are preferentially stopped in these regions, and ii) the diffusion length of the positrons will be reduced due to trapping, i.e. positrons stay within the defected regions. Although such inhomogeneously distributed regions of high vacancy concentrations have not been detected by other means, they might well be suspected in view of the proficiency of diamond for containing inhomogeneously distributed nitrogen.

The lifetime data in Table 2 (p65) and Fig.5.1(p66) show that the content of vacancies varies significantly even for the same type of diamond. We bring attention to, in particular, Ib(nat) and IIa(2) which both have a τ_2 component whose value would suggest monovacancies (in view of the results from electron irradiation to be discussed below). These cannot, in either case, be V^0 since no GR1 absorption was observed for

either sample. However, $3N_S \cdot V$ is *possible* for Ib(nat) because absorption therefrom would not be detectable due to the strong absorption from N_S. For IIa(2) the lack of absorption bands between 250 nm and 1200 nm rules out monovacancies, free or complexed in forms that give rise to optical absorption. A possible defect candidate for the regions could be dislocation tangles which are particularly prevalent in IIa diamonds at considerable concentrations ($\approx 10^8 / cm^2$).

Based on the lifetime data for IIa(2) (Table 2, p65) the trapping rate is $4.1 \pm 0.2\ ns^{-1}$ and with Eq. (2.6) the defect-specific ratio S_V / S_{Ref} has the value of 1.10 ± 0.01. As will be discussed below, irradiation-produced monovacancies give a value of 1.079 ± 0.002 and a lifetime of 145 ps, so different defects may be indicated, even though the positron lifetimes for the two defects are nearly the same, i.e., in these disordered regions positrons may detect defects with an open volume that corresponds closely to that of free monovacancies but with a different "structure".

We now discuss the Doppler data in further detail, a main point being assessing the value of S for the bulk, S_B. This is not straightforward since all of the investigated diamonds display a vacancy component according to the lifetime measurements. To arrive at a value for S_B we select among the various samples those which have the smallest contributions from vacancies, and hence the smallest deviations from S_B. The selected samples are IIa(1), IIb, and Ib(syn) with $[N_S] \leq 100$ ppm, producing an average S value of 0.3854 ± 0.0005. We next assume that S for the vacancy clusters, S_C, is such that $S_C / S_B = 1.2$, which we judge a "reasonable" value for clusters; the data for the above selected samples then yield a value of 0.3800 ± 0.0005, and is used throughout this work.

However, as noted earlier, in view of the assumptions made, we refer to this value merely as S_{Ref}, rather than S_B.

The W parameters (expressing the core-momentum distribution) are puzzling in that W values for the nitrogen-lean diamonds (IIa(1), IIa(2) and IIb), which are nearly the same (0.017, Table 3), are significantly lower than for the nitrogen-rich samples (0.021); that W depends on [Ns] is clear from the data in Fig. 3(b). In view of the above, the bulk value of W, W_B, is rather uncertain, in particular due to the fact that W arising from vacancy clusters is unknown. We are thus unable to provide an estimate of W_B.

In summary, the positron bulk lifetime in diamond is estimated at 98 ± 2 ps and the bulk S value at 0.380, i.e. 25% smaller than for Si. The bulk W value is more uncertain, but is probably close to 0.017, which is $\cong 2$ times higher than that for Si. Vacancy clusters are found in all of the investigated diamonds but are generally smaller in synthetic diamonds as indicated by the smaller values of τ_3. These vacancy clusters are situated in highly disordered regions into which positrons are trapped during slow-down, and these defects appear not to cause optical absorption.

b: Irradiated Diamonds.

The data for the irradiated diamonds IIa(1) are the easiest to interpret. Irradiation produces a new lifetime with a value of 145 ± 5 ps (Fig.5.3(c)), and its intensity and lifetime are independent of temperature between 30 and 300 K as is (essentially) the S/S_{Ref} parameter between 30 and 720 K (Fig.5.5); this shows that the vacancy is neutral. Combining positron and optical data for the GR1 absorption (see Table 8) we can state that the trapping rate per unit dose (column 4) is essentially constant and so is the

ratio between the GR1 absorption and the trapping rate (column 7). All this points to the conclusion that the irradiation-produced lifetime of 145 ± 5 ps arises from neutral monovacancies. Uedono et al. [63] found 140 ps at 300 K after electron irradiation using synthetic IIa diamonds, but observed a significant decrease to 120 ps at 10 K. This decrease, not observed in our natural IIa diamonds, may arise from flux impurities necessary to produce synthetic diamonds present, according to the manufacturer, (Sumitomo Corp., Japan), in the significant concentration range of 50 to 70 ppm.

Table 8. Dose dependencies for IIa(1) for the neutral vacancy lifetime, τ_{V^0}, trapping rate, κ, the defect specific Doppler parameter S_{V^0}/S_{Ref}, and the peak absorption coefficient of the GR1 zero phonon line at 741 nm (1.673 eV).

Dose ($10^{17} e^- / cm^2$)	τ_{V^0} (ps)	κ (ns^{-1})	$\kappa / dose$ ($\times 10^{-17} cm^2 ns^{-1}$)	S_{V^0} / S_{Ref}	GR1 (cm^{-1})	GR1/κ ($cm^{-1} \cdot ns$)
3	143 ± 8	0.7 ± 0.1	0.23 ± 0.03	1.05 ± 0.02	1.1	1.6 ± 0.2
8	150 ± 10	1.63 ± 0.15	0.20 ± 0.02	1.08 ± 0.02	2.9	1.8 ± 0.2
14	143 ± 3	2.6 ± 0.2	0.19 ± 0.02	1.08 ± 0.01	4.8	1.9 ± 0.2

The $40 \pm 6\%$ increase in lifetime for neutral monovacancies relative to the bulk lifetime is quite large and so is the corresponding $8 \pm 1\%$ increase in S, but their relative changes correlate well with those for Si where the lifetime increases by 23% and S by 3.5% for monovacancies [72]. The doubling in effect for diamond as compared to Si could be taken to mean that localization of the positron wavefunction increases with valence electron density which is 3.5 times higher in C than in Si.

In Ib diamonds negatively charged monovacancies are expected on the basis of optical measurements [37]. The positron results support this: the positron lifetime that

emerges upon irradiation is 142 ± 1 ps indicating a monovacancy, no GR1 absorption was observed, and the response from the monovacancies is much more pronounced in Ib than from the neutral vacancies. This latter point is most clearly displayed by the Doppler data in Table 4 where saturation with dose indicates a trapping rate of at least $\approx 200\ ns^{-1}$ (cf. Ch.3,section 3.6), much larger than for neutral vacancies. Since saturation trapping is occurring, the value of S/S_{Ref} becomes the defect-specific value S_{V^-}/S_{Ref}, equal to 1.079 ± 0.002, and indistinguishable from 1.08 ± 0.01 for S_{V^0}/S_{Ref} (Table 8). Thus we conclude that the positron experiments confirm the formation of V^- in Ib diamond and that the defect-specific S_V/S_{Ref} parameter as well as the positron lifetime are the same as for V^0 (within error bars). The results for Ib(syn) agree very well with those from [63], where the positron lifetime for negatively charged monovacancies was 140 ps and the increase in S upon $1 \times 10^{18} e^-/cm^2$ irradiation was found to be 7%; we find 8%.

For Ib(nat) and Ia(1) – Tables 5 and 6 – the τ_2 lifetime is the same ($\cong 134$ ps) after irradiation, which is marginally lower than for the samples just discussed. Whether this arises from the fact that these samples contain a considerable contribution from preexisting vacancies or from the fact that they contain $N_S \cdot N_S$ (A) centers is not clear. That $N_S \cdot N_S$ centers might play a role originates from the suggestion [37] that up to 40% of irradiation-produced monovacancies can be in "close" proximity to nitrogen impurities, (i.e. that monovacancies are inhomogeneously produced) which may alter the positron lifetime. In the following section (d) on annealing it will be argued that complexing between monovacancies with N_S reduces the positron lifetime by ~ 5 ps.

Based on the data for IIa(1) we can estimate the introduction rate of neutral monovacancies by assuming that the vacancy concentration per unit trapping rate in diamond is the same as that in GaAs; using data from [73] we find, in convenient units, $3.5\times10^{17} cm^{-3}ns$ while from [74] $1.5\times10^{17} cm^{-3}ns$. Using the average value and the average of trapping rate per unit dose (Table 8) the introduction rate is $0.5\pm0.2\ cm^{-1}$ for 2.3 MeV electrons. An earlier estimate based on Ia(1) [60] was 0.3 cm^{-1} for 3.5 MeV electrons, but should be adjusted in view of the smaller bulk lifetime found in this work; the new value is 0.5 cm^{-1}, and from the reirradiated sample (Table 6) we find $0.7\pm$ 0.2 cm^{-1} (at 3.5 MeV). These rates are larger than estimated from optical measurements (0.1 cm^{-1}, 2 MeV electrons) based on GR1 absorption [37] by at least a factor of 3. This discrepancy may be the compounded effect of comparing data arrived at by different assumptions, namely equal trapping efficiency in GaAs and diamond on the one hand and, on the other, the assumptions made to estimate the oscillator strength for the GR1 zero phonon line.

The introduction rate of V^- in Ib(syn) cannot be determined since the trapping rate is too large to be extracted from the lifetime spectra. The saturation of S/S_{Ref} somewhere between doses 3 and $8\times10^{17} e^-/cm^2$ (Table 4) indicates according to chapter 3, section 6 a trapping rate of $\approx 200\ ns^{-1}$ contrasting the trapping rate of only 2-3 ns^{-1} for V^0. This large difference in trapping rates cannot reasonably be explained by a 100-fold difference in introduction rate, although some increase is observed due to nitrogen [37], so instead we suggest that it overwhelmingly arises from the negative charge of vacancies. In Si it has been found both experimentally [75] and theoretically

[56] that by charging a vacancy, from neutral to singly negative, the trapping rate increases by a factor of 3 at room temperature. Here, for diamond, a much large increase is called for, but there are good reasons for expecting such. First, the dielectric constant for diamond is 5.7 whereas for Si it is 11.2 so the Coulomb potential is deeper in diamond. Secondly, the potential level at which the Coulomb tail is replaced by a flat potential towards the vacancy (see [56] for details) is –0.1 eV for Si whereas we find for diamond –0.3 eV according to [76]. Thus the Rydberg-like states (acting as precursor states for the final localization of the positron in the *negatively* charged vacancy) are deeper in diamond so less detrapping can occur from them; this in turn causes more efficient trapping by V^- than in Si. To illustrate the importance of detrapping we mention that detrapping at room temperature for a positron state situated 0.1 eV below the delocalized state is about 3000 times higher than for a state situated at 0.3 eV.

In summary, V^0 and V^- give rise to room temperature positron lifetimes of 145 ± 5 ps and 142 ± 1 ps, respectively, (a difference which is not statistically significant) and the close correspondence between the positron response and the GR1 optical response strongly supports the interpretation of GR1 absorption as arising from V^0. Although direct correlation of optical and positron response to V^- was not possible, the positron data are fully supportive of the interpretation that V^- occurs in Ib diamonds after electron irradiation. The introduction rate for V^0 is estimated to be 0.5 ± 0.2 cm^{-1} (for 2.3 MeV electrons) and is *perhaps* significantly higher (factor ~3) than that estimated by optical measurements. Generally, it is found that trapping by monovacancies in diamond causes changes in positron parameters that are significantly larger than in Si, so diamonds may also be the physicist's best friend.

c: Temperature Effects.

Four of the irradiated diamonds were investigated as a function of temperature between 30 and 770 K by means of Doppler broadening whereas lifetime measurements were restricted to the 30-300 K temperature range. A temperature dependence of the lifetime parameters for negatively charged vacancies in the Ib diamond might have been expected but saturation trapping precludes this observation. The most interesting aspect of the Doppler data (Fig.5.5) are the (reversible) increases in S/S_{Ref} for Ib(nat) and Ia(1) at elevated temperatures approaching the (saturated) value for V^- in Ib(syn). This suggests that vacancies in Ib(nat) and in Ia(1) become negatively charged, and indicates that the Fermi level is very close to the 0/- level for the vacancies and moves up with temperature. In contrast, the absence of change in IIa and Ib(syn) indicates that the Fermi level is far from this level so no influence from high temperature is observed. The effect is undoubtedly dependent on sample and dose, but does suggest that one cannot assume that the charge state of vacancies is independent of temperature which might have consequences for interpretations of annealing processes such as those by Davies et al.[37].

Another temperature dependence of S/S_{Ref} deserves comment, namely that observed for Ib(syn) below room temperature (less strongly in Ib(nat) and also found in [63], albeit to a lesser extent. Such an effect is commonly interpreted as arising from competitive trapping by "shallow" traps whose S and lifetime values are close to bulk values. Whether this is also the case for diamond we do not know, but have doubts for the following reason: If "shallow" traps were the reason then the value of τ_2 (see Table 7)

should also decrease because of the stronger admixture of a lifetime close to the bulk lifetime, but this is not observed; analysis of the Doppler data indicates that τ_2 should have decreased to 125 ps in order to be consistent with the model of "shallow" traps, but according to Table 7 the decrease was only to 140 ± 2 ps. In section 5.2 we will argue that the decrease in S/S_{Ref} can be attributed to annihilation of positrons in Rydberg-like states at negatively charged vacancies.

d: Annealing Studies

The results for the isochronal annealing of Ib(syn), shown in Figs.5.6-5.9, constitute the basis for several observations, the main one being an insight into the processes involved in the agglomeration of monovacancies with N_S. First we bring attention to the observation that S/S_{Ref} decreased irreversibly upon the at-temperature measurements discussed earlier. This decrease is shown in Fig.5.6 (compare 20 ^0C and 480 ^0C data) and suggests, as also found from optical measurements [37,70] on neutral vacancies, that irradiation-produced vacancies disappear *below* the onset temperature (~600 ^0C) of vacancy migration and is interpreted [70] to signify recombination resulting from thermally induced liberation of trapped carbon interstitials. The positron data suggest that this also occurs for negative vacancies based not only on the Doppler data but also on the lifetime data (Fig. 5.7(b)) where the observation that I_2 increases from 93 to 96% supports migration of interstitials because they can also become trapped by vacancy clusters so reducing their contribution to trapping, causing I_2 to increase.

An important aspect of the isochronal annealing data is the (remarkable) similarity between S/S_{Ref} and τ_2 as a function of temperature (Figs. 5.6 and 5.7(a), respectively). Since both parameters depend nearly exclusively on valence electron density we interpret the changes in these parameters to be caused by the migration of vacancies toward N_S forming $N_S \cdot V^-$ complexes. That $N_S \cdot V^-$ and not $N_S \cdot V^0$ is formed is deduced from the fact that S/S_{Ref} only changes slightly, and this agrees with the conclusion of Uedono et al. [63] as well as with optical absorption data [77].

N_S is "tetrahedrally" bonded to four C atoms, but the extra valence electron from N is localized at one of these C atoms causing a $\equiv 30\%$ elongation in bond length whereas the remaining three bonds are equally shortened [78]: An approaching vacancy has, therefore, two physically different sites to be trapped at, and the increase in the two positron parameters indicates that the monovacancy occupies initially the C atom position involved in the long bond of smaller electron density (τ_2 increases) and smaller spread in momentum distribution (S/S_{Ref} increases). That the vacancy "selects" this particular bond at $\sim 600\ ^0C$ may, simply, arise from it being easier to break the long bond than the shortened bonds. This configuration, however, seems not to be thermally stable at higher temperature since the positron parameters decrease gradually up to $\sim 720\,^0C$. We suggest that the underlying process is that the vacancy switches from its initial positron to a more stable one at one of the three shortened bonds characterized by slightly higher electron density and momentum spread. Between $\sim$ 780 and $820\,^0C$ no further changes in the structure of $N_S \cdot V^-$ complex occur, and according to Fig.5.9, the $N_S \cdot V^-$ absorption does not perceptibly change in this temperature range. However, it does change rather

abruptly above $820^{\circ}C$ (within $50^{\circ}C$) where τ_2 and S/S_{Ref} both increase and the optical absorption decreases by $\cong 15\%$. Thus a second rearrangement of the $N_S \cdot V^-$ complex is indicated after which the monovacancy appears to be in a less "crowded" environment. During this rearrangement some vacancies ($\cong 15\%$) escape from the traps and this is also reflected in the slight decrease in I_2 (Fig.5.7(b)): No further changes are observed up to $1170^{\circ}C$, indicating that the $N_S \cdot V^-$ complex has reached its final stable configuration at $\cong 870^{\circ}C$. Uedono et al. [63] also observed a decrease in τ_2 and S above $600^{\circ}C$, but did not find any evidence for the "annealing" step between 820 and $870^{\circ}C$.

Despite the fact that positron annihilation can only monitor averaged electron densities, via τ_2, and averaged momentum distributions, via S/S_{Ref}, the effects discussed above are large enough to permit the conclusion that the $N_S \cdot V^-$ complex undergoes several changes before reaching its final stable configuration; further elucidation would require hyperfine techniques and detailed optical measurements.

5.1.5. Conclusion

Positron annihilation data indicate that in as-grown diamonds (natural or synthetic) vacancy clusters are concentrated in highly defected regions. These defects seem not to be optically active and their concentration increases with the concentration of nitrogen in synthetic Ib diamonds. Data for Ia diamonds are particularly difficult to

analyze because of unresolved lifetimes associated with, possibly, $N_S \cdot N_S$ (A) and $N_S \cdot N_S \cdot V$ (B) centers.

Electron irradiation produces neutral monovacancies in type IIa diamonds and the positron response therefrom correlates well with the GR1 zero phonon line at 741 nm. In Ib diamonds negatively charged monovacancies are formed according to the positron data and this too is in keeping with optical data. The introduction rate of monovacancies (neutral) by 2.3 MeV electrons is estimated to be 3-7 times higher than the value based on optical measurements but this discrepancy may be due to calibration assumptions. The positron data confirm long-held interpretations of optical data regarding the monovacancy and its charge states.

At-temperature positron measurements extend significantly the traditional temperature regime for investigating monovacancies and suggest that they can change their charge state in Ia and Ib(nat) at elevated temperatures ($\geq$ 400 K) from neutral to negative, whereas in IIa they stay neutral.

$N_S \cdot V^-$ complexes formed in Ib diamonds upon annealing above 550^0C are suggested to undergo at least two "modifications" up to 870^0C before reaching a stable configuration which yields positron parameter values very close to that for the isolated negatively charged monovacancy.

5.2. On the trapping of positrons by negatively charged vacancies

5.2.1. Introduction

Trapping of positrons by neutral and negatively charged vacancies in semiconductors is a subject fundamental to positron annihilation investigations and was treated theoretically by Puska et al. [79]. They calculated specific trapping rates for a hypothetical semiconductor with a band gap of 0.7 eV using simplified models for the electronic structure and mechanisms by which positrons lose their energy in the trapping processes. They obtained the following results: For neutral vacancies the specific trapping is constant with temperature in most scenarios in agreement with experimental findings. For negatively charged vacancies the situation is more complex since positrons can be trapped by two mechanisms. One is trapping directly from the (delocalized) bulk state into the vacancy, the other, and in parallel with the first, consists of initial trapping in precursor states wherefrom trapping subsequently occurs at the vacancy. The precursor states are Rydberg-like (i.e. hydrogenic-like) since they arise due to a columb-like trapping potential. In this work we consider a simplified model that can be solved analytically and discuss also the important issue of energy dissipation during the trapping processes of positrons.

5.2.2. Model

Figure 5.10(a) depicts the features of the model proposed by Puska et al.[79]. There are several Rydberg-like states each with their own specific trapping rate μ'_{BR}, but because the energy of these states is expected to be close to the bulk state energy thermally activated detrapping, μ'_{RB}, must be taken into account. From each of these

states positrons are transferred, via the rate η'_{RD} to the vacancy proper. The annihilation rate in the bulk is λ_B, and is, reasonably, assumed also to be that for the Rydberg-like states.

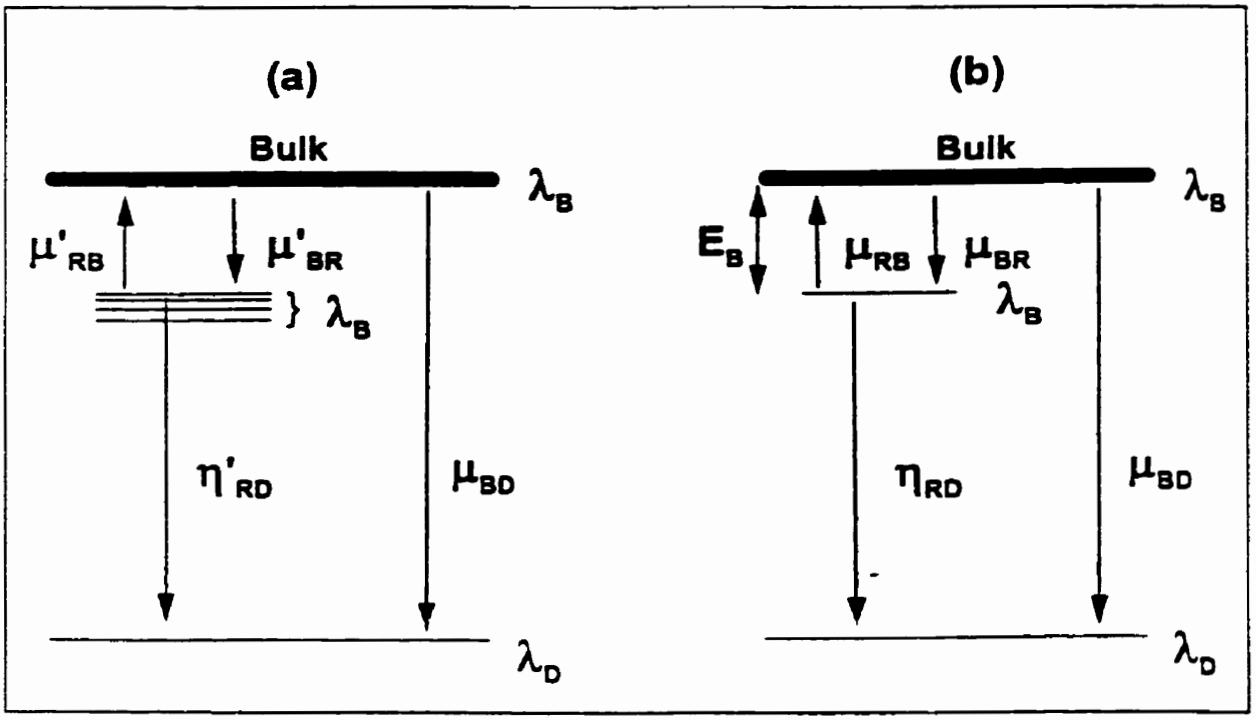

Figure 5.10. (a) Model for the trapping of positrons originally in the (delocalized) bulk state, into either several Rydberg-like states, thermal detrapping there from and transfer to the vacancy, or by direct trapping into the vacancy. (b) Simplified model replacing the manifold of Rydberg-like states with a single state resulting in the occupation probability equations (5.3 ~ 5.5), see text.

In the vacancy the annihilation rate is λ_D, and smaller than λ_B due to the smaller average electron density in the vacancy. Due to the multitude of Rydberg-like states this model is not amenable to detailed calculations nor to comparison with experimental data, so we replace it with the simpler model shown in Fig. 5.10(b), which preserves the essential features of the model in Fig. 5.10(a). For this model the occupation

probabilities, n_B, n_R and n_D of positrons in the three states (bulk, Rydberg and defect, respectively) are given by

$$\dot{n}_B = -\lambda_B n_B - \kappa_{BD} n_B - \kappa_{BR} n_B + \kappa_{RB} n_R . \tag{5.3}$$

$$\dot{n}_R = -\lambda_B n_R - \kappa_{RB} n_R - \eta_{RD} n_R + \kappa_{BR} n_B . \tag{5.4}$$

$$\dot{n}_D = -\lambda_D n_D + \eta_{RD} n_R + \kappa_{BD} n_B . \tag{5.5}$$

In these equations κ_{BD} equals $\mu_{BD} C_{V^-}$, where C_{V^-} is the relative concentration of negatively charged vacancies, i.e. equal to $[C_{V^-}]$/N with N being the atomic density; likewise, $\kappa_{BR} = \mu_{BR} C_{V^-}$ (the μ's and η_{RD} are the specific trapping rates as defined in Fig. 5.10(b)). The parameter κ_{RB} (detrapping rate from the Rydberg-like state to the bulk) is not an independent parameter because

$$\mu_{RB} = \mu_{BR} \exp(-E_B / k_B T), \tag{5.6}$$

where E_B is defined in Fig.5.10(b).

Assuming a parabolic density of states for the delocalized positrons gives together with Eq.(5.6)

$$\kappa_{RB} = \mu_{BR} \left(\frac{m_+ k_B T}{2\pi\hbar^2} \right)^{3/2} \frac{1}{N} \exp(-E_B / k_B T), \tag{5.7}$$

where m_+ is the effective mass of the positron, which we will assume equal to the free mass.

With the usual boundary conditions that n_B=1 and $n_R = n_D = 0$ at time t = 0 (i.e. all positrons occupy initially only the bulk state), we used a symbolic computer programme to solve Eqs. (5.3-5.5) for the time dependencies of n_B, n_R and n_D from

which experimentally observable lifetimes and their intensities can be calculated. Their expressions are complicated but are as follows:

Four convenient parameters can be defined:

$$r_1 = \kappa_{BR} + \kappa_{BD} + \lambda_B , \tag{5.8}$$

$$r_2 = \kappa_{RB} + \eta_{RD} + \lambda_B , \tag{5.9}$$

where r_1 and r_2 are physically identifiable as the disappearance rates from the bulk and Rydberg-like state, respectively, and

$$\alpha = (r_1 + r_2)/2 , \tag{5.10}$$

$$\beta = \sqrt{((r_1 - r_2)/2)^2 + \kappa_{RB}\kappa_{BR}} , \tag{5.11}$$

neither of which have any simple physical meaning, but are convenient mathematically.

The experimentally observable lifetimes are, following the tradition of enumerating lifetimes according to ascending values,

$$\tau_1 = 1/(\alpha + \beta) , \tag{5.12}$$

$$\tau_2 = 1/(\alpha - \beta) , \tag{5.13}$$

$$\tau_3 = 1/\lambda_D = 1/\lambda_3 , \tag{5.14}$$

and their associated intensities are, respectively

$$I_1 = \frac{1}{2} + (r_1 - r_2)/4\beta - \kappa_{BR}/2\beta + A , \tag{5.15}$$

$$I_2 = \frac{1}{2} - (r_1 - r_2)/4\beta + \kappa_{BR}/2\beta + B , \tag{5.16}$$

$$I_3 = 1 - I_1 - I_2 = -(A + B) , \tag{5.17}$$

where A and B are

$$A = 2[(r_1 - r_2 + 2\beta)(\lambda_D\kappa_{BD} - \kappa_{BD}r_2 - \eta_{RD}\kappa_{BR}) + 2\kappa_{BR}(r_1\eta_{RD} + \kappa_{BD}\kappa_{RB} - \lambda_D\eta_{RD})]/C ,$$

(5.18)

$$B = 2[(r_2 - r_1 + 2\beta)(\lambda_D \kappa_{BD} - \kappa_{BD} r_2 - \eta_{RD} \kappa_{BR}) - 2\kappa_{BR}(r_1 \eta_{RD} + \kappa_{BD} \kappa_{RB} - \lambda_D \eta_{RD})]/C ,$$

(5.19)

and C is

$$C = 8\beta(\alpha - \beta - \lambda_D)(\alpha + \beta - \lambda_D) . \quad (5.20)$$

Contributions to I_1 and I_2 arise from *all* of the three states whereas I_3 only arises from annihilations at the vacancies , so for the latter the physical origin of τ_3 is simple.

The fraction of positrons annihilating in the negatively charged vacancies is equal to $\int_0^\infty n_D \lambda_D dt$ which gives

$$F_D = A(\tau_1/\tau_3 - 1) + B(\tau_2/\tau_3 - 1) . \quad (5.21)$$

Although this expression for F_D is convenient when calculating lifetime parameters, it can also be obtained by integration of Eqs. (5.3-5.5) to yield the more manageable form

$$F_D = (\eta_{RD} \kappa_{BR}/(\lambda_B + \eta_{RD} + \kappa_{BD}) + \kappa_{BD})/(\lambda_B + \kappa_{BR} + \kappa_{BD} - \kappa_{RB} \kappa_{BR}/(\lambda_B + \eta_{RD} + \kappa_{RB})) .$$

(5.22)

This fraction is of merit since it enters into the Doppler broadening parameter via

$$S/S_B = (1 - F_D) + F_D S_D/S_B , \quad (5.23)$$

where S_B is the S parameter for the bulk (and Rydberg-like states), S_D is that for the negatively charged vacancy, and S would be the experimentally observed value.

5.2.3. Results and Discussion

What is of interest is how the observable positron parameters vary with temperature and one strongly influential parameter is κ_{RB} by virtue of its mainly exponential dependence on temperature (Eq. (5.7)), but so is the ratio κ_{BD}/η_{RD} and that may not be immediately obvious.

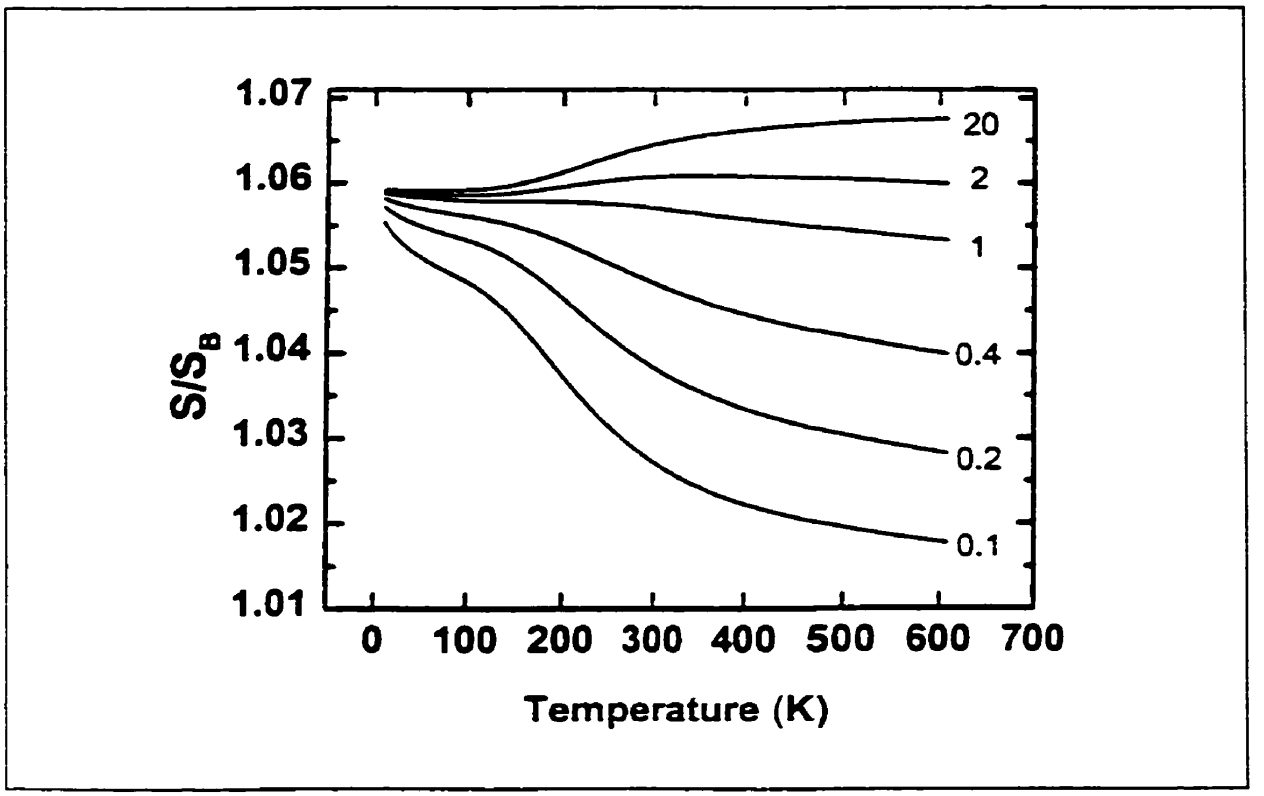

Figure 5.11. S/S_B as a function of temperature for different ratios of κ_{BD}/η_{RD} using the following parameter values at 300 K: Bulk lifetime 220 ps, defect lifetime 270 ps, defect specific S parameter S_D/S_B = 1.07, $\mu_{BR}=5\times10^6(\frac{300}{T})^{1/2} ns^{-1}$, $\mu_{BD}=1\times10^6(\frac{300}{T})^{1/2} ns^{-1}$, η_{RD} = 20 ns^{-1} (4 times the bulk annihilation rate), and E_B=50 meV. For the lowest ratio of κ_{BD}/η_{RD}, the relative concentration of the negatively charged vacancies is 2 ppm, and for increasing ratios, they are, 4, 8, 20, 40, 400 ppm.

To illustrate this, let us for the sake of argument assume that κ_{BD}/η_{RD} = 1, then according to Eq. (5.22) F_D equals $\kappa_{BD}/(\lambda_B+\kappa_{BD})$ so being independent of κ_{BR} and κ_{RB}. This realization can also be arrived at by inspection of Fig. 5.10(b): Since both the bulk and

the Rydberg-like state yield the same S value (because the annihilation rates are assumed the same (= λ_B)), it is immaterial to the value of F_D from which state the positrons are trapped into the vacancy: For $\kappa_{BD}/\eta_{RD} \neq 1$, F_D, and hence S/S_B, depends on κ_{BR} and κ_{RB}.

Figure 5.11 shows how S/S_B varies as a function of temperature for different ratios of κ_{BD}/η_{RD} evaluated at 300 K. Because κ_{BD} is assumed $T^{-1/2}$ dependent [79] whereas η_{RD} is assumed temperature independent, the curve for the ratio value of 1 (evaluated at 300 K) is not constant, albeit it shows the smallest variation with temperature as expected from the argument in the preceding paragraph. The temperature range inside which S/S_B is strongly sensitive to κ_{BR} and κ_{RB} depends on the value of E_B and shifts to higher temperatures with increasing values of E_B. Since η_{RD} is not dependent on the vacancy concentration whereas κ_{BD} is, an increase or a decrease in S/S_B with temperature depends on the vacancy concentration as illustrated by the values of κ_{BD}/η_{RD} for each of the curves shown in Fig. 5.11.

Observable lifetime parameters are shown in Figs. 5.12 and 5.13 for the same set of parameters as used in Fig. 5.11. Figure 5.12(a) depicts τ_1 and (b) τ_2 while in (c) is shown the composite (average) lifetime, τ_{avg}, as defined by $\sum_{i=1}^{3} I_i\tau_i$, (τ_3 = 270 ps). The temperature dependencies of these parameters are strongly dependent on the ratio κ_{BD}/η_{RD} and we note the close functional resemblance between τ_{avg} and S/S_B in Fig. 5.11.

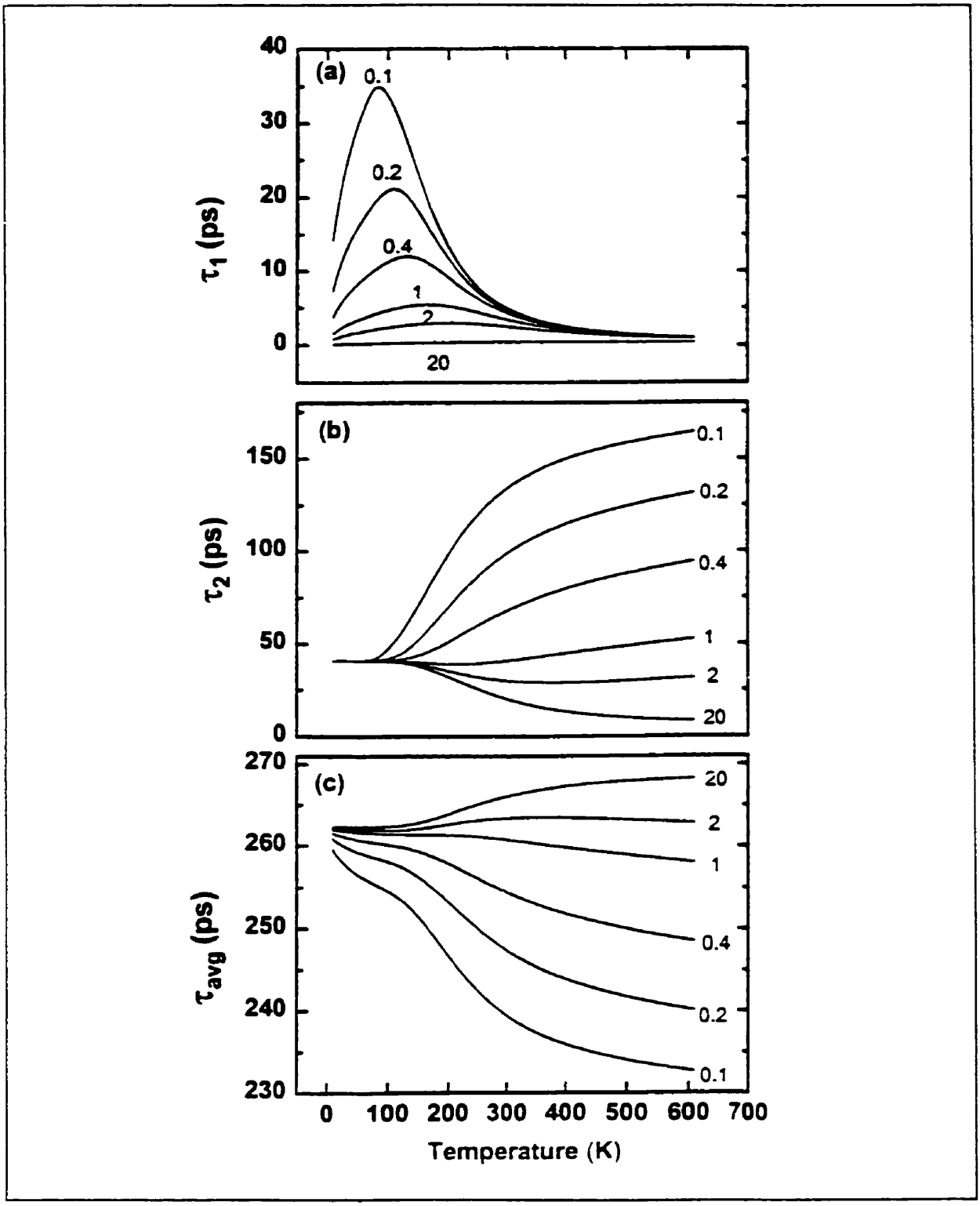

Figure 5.12. Individual lifetimes τ_1 (panel (a)) and τ_2 (panel (b)) for different ratios of κ_{BD}/η_{RD} (T = 300 K); τ_3 = 270 ps is not affected by these ratios. In panel (c) is shown the composite τ_{avg} parameter. Parameter values correspond to those used in Fig.5.11.

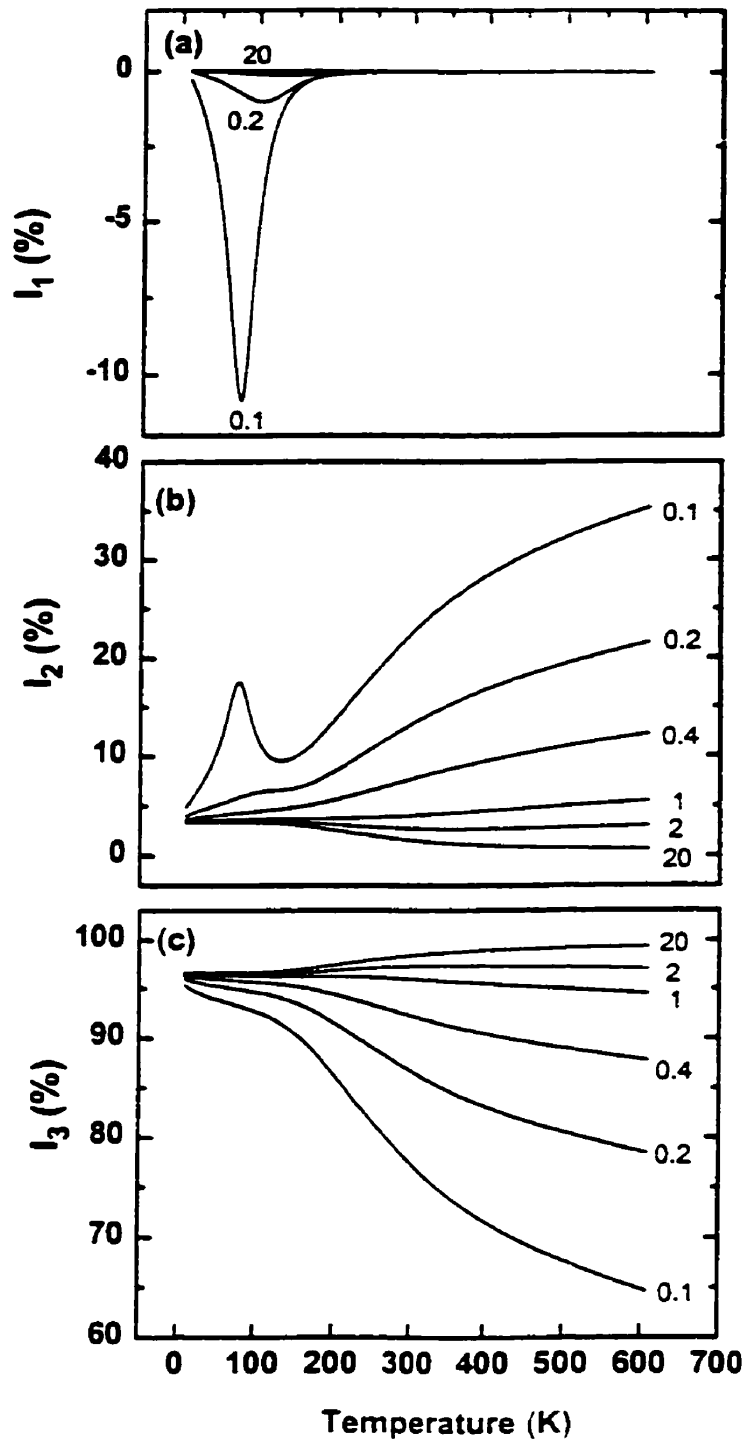

Figure 5.13. Intensities I_1, I_2 and I_3 of the τ_1, τ_2 and τ_3(=270 ps) lifetime components for different ratios of κ_{BD}/η_{RD} (T = 300 K).

The physical meaning of τ_1 and τ_2 is intricate as mentioned above: At temperatures where detrapping is large (> 200 K) τ_1 reflects mainly the disappearance of positrons from the Rydberg-like state and τ_2 mainly that from the bulk state while at low temperatures the reverse is the case. For the τ_3 component no such reversal with temperature occurs since positrons only disappear from the vacancies by means of annihilations.

Figure 5.13 shows the intensities of the three lifetime components. The occurrence of negative values for I_1 might be counter intuitive, but it should be pointed out that the intensities of the various lifetime components are not physical parameters unlike the occupation probabilities in Eqs. (5.3-5.5).

In experimentally obtained lifetime spectra lifetimes shorter than ≈ 50 ps cannot be resolved. Inspection of Fig. 5.12 shows that τ_1 would not be observable while τ_2 would for certain combinations of temperature and ratio values, so that either one-component spectra (with lifetime τ_3) or two-component spectra (τ_2 and τ_3) with positive intensities would be observable, features that make analyses of lifetime spectra a difficult task. An important consequence of the model is that the temperature dependencies of the observable positron parameters are markedly influenced by the value of κ_{BD}/η_{RD}, noting in particular that S/S_B can be reduced at low temperatures which questions the often invoked "shallow trap" concept.

The theoretical range of η'_{RD} (Fig. 5.10(a)) is quite large as calculated by Puska et al. [79]($\approx 3\ ns^{-1}$ to $\approx 1000\, ns^{-1}$) which unfortunately precludes any realistic assessment of the value for η_{RD} to be used in the model. We have therefor created an

experimental situation where κ_{BD}, and hence the ratio κ_{BD}/η_{RD}, varies significantly in order to test the model. The samples were two sets of diamonds both electron irradiated to a dose of $1.4\times10^{18} e^{-}/cm^{2}$. In one of the diamond sets (classified as IIa) the irradiation-produced monovacancies are neutral (see section 5.1), but a fraction of these can become negatively charged by means of illumination with 439 nm (2.83 eV) light (see the next section 5.3). For the other set (Ib diamonds) the monovacancies are negatively charged without illumination and at least 95% of the positrons are trapped at room temperature (see section 5.1).

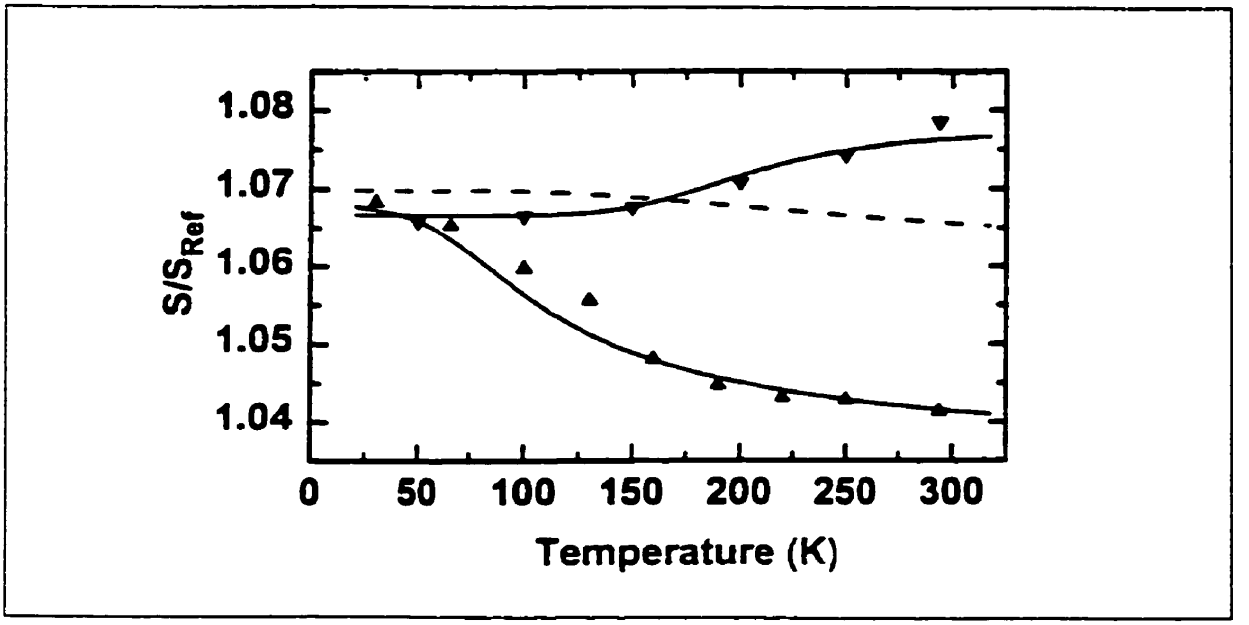

Figure 5.14. Experimental Doppler data as a function of sample temperature for two sets of diamonds, Ib (down-triangles) and illuminated IIa (up-triangles). The solid curves are fits to the data using parameter values as listed in Table 9 (first and third row) while the dashed curve is an attempt to fit the data for Ib using trapping parameters from IIa (second row in Table 9).

Let us first consider the data for the illuminated diamonds (up-triangles in Fig. 5.14), the mixture of neutral and negative vacancies requires a trivial extension of the model and with that gives the lower curve shown in Fig. 5.14 obtained using the parameter values

listed in Table 9. The good fit to the data demonstrates the feasibility of the model but there is considerable room for adjusting the first three parameter values. We note that η_{RD} is only 7 times the value for the bulk annihilation rate so the assumption by Puska et al. [79] that $\eta_{RD} >> \lambda_B$ might not be satisfied (λ_B for diamond is 10.2 ns^{-1} (see section 5.1)).

Table 9. Parameter values used to obtain the fits to the experimental data in Fig.5.14. The bulk annihilation rate is 10.2 ns^{-1}, the defect specific S/S_{Ref} is 1.079 for both neutral and negative monovacancies, and the vacancy concentration is 4 ppm ($7\times10^{17}/cm^3$) [see section 5.1]. μ_{BR} and μ_{BD} are specific trapping rates at 300 K. For neutral monovacancies the specific trapping rate is $1.5\times10^6 ns^{-1}$ and is used only in the case of IIa diamond.

Diamond Type	μ_{BR} ($10^6 ns^{-1}$)	μ_{BD} ($10^6 ns^{-1}$)	η_{RD} (ns^{-1})	E_B (meV	$[V^-]/[V]_{dark}$
IIa*	150	15	75	15	0.11
Ib**	150	15	75	15	1
Ib*	1500	150	70	80	1

*) Full curves in Fig.5.14.
**) Dashed curve in Fig.5.14.

For the other diamond set the experimental data are shown in Fig. 5.14 by the down-triangles, to which two fits were made. In the first the same parameter values were used as for the IIa diamonds except for setting the charge converted fraction to 1 since all the monovacancies are negatively charged: this resulted in the dashed curve and fits the data poorly, but a much better fit was possible with parameter values as listed in the 3rd row of Table 9. The μ values are now 10 times higher, E_B is 5 times higher but η_{RD} is essentially the same. We explain these changes by the $\cong 10$ times higher negative monovacancy concentration creating overlapping trapping potentials. This is mimicked in

the model by the increase in the μ values and E_B, while η_{RD}, as expected, is concentration independent.

Puska et al. [79] also addressed the most important issue of how a positron might rid itself of its binding energy when becoming trapped. In this context it is important to distinguish between the Rydberg state and the deep vacancy state. In the first, single phonon mediated trapping is most likely to occur, whereas deep state trapping into the vacancy requires a different mechanism due to the much larger amount of dissipated energy. The positron binding energy was calculated in the case of the monovacancy in Si to be between 0.4 and 1.0 eV depending on models [56,80] and an experimental value of 0.3 eV was found in GaAs [81]. These values are smaller than the band gaps which rules out electron excitation across the band gap as an energy dissipating mechanism. Puska et al. [79] also considered, in analogy with electron capture mechanisms, the possibility that defect states within the band gap could be a viable means of energy dissipation for positrons but here, too, energy consideration applies. It might be satisfied in the case of narrow band gap semiconductors ($\leq$ 1 eV), but for wider band gap materials such as diamond, SiO_2 and alkali-halides, the chance existence of suitable band gap states becomes increasingly improbable, yet trapping by vacancies does occur in all of the above mentioned materials [60,82,83]. There is, therefore, a need for a more general energy-dissipating mechanism for which we can mention two. The first is based on the spur model, i.e. that energetic positrons during slow-down produce free carriers and it is those that are available for energy dissipation during the trapping of a positron [84]. This model removes the above mentioned energy problem, but carries with it the other

problem of sufficient carrier concentration to make possible an effective (Auger) process, alleviation of which may, however, be accomplished by electron-positron attraction.

The second model, involving only phonons, is one in which multiple phonons are emitted during the trapping process. This model was originally advocated by Henry and Lang [85] to explain electron capture (see [86] for an eloquent review of energy loss mechanisms). This process is capable of dissipating several tenths of an eV and the rate of energy dissipation is comparable to positron annihilation rates. However, this model predicts a Boltzmann-like temperature dependency of the trapping cross section, and such has not generally been observed in positron experiments. This might be seen as a serious problem, but it should be noted that in the $\exp(-E_{barrier}/k_B T^*)$ term in the trapping cross section expression it is *not* the sample temperature, T, that centers but rather an "effective" temperature [85]. In the case of GaAs for the real temperature range of 20 K$\leq$ T $\leq$ 300 K the effective temperature range is from 210 K to 462 K (using a phonon energy of 35 meV), whereas for diamond T^* is essentially constant at 900 K for 20 K$\leq$ T $\leq$ 300 K (using 150 meV). Lack of an exponential T dependency can therefore not be construed to indicate the multiphonon process not being applicable. If the above discussed models indeed are operative in the case of positrons trapping, one may expect that specific trapping rates are material dependent.

5.2.4. Conclusion

We have examined the trapping of positrons by negatively charges vacancies based on a simplified model. Importantly, the scheme for trapping of positrons, as proposed by Puska et al. [79], has the inherent capability of predicting an increase as well

as a decrease in the temperature dependent fraction of positrons annihilating at vacancies depending on their concentration. The essential parameter determining this diverse behavior is the ratio κ_{BD}/η_{RD}, and questions the necessity for the shallow traps often invoked to explain a decrease in S/S_B at low temperatures. We have also discussed mechanisms for dissipation of the positron binding energy that may be of a more general nature than those considered so far, highlighting in particular the feasibility of the multi-phonon process.

5.3. Determination of the 0/- electronic level of the monovacancy in diamond by means of positron annihilation.

5.3.1. Introduction

Positron annihilation in conjunction with illumination provides a unique opportunity for investigating charge states of vacancies in semiconductors or insulators. Early investigations demonstrated this in the case of converting neutral chlorine vacancies to negatively charged in KCL [87,88] and results from more recent works [89~91] on GaAs and Si, using monochromatic light, are very promising for this particular avenue of positron annihilation experiments.

The strength of the method rests on the facts that positrons provide a vacancy-specific response and that the intensity of the response depends on the charge-state of the vacancies: If, for example, vacancies are neutral without illumination and turn positive upon illumination, their positron response will disappear because of the repulsion with the positively charged positron, whereas an illumination-induced negative charge of the vacancy will enhance the positron response. The capability of simultaneously identifying the vacancy-type defect that changes charge as well as the sign of the charge are features that neither photoconductivity, deep level transient spectroscopy, nor illumination-induced electron paramagnetic resonance posses. A restriction of the method is that high-resistivity samples are necessary to prevent free carriers from rapidly "nullifying" the photon introduced charging, a condition that was met in the works mentioned above [87~91]. Monochromatic light allows in principle for the determination of energy levels

for vacancy-like defects in the band gap without restrictions to their depth within the band gap or to sample temperature. In this work we have exploited these features to establish the 0/- electronic level of the monovacancy in diamond.

5.3.2. Experimental

Two IIa natural diamonds were irradiated at 8^0C by 2.5 MeV electrons to a dose of $1.4\times10^{18} e^- / cm^2$. Illumination was done with a 1/8 m Oriel monochrometer and a 100 W halogen lamp. In order to ensure a large photon flux (which in retrospect was not necessary) a fairly wide slit was used giving a band width of ~20 nm. The photon flux was monitored by a thermopile detector and photon fluxes entering into the samples are quoted with due consideration to the transmittance of the CdF_2 window in the cryostat and to the reflectivity of the diamonds, but are uncertain to within ~20% as far as absolute values are concerned.

Positron lifetime spectra were accumulated in time intervals of 3.3 h and repeated 6~8 times to allow for the detection of possible time effects arising from the accumulated photon dose over 24 h. At the level of photon flux $(9\pm2)\times10^{15} cm^{-2}s^{-1}$ no time effects were observed so the individual lifetime spectra were binned to produce two spectra, each with 8×10^6 counts, to improve on the analysis which was done using RESOLUTION [30]. The prompt full width at half maximum of the lifetime spectrometer was 200~205 ps, the positron source strength was 16 μCi (0.6 MBq) and the source contribution to the lifetime spectra was a component with 1.5% intensity and a lifetime of 250 ps, a correction that mattered little. The positrons probe a total volume of 0.2 mm^3 in the two

samples on each side of the positron source which is much less than the volumes probed by optical and EPR measurements.

Doppler broadened spectra were also accumulated in 3.3 h intervals giving 2×10^6 counts per spectrum in the annihilation peak, and again no time effects were observed. The energy resolution was 1.2 KeV and analyses were done in terms of the S parameter which provides a measure of the fraction of positrons trapped at vacancies (see section 5.1) optical absorption spectra were measured at 80 K in the wavelength range of 200 to 1200 nm.

5.3.3. Results and discussion

In Fig.5.15 Doppler results are shown as a function of photon energy using a constant photon flux of $(9\pm2)\times10^{15}cm^{-2}s^{-1}$ entering into the samples.

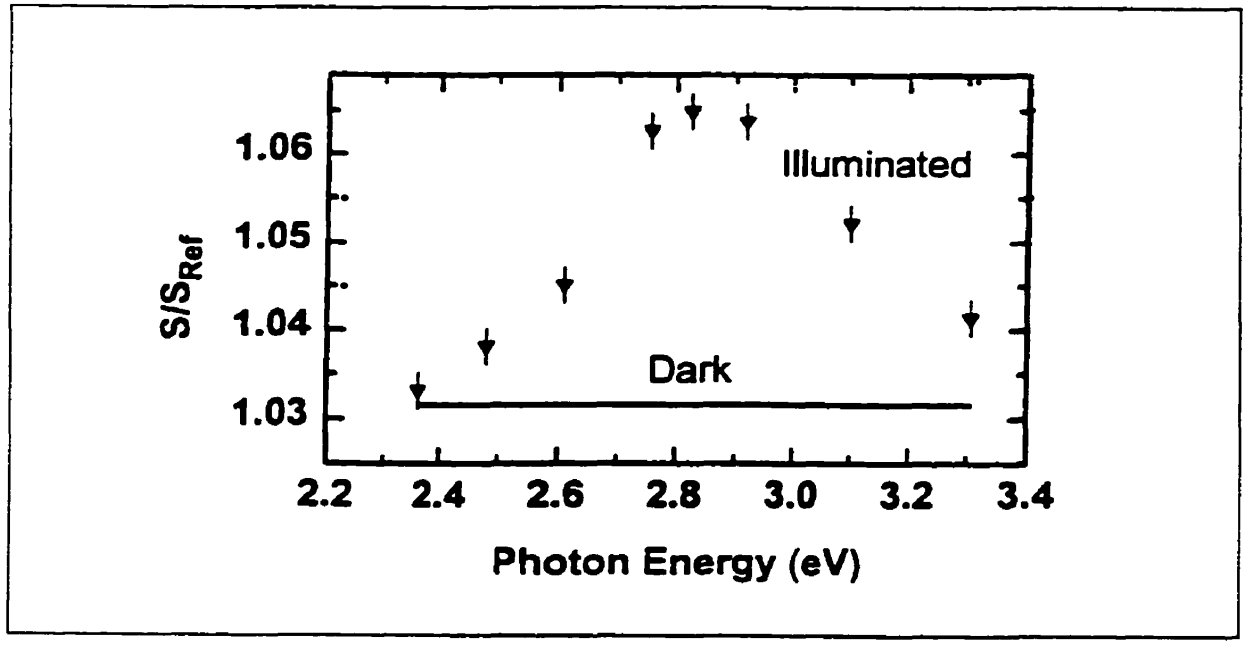

Figure 5.15. Doppler data obtained at 25 K with the samples in the dark and when illuminated with a photon flux of $9\times10^{15}cm^{-2}s^{-1}$ for photon energies between 2.35 and 3.3 eV.

The measured S parameter is normalized to $S_{Ref} = 0.380$, a value estimated to be close to the bulk value of S in defect-free diamond (see section 5.1). A significant increase in S/S_{Ref} is observed peaking at 2.8 eV whereas at 2.4 or 3.3 eV there is little effect compared to the dark value.

Lifetime data are in Table 10.

Table 10. Lifetime results for different illumination conditions. The photon flux was the same as for the Doppler data shown in Fig.5.15 ($9\times10^{15} cm^{-2}s^{-1}$) and the sample temperature was 30 K.

Condition	τ_1 (ps)	τ_2 (ps)	τ_3 (± 10 ps)	I_1 (%)	I_2 (%)	I_3 (%)
Dark	70±5	143±8	370	51±3	42±3	7±0.5
Photon energy						
$h\nu$=2.40 eV	50±5	128±5	348	25±3	67±3	8±0.4
$h\nu$=2.61 eV	Insolvable	128±7	376	0	89±1	11±1
$h\nu$=2.76 eV	Insolvable	142±4	365	0	90±1	10±1
$h\nu$=2.83 eV	Insolvable	137±4	348	0	89±1	11±1
$h\nu$=2.90 eV	Insolvable	145±5	348	0	91±1	9±1
$h\nu$=3.05 eV	Insolvable	142±3	342	0	92±1	8±1
$h\nu$=3.21 eV	50±5	133±4	318	19±4	73±3	8±0.8

In the dark condition three lifetimes could be resolved, τ_1, τ_2 and τ_3 with associated intensities I_1, I_2 and I_3, respectively. These lifetimes originate according to (section 5.1) from positrons residing in the bulk (τ_1), in the irradiation-produced neutral monovacancies (τ_2), and in highly disordered regions (τ_3). Upon illumination the τ_1 component could not be resolved, except for the two photon energies at 2.40 and 3.21 eV,

due to the increase in the fraction of positrons trapped by the monovacancies as reflected also by the increase in the S parameter (Fig.5.15), i.e. the response from vacancies has become saturated in the lifetime spectra. We ascribe this to the conversion of some of the neutral vacancies into negative vacancies whereupon there is little, if any, change in the value for τ_2.

Based on the data shown in Fig 5.15 the fraction, F, of positrons trapped by neutral and negatively charged vacancies can be calculated according to

$$F = \frac{(S/S_{Ref} - 1)}{(S_V/S_{Ref} - 1)}, \qquad (5.3.1)$$

where S_V is the vacancy-specific S parameter for the neutral and charged monovacancy, which according to (section 5.1) are the same ($S_V/S_{Ref} = 1.079$). The maximum value of 0.8 at the photon energy of 2.85 eV indicates a significant increase in trapping efficiency (the upper value for F is one).

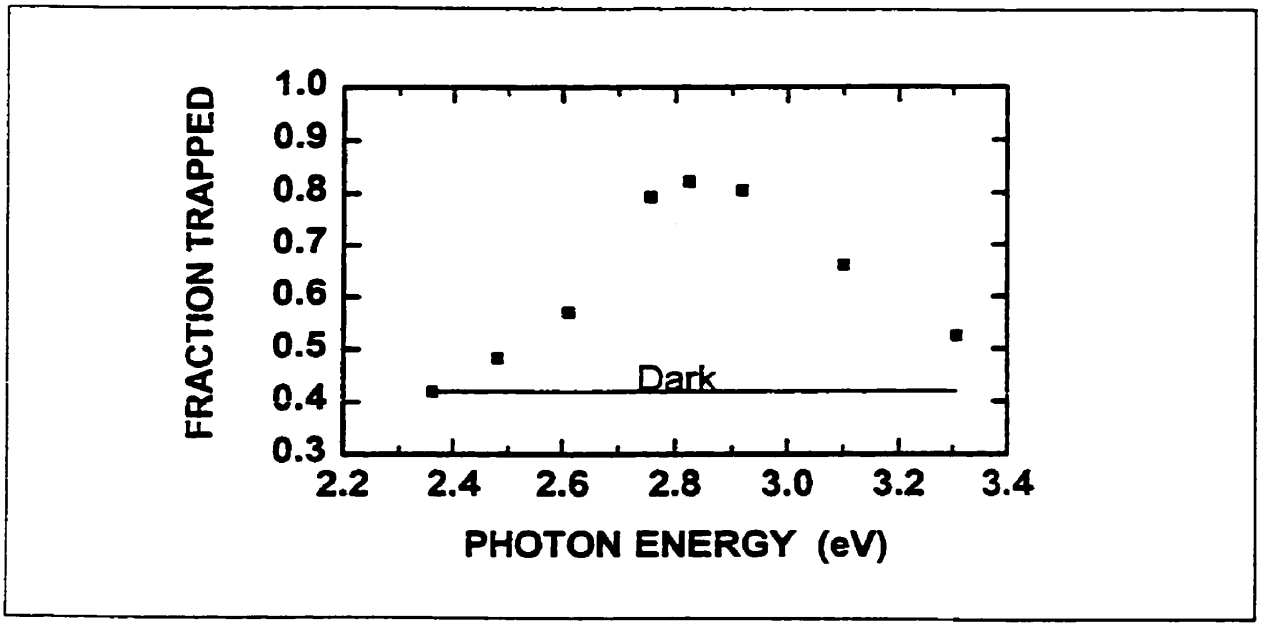

Figure 5.16. Fraction of positrons trapped as calculated from the data in Fig.5.15 using Eq.(5.3.1).

The temperature dependence of S/S_{Ref} is shown in Fig.5.17 in both the dark and illuminated conditions (photon flux and energy are $9\times10^{15}\,cm^{-2}s^{-1}$ and 2.83 eV, respectively). The significant increase in S/S_{Ref} at low temperatures is characteristic for trapping by negatively charged vacancies, whereas the nearly temperature independent results for the dark condition show that the monovacancies are neutral; this is in agreement with our optical data and those in [92].

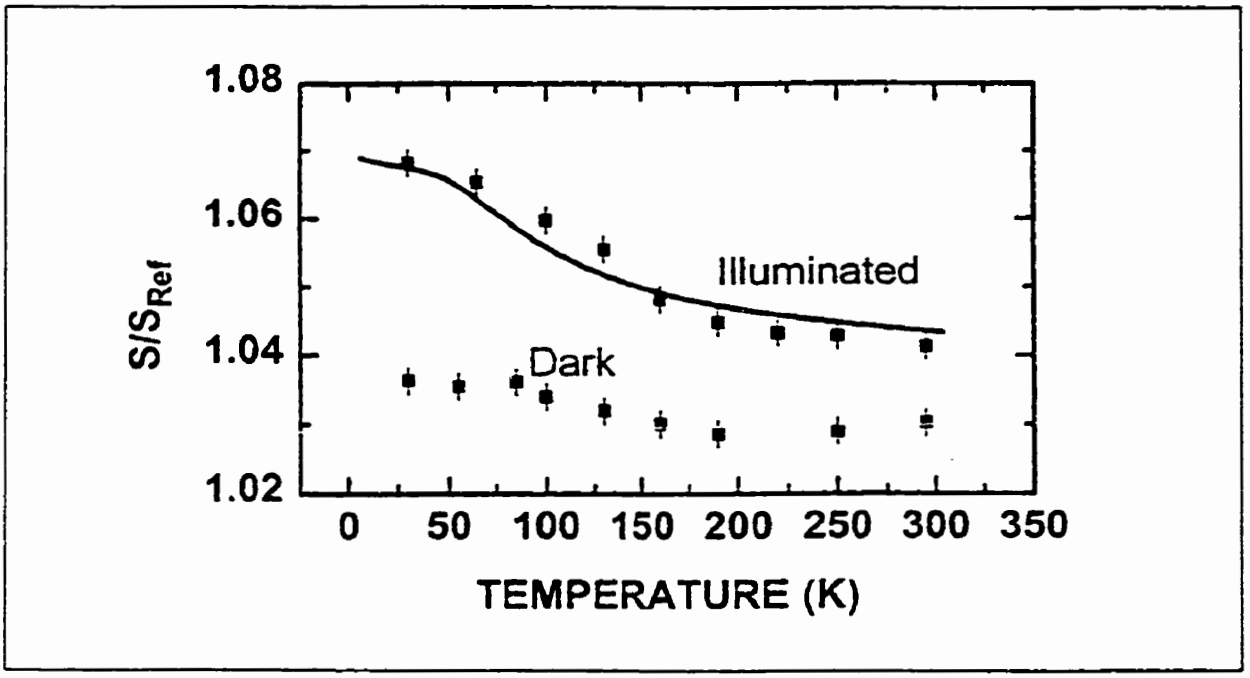

Figure 5.17. Doppler data as a function of temperature for samples in the dark and when illuminated with a photon energy of $2.83\pm0.07eV$ at a flux of $9\times10^{15}\,cm^{-2}s^{-1}$. The curve shows a fit using the model described in the text.

To gain further insight into the trapping by negatively charged monovacancies the data for the illuminated diamonds were fitted by a model proposed by Dannefaer and Pu (section 5.2) and based on the theoretical work by Puska et al. [79]. In this model positrons can be trapped directly by vacancies (V^0 or V^-), but in the case of V^- also via

a shallow Rydberg-like state from which final trapping by V^- takes place. This enhances significantly the overall trapping provided the thermally activated detrapping from the Rydberg states is quenched so, qualitatively, this explains the increase in S/S_{Ref} at low temperatures as shown in Fig.5.17. In applying the model, adjustments of 6-independent parameters are necessary, a task that does not bode well for the uniqueness of their values, but since some of these are only of importance at low temperatures while others are at high temperatures some decoupling of the parameters occurs. Of interest to this work is the fraction of V^0 turned V^- by the photons, for which we find a value of 0.1 ± 0.02. The model also provides for an estimate of the binding energy for the Rydberg-like states and values of 8-20 meV yield acceptable fits, values that are typical for shallow positron traps.

Using the parameters from the fit shown in Fig.5.17 but allowing the converted fraction to vary, the data in Fig.5.15 can be analyzed to yield the fraction as a function of photon energy. Fig.5.18 shows that V^- is formed within the photon range of 2.85 ± 0.15 eV full width at half maximum (this width includes the uncertainty in the photon energies of 0.07 eV). We interpret this result to mean that the 0/- electronic level of V^- is situated at 2.85 ± 0.1 eV above the valence band edge, i.e. very close to the middle of the band gap a position that has long been held probable in diamond research; here we have provided evidence therefor by means of positron annihilation. Because of the mid gap position of the 0/- level photons can both excite (valence) electrons to create V^- as well as remove an electron from V^- by exciting it into the conduction band, so the peaked structure results from the photon energy dependencies of these competing processes (we will return to the dynamics of V^- formation later).

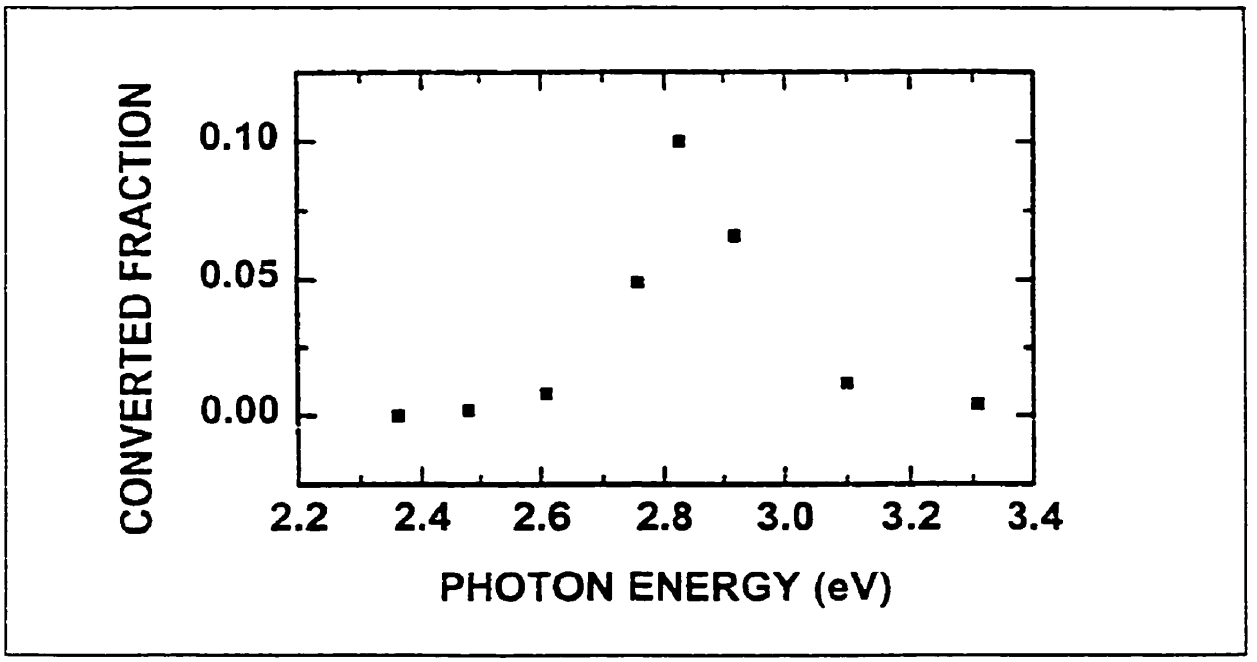

Figure 5.18. Fraction of neutral vacancies converted negative as a function of photon energy. The sample temperature was 25 K.

In agreement with the present photon-excitation results, Baldwin [93] found that photons with an energy above 2.8 eV gave rise to a new electron paramagnetic resonance, which according to the later work by Isoya et al. [94] arises from V^- (Baldwin misinterpreted his result to arise from V^+).

We also attempted to verify, but unsuccessfully, the charging of V^0 by optical absorption measurements at 80 K. V^0 gives rise to a dominant zero-photon line at 1.67 eV and V^- to one at 3.15 eV [92]. One of the samples was illuminated as in the positron measurements with 2.83 eV photons for one hour at 80 K in an optical cryostat after which the cryostat was placed in the spectrophotometer; this introduced a "dark" period of a few minutes and the optical absorption at the above mentioned line energies did not differ (to within 3%) from those obtained without 2.83 eV illumination. These optical

measurements are thus inconclusive as far as demonstrating conversion between the two charged states at 80 K. Light-on, light-off experiments were also done in connection with the data shown in Fig. 5.17 for sample temperatures of 25 K, 100 K and 300 K. Cycling at each of the temperatures showed that within ~½ h of the duration of each measurement (3.3 h) the S parameter reached the light-on and the light-off levels displayed in Fig. 5.17.

So the optical and the positron experiments show a rapid relaxation of V^- to V^0 and this is in sharp contrast to Baldwin's [93] observation that charging persisted for several days *in the dark*. The fast relaxation in the optical absorption experiments may well arise from the very act of doing so, and for the positron experiments, although performed in the dark, the ionizing effects from energetic positron and γ rays could increase the relaxation rate.

The above described positron experiments were done using a constant photon flux. It is of interest also to investigate the flux dependency of the converted fraction since that might give insight in the dynamics of V^- formation. A constant photon energy of 2.83 ± 0.07 eV was used in these experiments for two sample temperatures, 25 K and 293 K, and only Doppler measurements were made due to the problem of saturation of the lifetime spectra. Figure 5.19 shows the flux dependency of S/S_{Ref} and based on these data the converted fraction of neutral vacancies can be obtained in the same way as described above for their photon energy dependency, with results as shown in Fig. 5.20. To explain these data we apply a simple model in which it is assumed that V^0 is converted to V^- by a rate $r_1 = C_1 \cdot \Phi$, where C_1 is the optical cross section (at 2.83 ± 0.07 eV) and Φ is the photon flux. Since the 0/- level is essentially at mid-gap, a

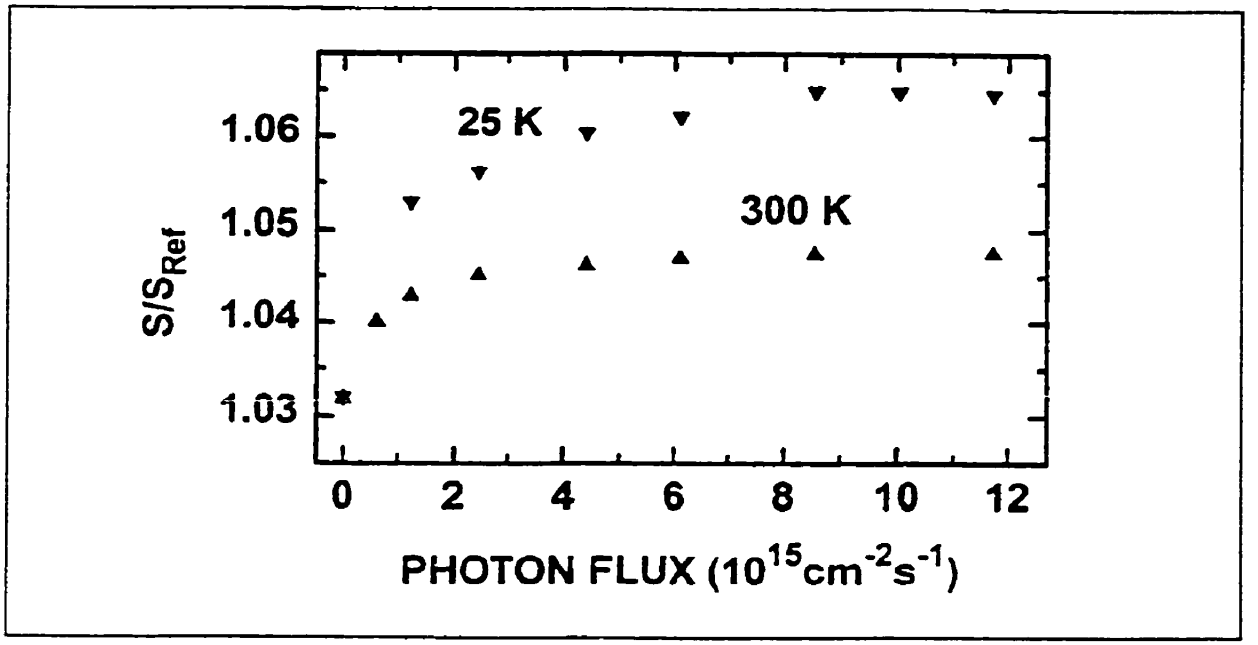

Figure 5.19. Doppler data as a function photon flux for two sample temperatures. The photon energy was 2.83 ± 0.07 eV.

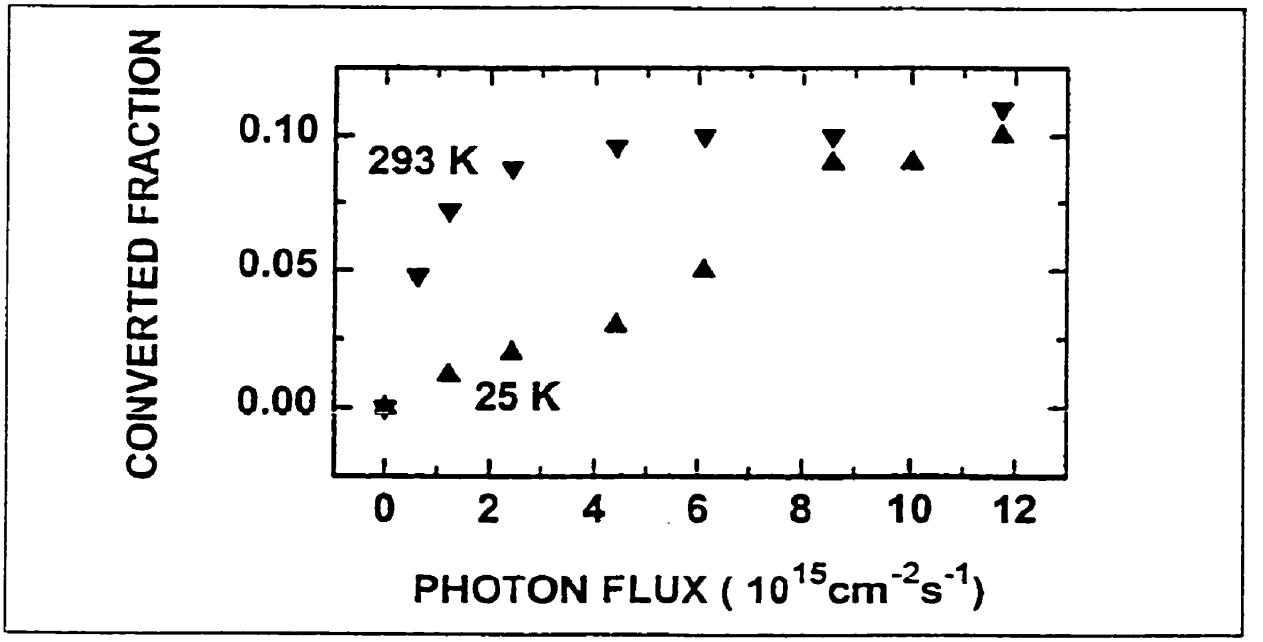

Figure 5.20. Fraction of neutral vacancies converted negative as calculated from the data in Fig.5.19 sample temperatures.

photon-induced back reaction via $r_2 = C_2 \cdot \Phi$ is also invoked, i.e. an electron can be removed from V^- by excitation to the conduction band by the same photon energy. Finally, a photon flux-independent rate γ is introduced to take into account the return of V^- to V^0 in the dark. This model gives the differential equation for the concentration of V^-.

$$\frac{d[V^-]}{dt} = r_1[V^0] - r_2[V^-] - \gamma \bullet [V^-] \qquad (5.3.2)$$

which together with conservation of vacancy concentration $[V^-] + [V^0] = [V^0]_{dark}$ and steady state (within the time frame of ½ h) gives

$$\frac{[V^-]}{[V^0]_{dark}} = \frac{C_1}{(C_1 + C_2 + \gamma/\Phi)}, \qquad (5.3.3)$$

where the converted fraction is that shown by the left hand side of Eq.(5.3.3). For the data obtained at 293 K (Fig.20), Eq. (5.3.3) describes well the flux dependency for values of $C_1/(C_1 + C_2) = 0.1$ and $\gamma/(C_1 + C_2) = 0.5 \times 10^{15}\ cm^{-2}s^{-1}$. The first number (0.1) indicates that the optical cross section, C_2, for removing an electron from V^- is nearly 10 times that for charging a neutral vacancy at the photon energy of 2.83 eV. As to the second number a realistic evaluation is not possible because the relaxation rate cannot be evaluation from the present data due to the 3.3 h duration of data accumulation.

At 25 K the converted fraction increases significantly slower with flux than at 293 K and a good fit to the data using the above model cannot be obtained. Nevertheless, we suggest that a reason for the *de facto* smaller converted fraction arises from an increase in the recombination rate of holes with V^- due to more efficient coulomb attraction at low temperatures.

5.3.4. Conclusion

Photons are capable of converting neutral monovacancies in IIa diamonds into negatively charged vacancies with maximum efficiency at 2.85 eV, indicating that its 0/- electronic level is situated at 2.85 ± 0.10 eV above the valance band. Photon flux dependencies on the charging of neutral monovacancies at 25 K and at 293 K suggests that the efficiency of creating V^- at 25 K is significantly less than at 293 K, an observation attributable to coulomb attraction between holes and V^-.

References:

[1] Gurney, J. J. (1989). In: proceedings of the fourth international kimberlite conference (J. Ross, ed.), Blackwell Scientific, Melbourne, vol.2,pp.935-965.

[2] Nixon, P. H.(1987). Mantle Xenoliths, Wiley, Chichester, pp.844

[3] Eric Bruton, F.G.A. (1971). Diamonds, Press Ltd., London, England, Ch.16.

[4] J.E. Field, Editor,(1992): The properties of Natural and Synthetic Diamond. (Academic Press).Part II.

[5] P.A.M. Dirac. Proc. Cambridge.Phil.Soc.26, pp.361(1929).

[6] P.A.M. Dirac., A Theory of Electrons and Protons. Proc.Roy.Soc.A126, pp.1360-36 (1930).

[7] Anderson, C.D., Science, New Series76, 238-239(1932).,C.D. Anderson, Phys.Rev.43, pp.491-494 (1933).

[8] Blackett, P.M.S., and G.P.S. Occhialini, Proc.Roy.Soc.A139, pp.699-726(1933).

[9] Tribaud, J., Phys.Rev.46, pp.781(1934).

[10] Klempere, O., Proc. Cambridge Phil.Soc.30, pp.347 (1934).

[11] Deutsch, M., Phys. Rev., 82, 1951a, pp.455.

[12] Deutsch, M., Phys. Rev., 83, 1951b, pp.866.

[13] V. Avalos, "Positron Annihilation Investigation of Electron Irradiated Silicon", MSc. thesis (1997) Positron Lab. of Physics, University of Winnipeg.

[14] K. Furderer, Hyperf. Interact.21 (1986), pp.81.

[15] I.K. Mackenzie, I.A. Eady and R.R. Gingerich, Phys. Lett. A **33**, pp.279(1970).

[16] P.H. Leo, K.D. Moore, P.L. Jones, and F.H. Cocks. Phys. Stat. Sol. B **108** pp.145 (1981).

[17] R.E. Bell and R.L. Graham, Phys. Rev. 90 (1953), pp.644.

[18] J.W. Shearer and M. Deutsch, Phys. Rev. 76 (1949), pp. 462.

[19] J. Mahony, "Point Defect Characterization of III-V Semiconductor Wafers Using Positron Annihilation Spectroscopy", M.Eng. thesis (1996), McMaster University.

[20] EG & G Ortec Inc. Photomultiplier, Instruction Manual.

[21] EG & G Ortec Inc.. Model 583 Constant-Fraction-Discriminator, Operating and service Manual.

[22] Dannefaer, S., " Positron Annihilation in Coloured and Uncoloured KCl and NaCl", Ph.D. Thesis (1972) Lab. of Applied Physics II, Technical University of Denmark, DK-2800 Lyngby, Denmark. P.10, 34.

[23] EG &G Ortec Inc. Model 566, Time-to-Amplitude-Converter. Operating and Service Manual.

[24] Goldanskii, V.I. and Prokopev, E.P., Soviet Phys.-Solid St., 6, pp.2641 (1966).

[25] P. Hautojarvi (Ed.), Positrons in Solids, Topics in Current Physics, vol.12, Springer-Verlag, Heidelberg, 1979.

[26] W. Brandt and A. Dupasquier, Positron-Solid State Physics, Proc. Int.School of Physics " Enrico Fermi ", Varenna 1981 (North-Holland Publ. Corp., Amsterdam 1983).

[27] W. Brandt: in Positron Annihilation, edited by A.T. Stewardt and L.O. Roellig (Academic Press, New York, N.Y., 1967) pp.155.

[28] B. Bergersen and M.J. Stott: Solid State Commun, 7, pp.1203 (1969).

[29] D.C. Connors and R.N. West: Phys. Lett. A, 30, pp.24 (1969).

[30] P. Kirkegaard, N.J. Pedersen, and M. Eldrup: Patfit-88, Risφ-M-2740, Risφ, DK-4000 Roskilde, Denmark.

[31] M. Lannoo and J. Bourgoin " Point Defects in Semiconductors I ", Solid State Science (Springer-Verlag, Berlin, Heidelberg, New York 1981).

[32] O. Reinkober, Ann. Phys. (Germany) vol.34 (1911)pp.342.

[33] Eric Bruton,F. G.A.(1971). In: Diamonds, Press Ltd., London, England,Ch.18.

[34] W. Kaiser, W.L. Bond, Phys. Rev. (USA). 115(1959) pp.857-63.

[35] J.F.H. Custers, Physica. vol.18 (1952) pp.489-96.

[36] Properties and Growth of Diamond. Ed. G. Davies, EMIS Data Reviews Series No.9 INSPEC, London, UK (1994) Chapter 5.

[37] G. Davies, S.C. Lawson, A.T. Collins, A. Mainwood and S.J. Sharp, Phys. Rev. B46 (1992) pp.13157.

[38] G. Davies, Nature 269 (1977) pp.498.

[39] R.G. Farrer, Solid St. Commun. 7 (1969) pp.685.

[40] P. Denham, E.C. Lightowlers and P.J. Dean, Phys. Rev. 161 (1967) pp.762.

[41] R.G. Farrer and L.A. Vermeulen, J. Phys. C: Solid St. Phys. 5 (1972) pp.2762.

[42] C.D. Clark, R.W. Ditchburn and H.B. Dyer, Proc. R. Soc. London Ser. A 237 (1956) pp.75.

[43] S.C. Sharma, C.A. Dark, R.C. Hyer, M. Green, T. Black, A.R. Chourasia, D.R. Chopra and K.K. Mishra, Appl. Phys. Lett 56 (1990) pp.1781.

[44] A. Uedono, S. Tanigawa, H. Funamoto, A. Nishikawa and K. Takahashi, Jpn. J. Appl. Phys. 29 (1990) pp.555.

[45] R. Suzuki, Y. Kobayashi, T. Mikado, H. Ohgaki, M. Chiwaki, T. Yamazaki, A. Uedono, S. Tanigawa and H. Funamoto, Jpn. J. Appl. Phys. 31 (1992) pp.2237.

[46] A. Saleh, P. Rice-Evans and S. Bull, Philos. Mag. B 70 (1994) pp.591.

[47] A. Saleh and P. Rice-Evans, Diamond and Relat. Mater. 3 (1994) pp.1293.

[48] P. Asoka-Kumar, B.F. Dorfman, M.G. Abraizov, D. Yan and F.H. Pollak, J. Vac. Sci. Technol. A 13 (1995) pp.1044.

[49] S. Dannefaer, W. Zhu, T. Bretagnon and D. Kerr, Phys. Rev. B 53 (1996) pp.1979.

[50] S. Dannefaer, J. Phys. C: Solid State Phys. 15 (1982) pp.599.

[51] S.Y. Li, S. Berko and A.P. Mills In: Zs. Kajcsos and Cs. Szeles, (eds.) Proc. 9th Int. Conf. On Positron Annihilation, (Trans. Tech. Publications, Aedermansdorf, 1992) pp.739.

[52] S. Fujii, Y. Nishibayashi, S. Shikata, A. Uedono and S. Tanigawa, Appl. Phys. A 61 (1995) pp.333.

[53] R.W.N. Nilen, S.H. Connell, W.G. Schmidt, D.T. Britton, W.S. Verwoerd, J.P.F. Sellschop and S. Shrivastava, Appl. Surface Science 116 (1997) pp.330.

[54] M. Shi, W.B. Waeber and W. Triftshauser, Appl. Surface Science, 116 (1997) pp.203.

[55] R.W.N. Nilen, S.H. Connell, D.T. Britton, C.G. Fischer, E.J. Sendezera, P. Schaaff, W.G. Schmidt, J.P.F. Sellschop and W.S. Verwoerd, J. Phys.: Condens. Matter 9 (1997) pp.6323.

[56] M.J. Puska, S. Makinen, M. Manninen and R.M. Nieminen, Phys. Rev. B 39 (1989) pp.7666.

[57] M.J. Puska and R.M. Nieminen, J. Phys.: Condens. Matter 4 (1992) L149.

[58] W.G. Schmidt and W.S. Verwoerd, Phys. Lett A 222 (1996) pp.275.

[59] B.K. Panda, S. Fung and C.D. Beling, Phys. Rev. B 53 (1996) pp.1251.

[60] S. Dannefaer, P. Mascher and D. Kerr, Diamond and Relat. Matter. 1 (1992) pp.407.

[61] A. Uedono, T. Kawano, S. Tanigawa, R. Suzuki, T. Ohdaira, T. Mikado, S. Fujii and S. Shikata, Jpn. J. Appl. Phys. 34 (1995) pp.1772.

[62] S. Dannefaer and D. Kerr, Diamond and Relat. Matter. 7 (1998) pp.339.

[63] A. Uedono, S. Fujii, N. Morishita, H. Itoh, S. Tanigawa and S. Shikata, J. Phys.: Condens. Matter. **11** (1999)pp.4109-4122.

[64] N.V. Novikov, T.D. Ositinskaya and V.S. Mikhalenkov, Diamond and Relat. Mater. 7 (1998) pp.756.

[65] I. Kiflawi, A.E. Mayer, P.M. Spear, J.A. van Wyk and G.S. Woods, Philos. Mag. B 69 (1994) pp.1141.

[66] S.R. Boyd, I. Kiflawi and G.S. Woods, Philos. Mag. B 72 (1995) pp.351.

[67] I.M. Reinitz, E. Fritsch and J. Shigley, Diamond and Relat. Mater. 7 (1998) pp.313.

[68] M.J. Puska and R.M. Nieminen, Rev. Modern Phys. 66 (1994) pp.841.

[69] J. Walker, Inst. Phys. Conf. Ser. No. 23 (1975) pp.317.

[70] L. Allers, A.T. Collins and J. Hiscock, Diamond and Relat. Mater. 7 (1998) pp.228.

[71] M. Alatalo, P. Asoka-Kumar, V.J. Ghosh, B. Nielsen, K.G. Lynn, A.C. Kruseman, A. van Veen, T. Korhonen and M.J. Puska, J. Phys. Chem. Solids 59 (1998) pp.55.

[72] V. Avalos and S. Dannefaer, Phys. Rev. B60(1999)pp.1729.

[73] S. Dannefaer and D. Kerr, Phys. Rev. B 48 (1993) pp.9142.

[74] J. Makinen, C. Corbel, P. Hautojarvi, P. Moser and F. Pierre, Phys. Rev. B 39 (1989) pp.10162.

[75] P. Mascher, S. Dannefaer and D. Kerr, Phys. Rev. B 40 (1989) pp.11764.

[76] C.O. Rodriguez, S. Brand and M. Taras, J. Phys. C: Solid St. Phys. 13 (1980) L333.

[77] Y. Mita, Phys. Rev. B 53 (1996) pp.11360.

[78] A. Mainwood, Phys. Rev. B 49 (1994) pp.7934.

[79] M.J. Puska, C. Corbel and R.M. Nieminen. Phys. Rev. B. 41 (1990) pp.9980.

[80] B. Barbiellini, M.J. Puska, T. Korhonen, A. Harju, T. Torsti and R.M. Nieminen. Phys. Rev. B (1996) pp.16201.

[81] S. Dannefaer and D. Kerr. Phys. Rev. B (1994) pp.14096.

[82] S. Dannefaer, T. Bretagnon and D. Craigen. J. Appl. Phys.86.pp.190(1999).

[83] S. Dannefaer, D.P. Kerr and B.G. Hogg. J. Phys. C: Solid St. Phys. (1975) pp.2667.

[84] O.E. Mogensen. Phys. Lett A. (1987) pp.409.

[85] C.H. Henry and D.V. Lang. Phys. Rev. B (1977) pp.989.

[86] J.S. Blakemore and S. Rahimi. In: Semiconductors and Semimetals, Vol. 20 (edited by R.K. Willardson and A.C. Beer) (Academic Press, Orlando, 1984) pp. 233.

[87] L.Bosi, A.Dupasquier, L.Zappa, J. Phys. Colloque, Paris C-9, suppl. 11-12, tome 34 (1973) pp.295.

[88] S. Dannefaer, G. Trumpy, R.M.J. Cotterill, J. Phys. C: Solid St. Phys. 7 (1974) pp.1261.

[89] K. Saarinen, S. Kuisma, P. Hautojarvi, C. Corbel, C. LeBerre, Phys. Rev. Lett. 70 (1993) pp.2794.

[90] H. Kauppinen, C. Corbel, J. Nissila, K. Saarinen, P. Hautojarvi, Phys. Rev. B57 (1998) pp.12911.

[91] S. Dannefaer, V. Avalos, Phys. Rev. B 60 (1999) pp.1729.

[92] G. Davies and N.B. Manson, in: "Properties and Growth of Diamond". Edited by G. Davies. INSPEC Data reviews series no. 9 (INSPEC, United Kingdom 1994) pp. 173.

[93] J.A. Baldwin, Jr. Phys. Rev. Lett. 10 (1963) pp.220.

[94] J. Isoya, H. Kanda, Y. Uchida, S.C. Lawson, S. Yamasaki, H. Itoh, Y. Morita, Phys. Rev. B45 (1992) pp.1436.